

We are IntechOpen, the world's leading publisher of Open Access books Built by scientists, for scientists

6,300

Open access books available

171,000

International authors and editors

190M

Downloads

Our authors are among the

154

Countries delivered to

TOP 1%

most cited scientists

12.2%

Contributors from top 500 universities



WEB OF SCIENCE™

Selection of our books indexed in the Book Citation Index
in Web of Science™ Core Collection (BKCI)

Interested in publishing with us?
Contact book.department@intechopen.com

Numbers displayed above are based on latest data collected.
For more information visit www.intechopen.com



Nonlinear Dynamics in Optoelectronics Structures with Quantum Well

Andreea Rodica Sterian

Additional information is available at the end of the chapter

<http://dx.doi.org/10.5772/intechopen.74557>

Abstract

The author presents some results on nonlinear dynamics in optoelectronics nanostructures as lasers with quantum wells and quantum well solar cells using mathematical modeling and numerical simulations of the phenomena which take place in such kinds of structures. The nonlinear dynamics takes the complexity of the phenomena into account, which govern the field-substance interaction. Computational software was elaborated to study the nonlinear phenomena in such quantum devices, which put into evidence their complex nonlinear dynamics, characterized by bifurcation points and chaos, and the critical values of the parameters being determined. The mathematical modeling and numerical simulations for the quantum well solar cells for optimizing the values of their optical parameters (refraction index, reflectance, and absorption) were also analyzed, so that the conversion efficiency of the devices can be improved. Although in our study we have considered only rectangular quantum wells, the hybrid model allows computing the optimum values of the parameters whatsoever the form of the quantum wells. The developed numerical models and the obtained results are consistent with the existing data in the literature for the optoelectronics of quantum well structures, having important implications in the applications.

Keywords: quantum well laser, quantum well solar cell, hybrid model, bifurcation diagram, chaotic state, quantum engineering, chaos masking

1. Introduction

The nonlinear dynamics is treated taking into account the complexity of the phenomena which govern the field-substance interaction including the dissipative phenomena [1–6]. Computational software was elaborated to study the nonlinear phenomena in such kinds of quantum devices [7–9].

A quantum well (QW) structure improves the functioning characteristics of laser diodes and of the solar cells as the emitted wavelength depends on nanostructure dimension (quantum size effect) [3, 10–13]. Such a structure is one in which the active region of the device is so narrow that quantum confinement occurs, according to quantum mechanics. The wavelength of the light emitted by a quantum well laser is determined by the width of the active region rather than just the band gap of the material from which the device is realized. Consequently, much shorter wavelengths can be obtained from quantum well lasers than from conventional laser diodes using a particular semiconductor material. The realization of quantum well structures represents cutting-edge technological advances in the field of semiconductor optoelectronics structures. These devices, unlike the classic ones, have the active area in the form of a periodic structure of semiconductor layers having different forbidden energy bands. These layers have very small thicknesses (nanometer units), their deposition being possible using advanced technologies and special deposition techniques.

In this chapter, first, we shall recall different forms of the rate equations used to take into account the complexity of the phenomena which govern the field-substance interaction. Based on computational software which was elaborated for the rate equation models presented, the phenomena were numerically studied in such a kind of quantum devices, and the utility of these models on some very simple examples and applications by different methods of simulations [14–21] was illustrated.

Second, we treat the complex nonlinear dynamics, characterized by bifurcation points and chaos, the critical values of the parameters being determined. The work emphasizes the variety of dynamical modes of operation of a semiconductor laser as a result of modulation of the injection current [22–28].

The third part of the chapter is dedicated to the particularities of the quantum well solar cells. The simulation results for the optical parameters (refraction index, reflectance, absorption coefficient) are presented as well as those for the optimization of the quantum efficiency of QW solar cells [21, 29–34].

Finally, as the application of the chaotic dynamics, an optical communications channel with chaotic laser signals is presented to demonstrate the important implications of these kinds of systems in quantum engineering and for transmission and processing of the optical information [35–40].

2. Modeling methods and techniques for quantum well lasers

2.1. Standard rate equations

Several levels of descriptions and modeling of field-substance interaction are known in the theory of lasers, depending on the classical or quantum character of the evolution equations, describing the two subsystems in interaction, the substance and the electromagnetic field, the laser system being a dissipative structure which takes on self-organizing phenomena, far from

equilibrium. Besides the phenomenological description of lasers owing to Einstein, who discovered the stimulated emission in 1916, which makes the amplification of coherent radiation in lasers possible, the theories developed for laser phenomena description are *the thermodynamic* theory, based on the equations of the rates as equations of balance for the populations of the laser levels and the density of the photons in the laser cavity, considering the dissipation; *the semi-classical* theory (or *semi-quantum*) in which the population equations are quantum, established as motion equations for the quantum operators corresponding to the populations of the levels involved and the field equation which is the classical equation describing the electromagnetic field in the laser medium, polarization of the medium being the source of the field; and *the quantum* theory in which both the substance and the electromagnetic field are described by quantum equations of evolution. The abovementioned theories are complementary to each other and are used according to the phenomena whose description is being followed in the studied issue or application.

As a system, the laser is described by the equations of two nonlinear coupled oscillators, a quantum oscillator represented by the polarization of the active medium and a classical oscillator which is the electromagnetic field from the optical resonant cavity. By pumping, the system receives external energy to realize the population inversion. Above the threshold, the oscillation condition being accomplished, the energy accumulated in the active medium is liberated through stimulated emission, under the form of the coherent light beam of laser.

The main quantum well laser model used in this chapter is based on the description of semiconductor lasers using the thermodynamic theory of the rate equations [14].

While the first models were based on one pair of equations to describe the density of photons and carriers in the active region, recent approaches include additional rate equations to take into account, and carriers transport between the active region and the adjacent layers of the structure as in Ref.s [15–18].

It can be observed that in most cases, the rate equations lead to multiple solutions, although only one solution is correct. Javro and Kang [19] showed that incorrect solutions or without physical sense can be eliminated or avoided through a change of variables in the rate equations. However, the transformations used are available under certain conditions, and for some cases, they give unrealistic solutions. These shortcomings are caused mainly due to the linear character of the gain-saturation coefficient. A more general expression of the gain-saturation coefficient, proposed by Channin, can be used to obtain models for operation regimes having a solution unique. Agrawal suggests another expression for this coefficient, which is also suitable. As is shown, any of these two forms of the gain-saturation coefficient can be used to obtain models with a solution unique to the operation regime.

2.1.1. *The model with linear gain saturation*

One of the prevailing laser diode models is based on a set of rate equations. The rigorous derivation of these equations originates from Maxwell equations with a quantum mechanical approach for the induced polarization. However, the rate equations could also be derived by considering physical phenomena described as in [3].

The population equation is as follows:

$$\frac{dN}{dt} = \frac{I}{qV_{act}} - g_0(N - N_0)(1 - \epsilon S)S - \frac{N}{\tau_p} + \frac{N_e}{\tau_n} \quad (1)$$

Similarly, the photon density equation is written as.

$$\frac{dS}{dt} = \Gamma g_0(N - N_0)(1 - \epsilon S)S + \frac{\Gamma \beta N}{\tau_n} - \frac{S}{\tau_p} \quad (2)$$

The photon density S reported the output power P_f as described by Eq. (3):

$$\frac{S}{P_f} = \frac{\Gamma \tau_p \lambda_0}{V_{act} \eta h c} = \vartheta \quad (3)$$

Eq. (1) relates the rate of change in carrier concentration N to the drive current I , the carrier combination rate and the stimulated-emission rate S . Eq. (2) relates the rate of change in photon density S to photon loss, the rate of coupled recombination into the lasing mode, and the stimulated-emission rate. The photon density S to the output power P_f is described by Eq. (3). The other parameters used have well-known significances as in Ref. [14]. This simple model can be directly implemented with Matlab Simulink.

2.1.2. The model with nonlinear gain saturation

An alternate version of the standard rate equations ensures us that for a nonnegative injection current, one nonnegative solution exists for density of both carriers and photons. The equations treated henceforth are the more generalized versions of Eqs. (1) and (2) with the linear gain-saturation term replaced by the term proposed by either Channin or Agrawal. The new equations are shown below as in Ref. [20]:

$$\frac{dN}{dt} = \frac{\eta_i I}{q N_w V_{act}} - R_w(N) - \Gamma_c v_{gr} \frac{\alpha(N)}{\Phi(S)} S \quad (4)$$

$$\frac{dS}{dt} = -\frac{S}{\tau_p} + N_w R_{w\beta}(N) + N_w \Gamma_c v_{gr} \frac{\alpha(N)}{\Phi(S)} S \quad (5)$$

$$\frac{S}{P_f} = \frac{\lambda \tau_p}{\eta_c V_{act} h c} = \vartheta \quad (6)$$

Eq. (4) relates the rate of change in carrier concentration N with the injection current, the carrier recombination rate and the stimulated-emission rate. In order to account for different recombination mechanisms, it considers $R_w(N) = AN + BN^2 + CN^3$, where A , B , and C are the unimolecular, radiative, and Auger recombination coefficient, respectively. Eq. (5) relates the rate of change in photon density to photon loss, the rate of coupled recombination into the lasing mode, and the stimulated-emission rate. In the above equations, the two gain-saturation terms are

$$\alpha(N) = G_0 \ln \left(\frac{R_w(N)}{R_w(N_0)} \right) \quad (7)$$

$$\alpha(N) = g_l G_0 \left(\frac{N}{N_0} - 1 \right) \quad (8)$$

where G_0 is the gain coefficient per quantum well, N_0 is the optical transparency density, and g_l is a factor obtained when linearizing the logarithmic gain around N_0 . Specifically,

$$g_l = \frac{AN_0 + 2BN_0^2 + 3CN_0^3}{AN_0 + BN_0^2 + CN_0^3} \quad (9)$$

The gain-saturation function can take on one of the following two forms:

$$\phi^{-1}(S) = \frac{1}{1 + \varepsilon \Gamma_c S} \quad (10)$$

$$\phi^{-1}(S) = \frac{1}{\sqrt{1 + \varepsilon \Gamma_c S}} \quad (11)$$

Using the approach taken in [11, 18, 20], an equivalent circuit model based on the above equations can be implemented in SPICE. Unlike models based on the rate equations that use a linear gain-saturation term, this circuit model is applicable for all nonnegative values of injection current.

2.2. Numerical experiments in MathCad

A comparative study of the models presented above for quantum well lasers is possible by numerical integration in MathCad of the corresponding equations to find the response for different types of pumping signals. The model with linear gain saturation, given by Eqs. (1) and (2), was integrated for a constant injection current, the corresponding waveforms for the optical output power being illustrated in [10]. The nonlinear gain-saturation model of Eqs. (4) and (6) was integrated for an injection current rectangular (**Figure 1**), which for some periods can be written under the form.

$$I_i(t) = 10^{-8} + 0,01 + 0,25 I_i(t - 2 \cdot 10^{-9}) + 0,25 I_i(t - 7 \cdot 10^{-9}) + 0,25 I_i(t - 12 \cdot 10^{-9}). \quad (12)$$

In general, all models studied give satisfactory results for the study of the transient and dynamic regime at low injection levels. At high injection rates, the numerical results obtained show the specific limits of each model, being consistent with the theoretical analysis.

2.3. Methods of modeling solutions of the rate equations

In this section, the two methods of modeling the solutions of the rate equations analyzed in [14] are presented. The first modeling technique is based on standard rate equations with a set

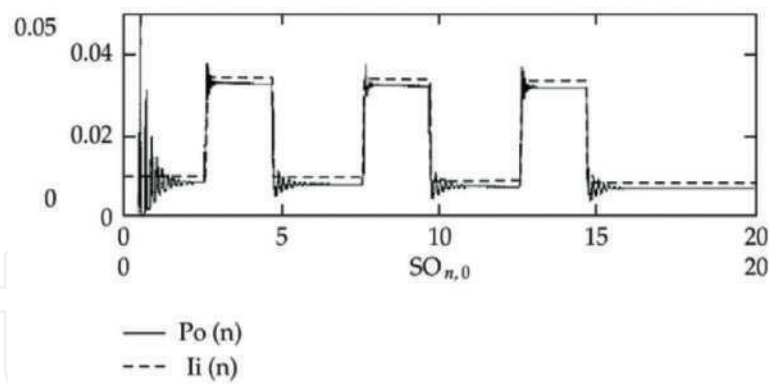


Figure 1. The waveforms of optical output power for an injection current rectangular in the model with nonlinear gain saturation.

of parameters given directly in Simulink. The second model is based on the standard rate equations that use a gain-saturation term and can be implemented in SPICE.

2.3.1. The Simulink modeling technique

This simple model can be directly implemented with Simulink like in **Figure 2**.

The input parameter from a signal generator is I , while S , N and P_f are the output parameters. All the parameters in the rate equations can be modified before the simulation starts as in all specialized papers [14–16].

With the above model, different signals can be used as input current for the quantum well laser. They show that the theoretical response of the equations is good when compared with real results that are expected in applications. Signals like saw tooth and sine types are used as input. The results are shown in **Figure 3**. They show very fast response at a low level of the current. Low threshold current is the main feature of quantum well lasers, and it is directly shown for the basic form of rate equation. The simulation is not perfect, and this is because of negative solutions for N and S and high power solution of the equations.

2.3.2. The SPICE modeling technique

In an alternate version of the rate equations, the linear gain-saturation term is replaced by the term proposed by either Channin or Agrawal [10, 15, 20]. Using the approach taken in [11, 14], an equivalent circuit model based on the above equations can be implemented in SPICE. Unlike models based on the rate equations that use a linear gain-saturation term, this circuit model is applicable for all nonnegative values of injection current.

In **Figure 4**, the circuit implementation is shown. This equivalent circuit can be obtained through suitable handling of the rate equations and by the transformations of variables. Diodes D1 and D2 and current sources I_{c1} and I_{c2} are modeling the linear recombination and charge storage in the device, while Br1 and Bs1 are modeling the effects of additional recombination mechanisms and stimulated emission, respectively, on the charges carrier density.

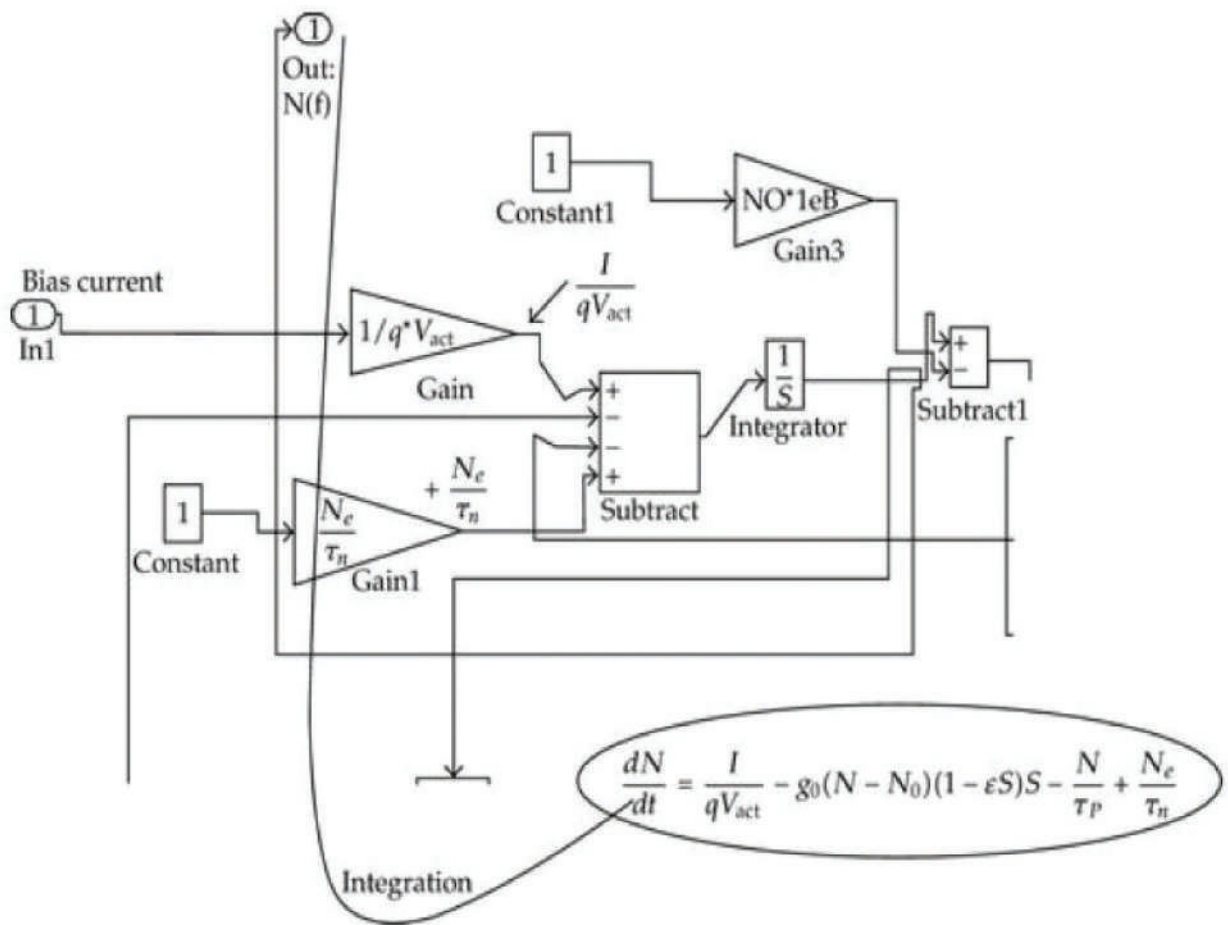


Figure 2. The Simulink block scheme of the rate equations.

The components Rph and Cph of the circuit help to model the time variation of the photon density under the effects of spontaneous and stimulated emission, which are accounted for by Br2 and Bs2, respectively. Finally, the source Bpf produces the optical output power of the laser in the form of a voltage. The circuit equations are given as follows:

$$I = I_{T1} + I_{D1} + I_{C1} + B_{r1} + B_{s1} \text{ where } I_{T1} = I_{D1} + I_{C1} \quad (13)$$

$$2\tau_p \frac{dm}{dt} + m = B_{r2} + B_{s2} \text{ and } B_{pf} = (m + \delta)^2 \quad (14)$$

$$I_{D1} = \frac{qN_w V_{act} N_e}{2\eta_i \tau_n} \left[\exp\left(\frac{qV}{nkT}\right) - 1 \right] \quad (15)$$

$$I_{D2} = \frac{qN_w V_{act} N_e}{2\eta_i \tau_n} \left[\exp\left(\frac{qV}{nkT}\right) - 1 + \frac{2q\tau_p}{nkT} \exp\left(\frac{qV}{nkT}\right) \frac{dV}{dt} \right] \quad (16)$$

$$I_{c1} = I_{c2} = \frac{qN_w V_{act} N_e}{2\eta_i \tau_n} \quad (17)$$

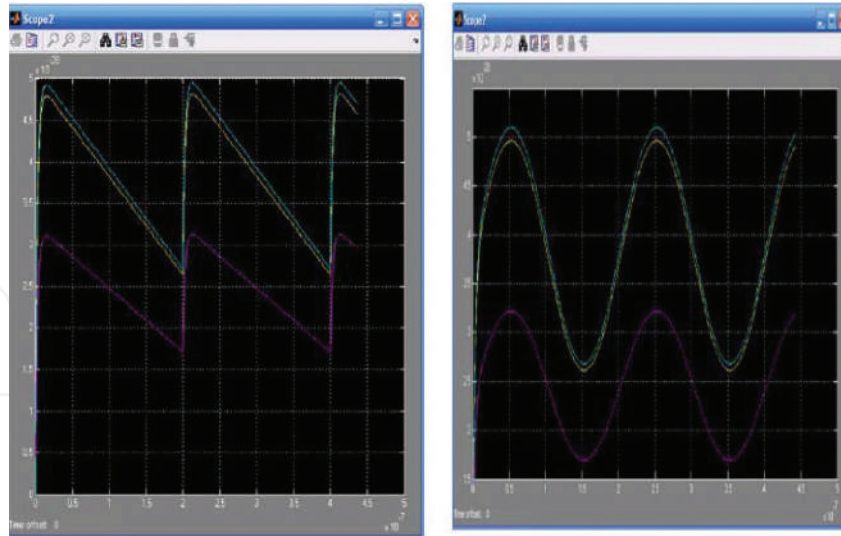


Figure 3. Output for saw tooth input signal of 10 mA amplitude and frequency of 5 MHz, and the output for the input signal sinusoidally having the same values for the amplitude and frequency.

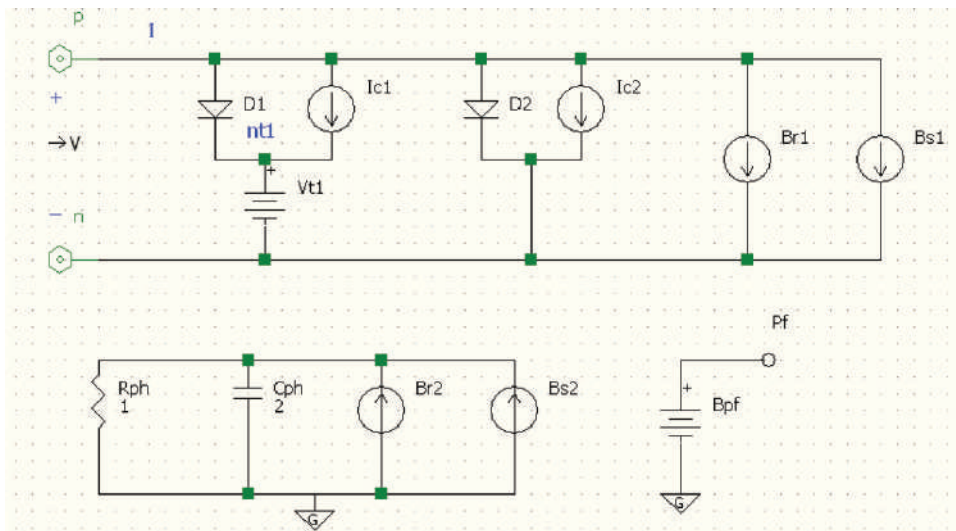


Figure 4. The electric circuit corresponding to the rate equation model.

$$B_{r1} = \frac{qN_w V_{act}}{\eta_i} R_{\omega 2}(\Theta I_{T1}) \tag{18}$$

$$B_{s1} = \frac{\lambda \tau_p N_w \Gamma_c v_{gr}}{\eta_i \eta_c h c} \frac{\alpha(\Theta I_{T1})}{\phi(\vartheta(m + \delta)^2)} \vartheta(m + \delta)^2 \tag{19}$$

$$B_{r2} = \frac{N_w \eta_c V_{act} h c}{\lambda \vartheta(m + \delta)} R_{\omega 2}(\Theta I_{T1}) \tag{20}$$

$$B_{s2} = \tau_p N_w \Gamma_c v_{gr} \frac{\alpha(\Theta I_{T1})}{\phi(\vartheta(m + \delta)^2)} (m + \delta) - \delta \tag{21}$$

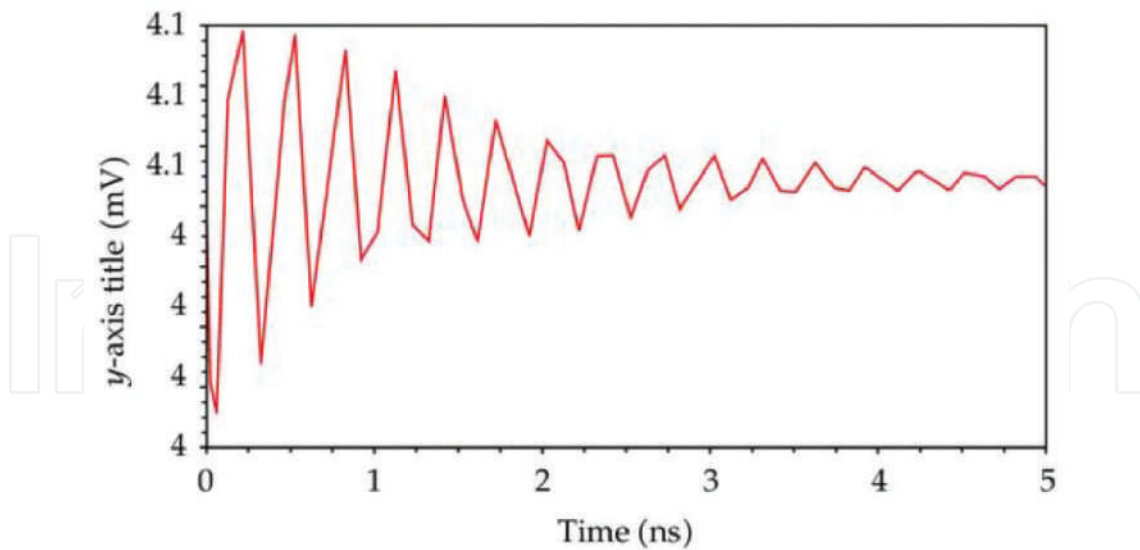


Figure 5. Transient output power response between 0 and 5 ns.

We implemented the SPICE netlist in AIM-SPICE, but calculating the parameters in the netlist is time-consuming. **Figure 5** shows results from PSPICE simulation with simple DC sweep and transient output power in response. (Obs: output power is given in Volt, because SPICE cannot have output variables in Watt).

Modifying one parameter will result in new calculations and new SPICE netlist. Simulations are not limited to SPICE, any all-purpose circuit simulators can be used to get similar results. Future development software that integrates circuit simulation and other modeling methods for quantum well lasers can be built to have a tool that models these devices from all points of view.

As a future development, we mention the method of the MATH package Simulink to simulate the behavior of the quantum well laser diodes with distributed feedback using the rate equations [16].

A more deeper additional can be the finite-difference time-domain (FDTD) method and then all are bundled in one software package for more simulation options [34].

3. Nonlinear dynamics of the quantum well laser

3.1. Modulation of the quantum well laser

We study the amplitude modulation of the injection current [22, 23]:

$$I = I_b[1 + m \sin(2\pi ft)] \quad (22)$$

where I_b is the polarization current and m modulation index:

$$m = \frac{I_m}{I_b} \quad (23)$$

where I_m is the amplitude of the modulating signal ($i_m = I_m \sin(\omega t)$), f being the modulation frequency.

3.2. The model of small signal and the frequency response

In this section, we analyze the low signal model and the frequency response of the laser for different polarization currents. The small signal model can be obtained from the equations of the rates, with two equations of populations [10], replacing $I, N_b, N_w,$ and S with $N_{b0} + \Delta N_b e^{j\omega t}, I_b + \Delta I e^{j\omega t}, N_{w0} + \Delta N_w e^{j\omega t},$ respectively, $S_0 + \Delta S e^{j\omega t}$, where I_b is the polarization current. The quantities N_{b0}, N_{w0}, S_0 are the solution of the considered rate equations, when the laser is pumped with the polarization current I_b , ΔI is the amplitude of a small perturbation overlaid on I_b and $\Delta N_b, \Delta N_w, \Delta S$ are the amplitudes of population densities and photon density corresponding to a small excitation. The frequency response of the laser is represented graphically in **Figure 6** using system (24) where N_{w0} and S_0 are calculated by means of the large signal model, placing $I(t) = I_b$ for the large t . The simulation parameters can be found in [10]

$$\begin{pmatrix} -\frac{i\Delta I}{qV_w} \\ 0 \\ 0 \end{pmatrix} = \begin{pmatrix} \bar{\omega} - \frac{i}{\tau_{cap}} - \frac{i}{\tau_n} - \frac{i}{\tau_{esc}} & 0 \\ \frac{i}{\tau_{cap}} & \omega - \frac{i}{\tau_{esc}} - \frac{i}{\tau_n} - ig_0 \frac{S_0}{1 + \epsilon S_0} & -i \frac{g_0}{(1 + \epsilon S_0)^2} (N_{w0} - N_0) \\ 0 & i\Gamma g_0 \frac{S_0}{1 + \epsilon S_0} + i\Gamma \frac{\beta_{sp}}{\tau_n} & \bar{\omega} + i\Gamma \frac{g_0}{(1 + \epsilon S_0)^2} (N_{w0} - N_0) - \frac{i}{\tau_p} \end{pmatrix} \cdot \begin{pmatrix} N_b \\ N_w \\ S \end{pmatrix} \quad (24)$$

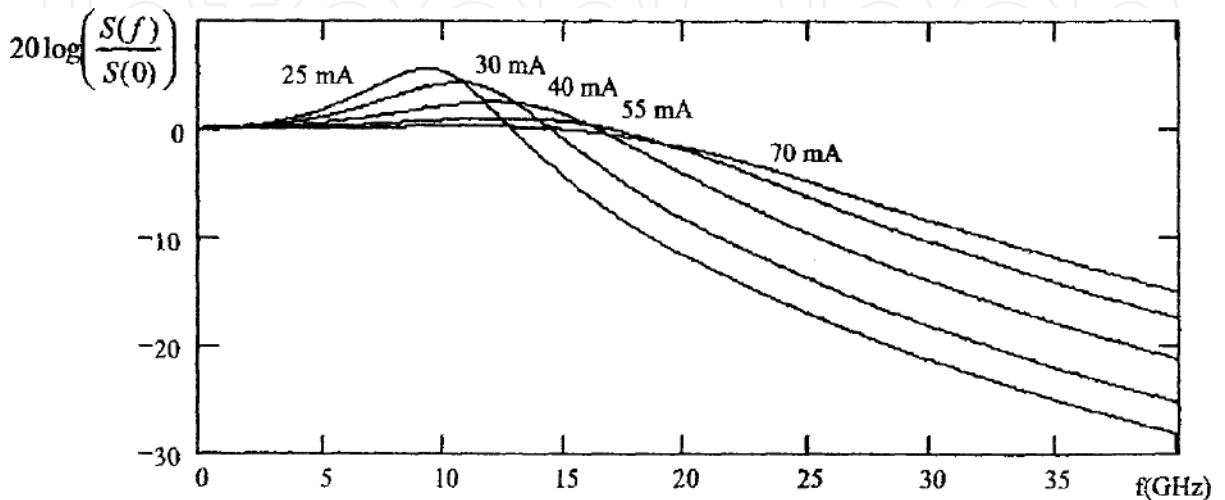


Figure 6. Frequency response of QW laser for $I_b = 25; 30; 40; 55; 70$ mA.

In the preceding paragraph, a small signal pattern was derived to analyze the frequency response of a QW laser for different polarization currents I_b . By increasing this current in a certain range, the laser band, the maximum modulation frequency increases.

As shown in the subsequent text, the QW laser band can be further extended if the gain of the active medium g_0 (e.g., carrier temperature in the active region of the laser) is modulated additionally to I . For this purpose, a new low signal model is derived. This time, we use the equations of the large signal pattern with one population equation [10, 20]. Optical gain is no longer a constant, having the form $g(t) = g_0(1 + \Delta P \sin \omega t)$, where ΔP represents a small fraction of g_0 . The system of linear equations of the small signal pattern written in a matrix form easily implementable in MathCad has the form:

$$\begin{pmatrix} \frac{-i\Delta I}{qV_{act}} + i(1 - \varepsilon S)Sg_0(N - N_0)\Delta P \\ -i(1 - \varepsilon S)Sg_0\Gamma(N - N_0)\Delta P \end{pmatrix} = \begin{pmatrix} \bar{\omega} - ig_0S(1 - \varepsilon S) - \frac{i}{\tau_n} & -i(1 - 2\varepsilon S)g_0(N - N_0) \\ i\Gamma g_0S(1 - \varepsilon S) + i\Gamma\beta\frac{1}{\tau_n} & \bar{\omega} + i(1 - 2\varepsilon S)g_0\Gamma(N - N_0) - \frac{i}{\tau_p} \end{pmatrix} \cdot \begin{pmatrix} N \\ S \end{pmatrix} \quad (25)$$

The results obtained by simulations for the photon density correspond to the three modulation cases and are given in [10]: (1) modulation of injection current and simultaneously of g ; (2) the simple modulation of I ; and (3) simple modulation of g , being presented in **Figure 7** (in all cases, $I_b = 50$ mA).

An increase in the bandwidth of the laser is observed when both I and g_0 are simultaneously modulated.

3.3. Routes to chaos and bifurcation diagrams

In **Figure 8**, the variation of the photon density S for different modulation indices as in [28] is compared.

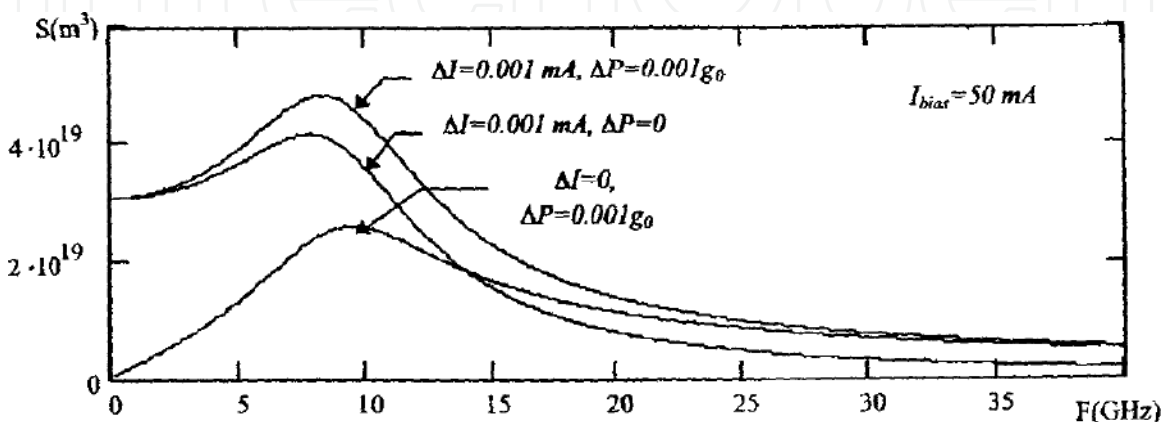


Figure 7. The photon density for three modulation cases: (1) modulation of injection current and simultaneously of g ; (2) the simple modulation of I ; and (3) simple modulation of g .

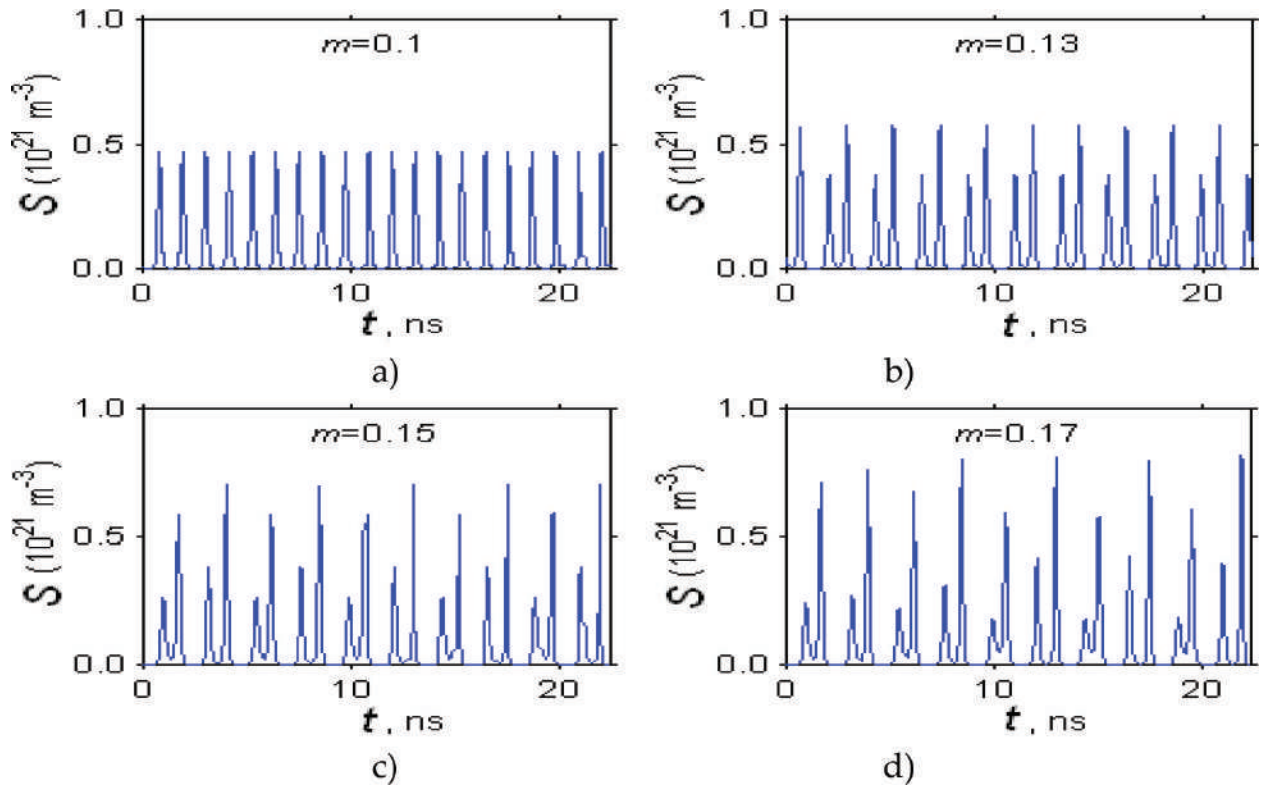


Figure 8. Time dependence of photon density for different modulation indices. The 1 T periodic signal in (a) becomes a double period (2 T) in (b), with the 4 T period in (c) and chaotically in (d).

Such a route to chaos with the increase of m by doubling of the period can also be presented qualitatively in the phase space as in [10, 28]. Knowing the hierarchy of instabilities of laser devices is useful in designing and calculating stable operating regimes in applications. Next, we analyze the bifurcation diagram of the peak photon density according to the modulation index (**Figure 9**) in the direct sense (with the increase of m) and vice versa (with the decrease of m) for a modulation cycle as an indicator of the evolution of the system.

In the chaotic region, there are periodic dynamic windows and a hysteresis dynamics (marked with arrows in **Figure 9**). In **Figure 10**, another bifurcation diagram is presented for a modulation frequency $f = f_0/2$, the other parameters remaining unchanged.

This result shows the complexity of system dynamics, without this complexity to be fully elucidated to date [12].

3.4. Rate equations with noise sources

The noise sources F_n and F_s are considered in the rate equations as in [27, 28]:

$$\frac{dN}{dt} = \frac{I}{qV_{act}} - g_0(N - N_0)S - \frac{N}{\tau_n} + F_n(t) \quad (26)$$

$$\frac{dS}{dt} = g_0(N - N_0)S - \frac{S}{\tau_p} + \gamma \frac{N}{\tau_n} + F_s(t) \quad (27)$$

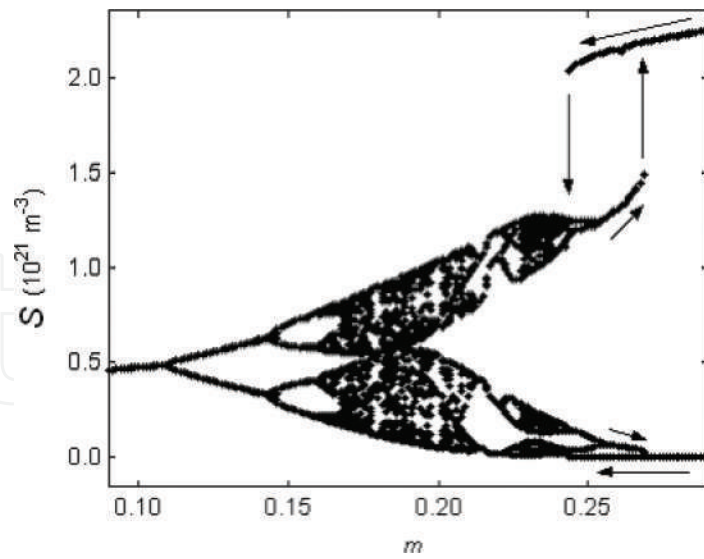


Figure 9. Bifurcation diagram of photon density depending on the modulation index.

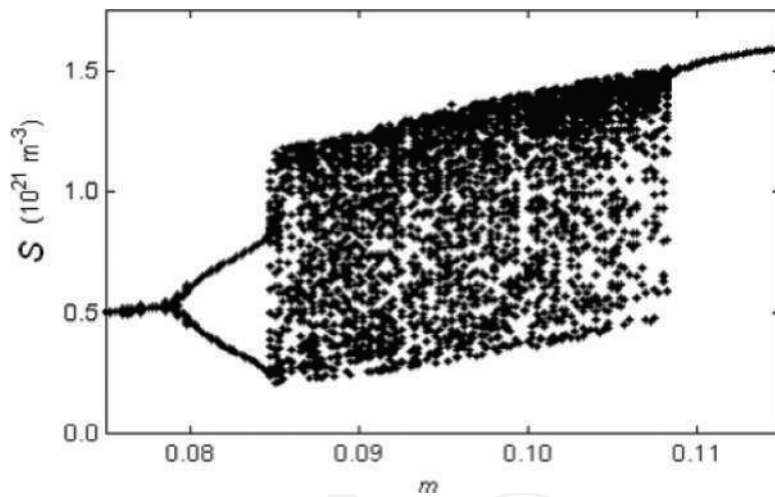


Figure 10. Bifurcation diagram for $f = f_0/2$.

In the Markoff approximation, noise sources are Gaussian variables of zero average, δ correlated, as

$$\langle F_n(t) \rangle = 0, \quad \langle F_n(t)F_n(t') \rangle = V_n^2 \delta(t - t') \quad (28)$$

$$\langle F_s(t) \rangle = 0, \quad \langle F_s(t)F_s(t') \rangle = V_s^2 \delta(t - t') \quad (29)$$

$$\langle F_n(t)F_s(t') \rangle = rV_nV_s \delta(t - t') \quad (30)$$

In the above expressions, V_n^2 and V_s^2 , there are variances of the random variables F_n and F_s , respectively, and r a correlation coefficient. See reference [28] for details. In the numerical modeling of Eqs. (26) and (27), it considers, for the intervals Δt , the autocorrelation function (7.81) of the form:

$$\langle F_n(t)F_n(t') \rangle = \begin{cases} V_n^2/\Delta t, & \text{pentru } |t - t'| < \Delta t \\ 0, & \text{pentru } |t - t'| > \Delta t. \end{cases} \quad (31)$$

This condition leads to the representation of

$$F_n = \left(V_n/\sqrt{\Delta t} \right) x_n \quad (32)$$

where x_n is a Gaussian random variable of zero average and unit variance.

By using Gaussian random numbers supplied by MATLAB functions, integration is achieved in much smaller steps Δt relative to the modulation period. Numerical calculations show that no matter how small the noise is, it disturbs the attractors and can even produce transitions between coexisting attractors.

For a modulation index $m = 0,265$, two stable attractors coexist (**Figure 11a** and **b**), but the presence of noise induces transitions from one attractor to another as is shown in **Figure 11c**. See references [27, 28].

The complexity of phenomena taking place in a laser diode in the presence of modulation is correlated with the nonlinearity of the stimulated-emission rate $g_0(N - N_0)S$, which will be analyzed extensively in the following paragraph.

3.5. Nonlinear dynamics of the MQW: A case study

This section presents a case study in which the nonlinear dynamics of the quantum hole laser is systematically analyzed on the basis of two population equations proposed by Nagarajan et al. [26]. In this model, a quantum well structure is modeled as a single quantum well structure, “concentrating” both the quantum wells and the barriers together.

Rate equations were solved numerically. The simulations were performed in the Matlab programming language using a fourth-order Runge–Kutta scheme [10].

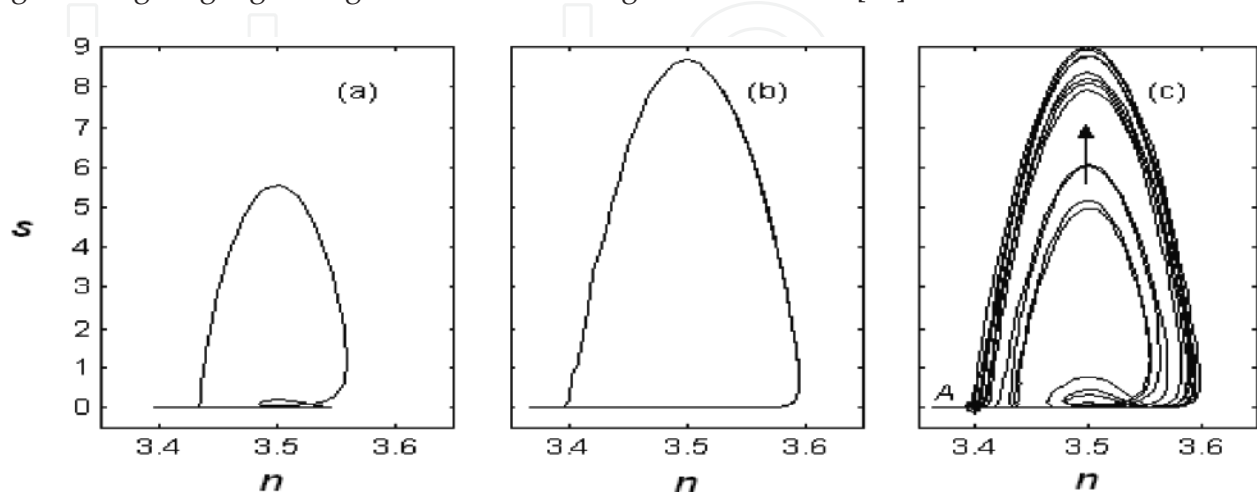


Figure 11. Influence of Gaussian noise on the evolution of the system in phases.

Detailed numerical investigations have shown that for lower frequencies with respect to the relaxation frequency, system dynamics is periodic with the radiofrequency modulator signal period.

For a small enough modulation index ($m = \frac{I_{RF}}{I_{DC}} \ll 1$), the periodic sinusoidal mode is obtained. The output power of the laser is sinusoidal, with the injection current (**Figure 12a**).

In the case of increasing of the modulation index and by approximating the frequency modulation with the frequency of the relaxation oscillations, a pulse operation mode (**Figure 12b**) is obtained, with a duration of the picoseconds (ultrashort pulses), the laser being used as a pulse source for optical communications.

For higher frequencies in relation to the resonance frequency of the system and modulation indices over a critical value, the phenomenon of doubling the frequency occurs.

The corresponding bifurcation diagrams are shown in [12]. At a value of parameter m for which the dynamics is $2T$ (nT), the representation consists of two points (n points). Higher modulation frequencies cause multiple bifurcation points, including chaotic dynamics for certain parameter values ($f = 8$ GHz, in **Figure 13**).

Also in **Figure 13**, the dependence of the critical modulation index (frequency bifurcation) is observed (for $f = 12$ GHz, m_{critic} is higher than for $f = 7$ GHz). **Figure 14** shows the laser nonlinear dynamics $4T$ (**Figure 14a**) and the corresponding two-dimensional representation in the phase space (**Figure 14b**), for $I_{DC} = 20$ mA, $f = 8$ GHz, and $m = 3.5$. For an increased modulation index, $m = 5.5$, the dynamics becomes chaotic (**Figure 14c and d**).

The behavior is similar for other over-threshold injection current values, but there is an increasing dependence of the modulation index on doubling the period with the polarization current.

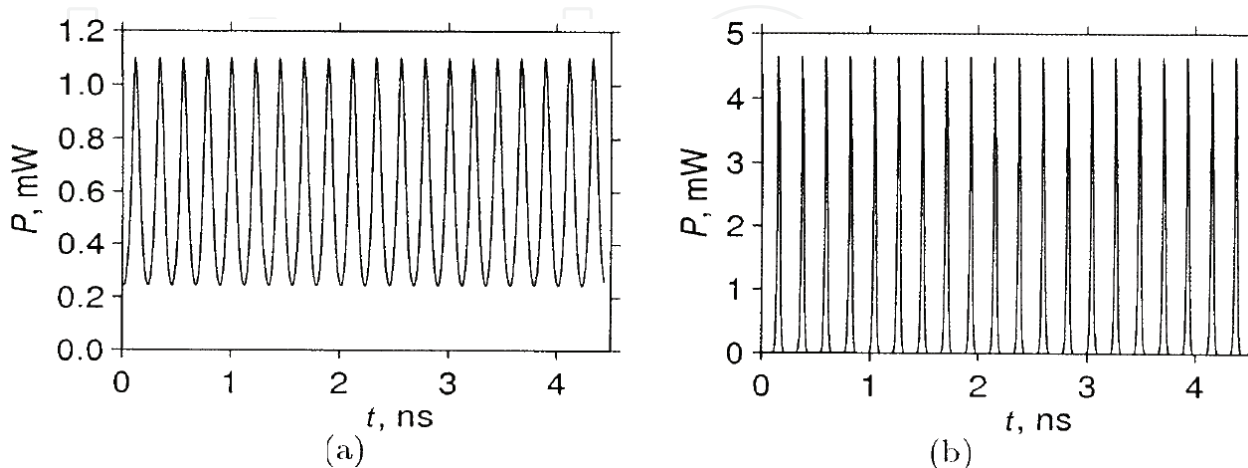


Figure 12. (a) Output power of the laser, sinusoidal for low signal modulation ($m = 0,1$); (b) the same pulse dependence, for $m = 2$ ($I = 20$ mA, $f = 4.5$ GHz).

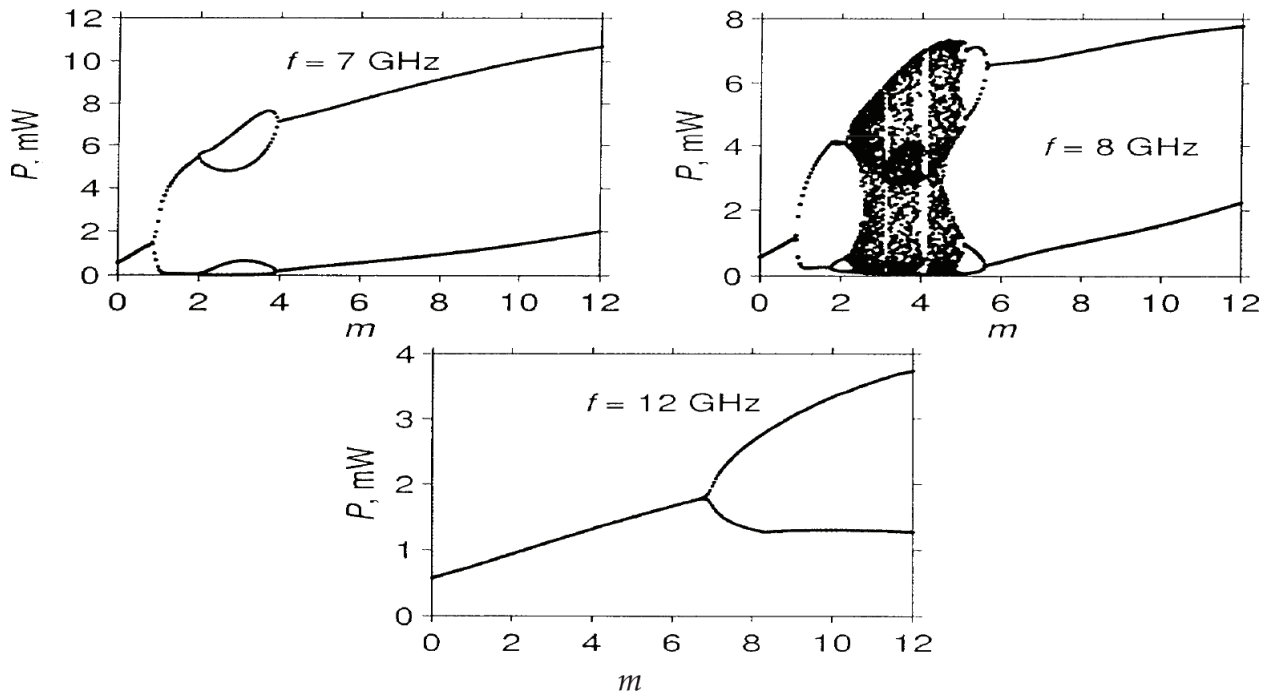


Figure 13. Bifurcation diagrams of the laser for different modulation frequencies.

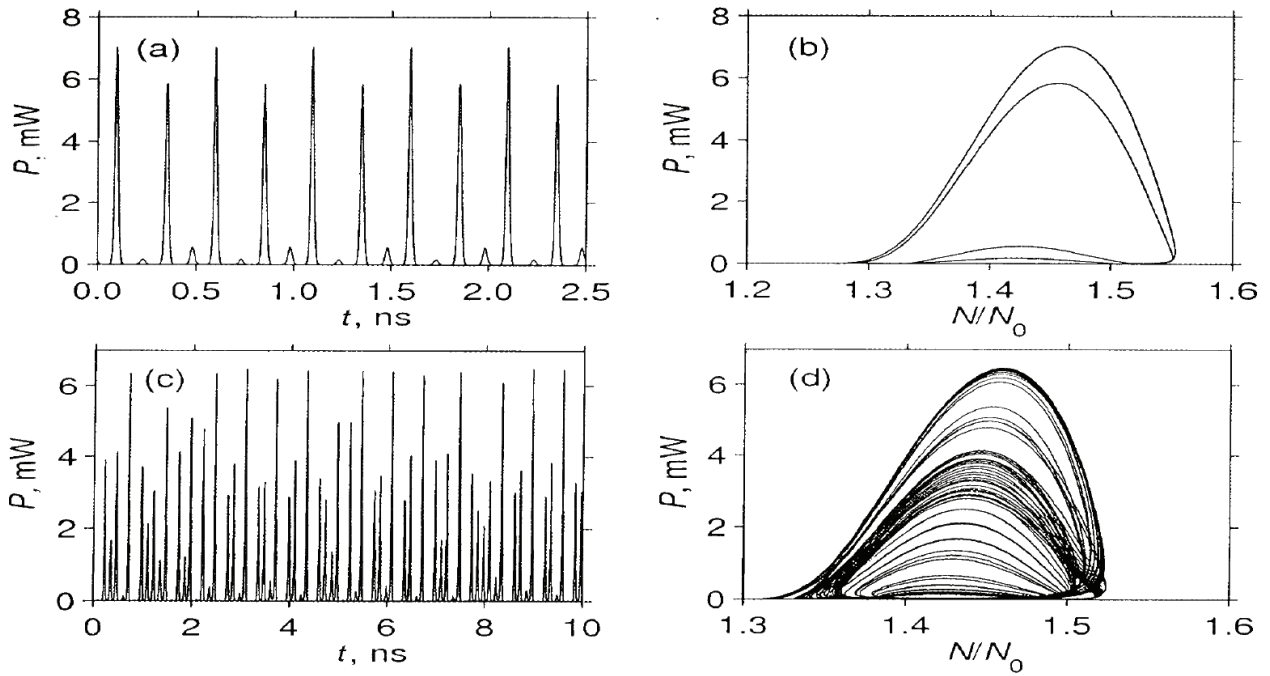


Figure 14. Nonlinear dynamics, temporal and in the phase space: (a, b) 4 T for $m = 3.5$ and (c, d) chaotic for $m = 5.5$.

4. Particularities of modeling and simulation of quantum well solar cells

This part of the chapter is dedicated to research results concerning the simulation of optical parameters (refraction index, reflectance, and the absorption coefficient) of the quantum well

(QW) photovoltaic cells, which represents the third generation of solar cells, proposed in 1990 by Keith Barnham [29, 30], aiming to extend the spectral response and to increase the photo-current of this kind of optoelectronics devices.

The quantum well solar cell is a p-i-n structure having quantum wells built in the intrinsic region. The doped parts on each side will produce an electric field perpendicular to the layers of quantum wells as is shown in [31]. The multiple quantum well solar cells (MQW) modeling is conducted at two levels dimensionally: a *quantum level* in which one computes the energy spectrum of the electron and the absorption coefficient of the MQW; a *macroscopic level* in which one studies the transport of charge carriers in a similar manner to the conventional p-i-n diode as in [30]. The reflection of light is brought, considering MQW cell a pseudo-homogeneous medium. This combination of quantum and classical elements used in the modeling of MQW solar cell justifies the name of *hybrid* given to the model of MQW solar cell. An example of the application of the hybrid model (HM) is given in [31]. It is the case of solar cell based on a ternary alloy semiconductor $A_xB_{1-x}C$ ($Al_xGa_{1-x}As/GaAs$) which has the lowest BC band gap = 0 and achieves the greatest value ($x = 1$) for the AC semiconductor band gap.

The hybrid model (HM) allows determining the configuration that leads to maximum conversion efficiency. This configuration can be designed, by using the transfer matrix method and the properties of the real materials. In other words, starting from a hypothetical system structure, the HM model allows optimization of the solar cell configuration in order to obtain maximum output electrical power, for a certain state of illumination as in [32].

4.1. Modeling and simulation of the cell reflectance

An important problem is to evaluate the effect of the quantum well number on the index of refraction and on the reflection losses, so the optimal number of the quantum well for the structure can be calculated [9].

In **Figure 15**, the results of the optical simulation of reflectance R dependence on the radiation wavelength for different thicknesses d of the anti-reflecting coating (ARC) are presented, in the case of anti-reflecting coating of SiO ($n_1 = 1.4$). Results obtained based on presented model are consistent with experimental data.

The simulation of refraction index and reflectance of the solar cells with quantum wells have been made with the Octave software, version 3.02. The cell reflectance can be calculated using the refraction indices of GaAs semiconductor and of the $Al_{0.3}Ga_{0.7}As$ alloy as in [30]:

$$n_{GaAs} = \begin{cases} \frac{3.24123 - \frac{4.8304085}{\lambda} + \frac{2.82482}{\lambda^2} - \frac{0.769037}{\lambda^3} + \frac{0.08198}{\lambda^4}}{1 - \frac{1.5308}{\lambda} + \frac{0.9123972}{\lambda^2} - \frac{0.2508648}{\lambda^3} + \frac{0.026769}{\lambda^4}} & \text{if } 0.325 < \lambda \leq 4 \\ \frac{2.8434068 - \frac{1.8916996}{\lambda} + \frac{0.4189801}{\lambda^2} - \frac{0.0308637}{\lambda^3}}{1 - \frac{0.682372}{\lambda} + \frac{0.154593}{\lambda^2} - \frac{0.01159}{\lambda^3}} & \text{if } 0.2 \leq \lambda \leq 0.325 \end{cases} \quad (33)$$

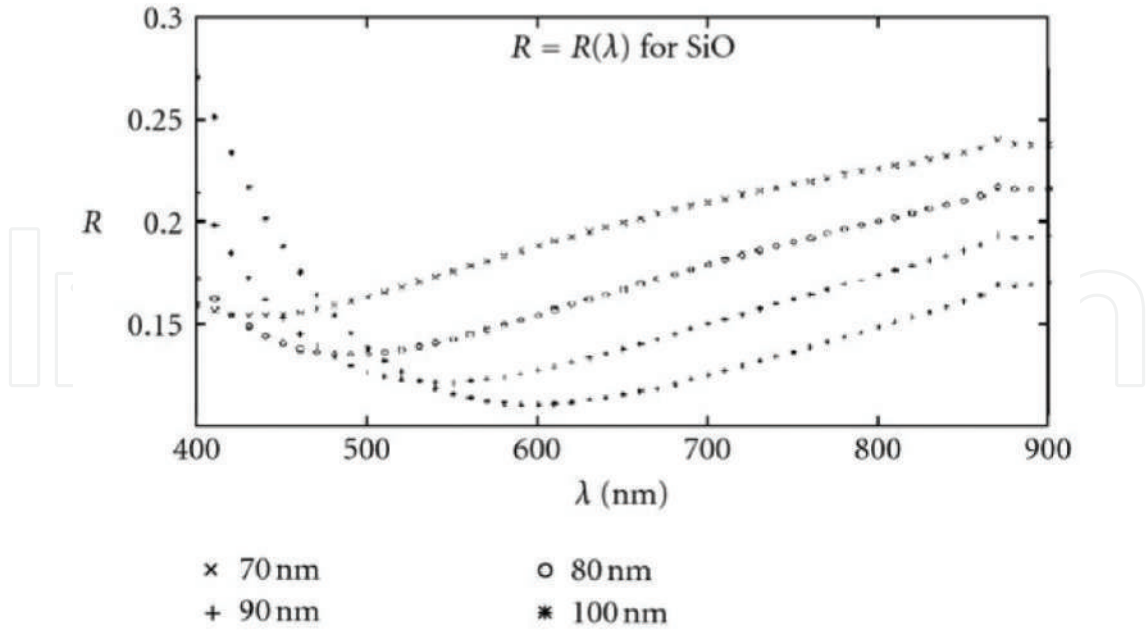


Figure 15. Simulation of the reflectance dependence of λ , for a solar cell QW structure with an SiO anti-reflecting coating.

In Eq. (33), λ is expressed in μm . The refraction index of ternary alloy $\text{Al}_x\text{Ga}_{1-x}\text{As}$ is calculated as.

$$n_{\text{Al}_x\text{Ga}_{1-x}\text{As}}(\lambda) = [1.05 - 0.53x + 0.09x^2]n_{\text{GaAs}}(\lambda_x) \quad (34)$$

with λ in μm

To minimize the reflection losses, the solar cells are frequently designed with anti-reflecting coating (ARC).

The MQW layer was considered to consist of 30 quantum wells of GaAs of 20-nm width separated by barriers $\text{Al}_{0.3}\text{Ga}_{0.7}\text{As}$ with a width of 10 nm.

4.2. Modeling and simulation of absorption coefficient

In applications related to calculating the conversion efficiency of solar cells, but also in other situations, the coefficient of absorption (the absorbance) is practically described by continuous functions. For GaAs, according to the experimental data shown in [30], the following function that approximates the acceptable rate of absorption was determined:

$$\alpha_{\text{GaAs}}(\lambda) = \begin{cases} e^{F_1(\lambda)}, & 0.7 < \lambda \leq 0.88 \\ e^{F_2(\lambda)}, & 0.24 < \lambda \leq 0.7 \\ e^{F_2(0.24)}, & 0 < \lambda \leq 0.24 \\ 0, & \text{otherwise} \end{cases} \quad (35)$$

$$F_1(\lambda) = -0.7863 + 5.3115 \left[1 + \text{erf} \left(-\frac{\lambda - 0.84291}{0.038} \right) \right] \quad (36)$$

$$F_2(\lambda) = -447.432 + 4201.2\lambda^2 + 6835.128\lambda^2 \ln \lambda - 3781.193\lambda^3 + \frac{3.9049}{\lambda^2} \quad (37)$$

In Ref. [30], the absorption coefficient for GaAs calculated with this model is represented.

4.3. Simulation of the quantum efficiency of QW solar cells

The analyzed model uses the transport equation of $\text{Al}_x\text{Ga}_{1-x}\text{As}$ quantum well solar cells, where x represents the aluminum concentration. The expression of the quantum efficiency (QE) is given by

$$QE \cong \frac{\alpha k(\alpha - S)}{(k^2 - \alpha^2)(S \sinh(kz) - k \cosh(kz))} \cong \frac{\alpha - S}{\alpha^2(S - 1)} \quad (38)$$

where α is the spectral absorption, ε_f is the effective electric field due to the minority carriers, and S a parameter.

From the analysis of the data obtained, it results that quantum efficiency increases with any increase in λ , reaching significant values of a maximum of 90%, in the case of large diffusion wavelength; quantum efficiency increases with any increase of z and ε_f , respectively.

In [30] for the cell parameters $N_w = 30$, $l_w = 20$ nm and $l_b = 10$ nm, the calculation results of the conversion efficiency are summarized.

In **Figure 16**, it is observed that the conversion efficiency is strongly correlated with the number of quantum well up to $N_w = 30$; above this value, the efficiency is saturated at larger

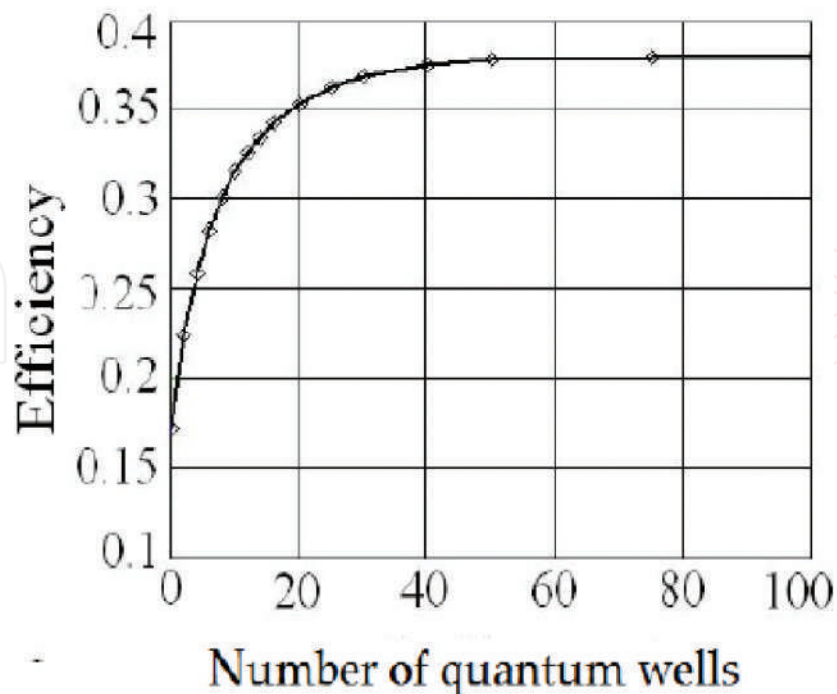


Figure 16. The dependence of the efficiency of MQW solar cell by the number of quantum wells.

values of Nw . The saturation is installed when the road length traveled by light is comparable with the absorption length. This result is a positive one by using the HM model. The calculation can be repeated varying different geometrical and material parameters in order to determine the optimal configuration, that is, one that maximizes efficiency.

Recently, good experimental results were reported in MQW solar cells. The fabricated solar cells based on $\text{In}_{0.3}\text{Ga}_{0.7}\text{N}/\text{GaN}$ MQWs exhibit an open circuit voltage of about 2 V, a fill factor of about 60%, and an external efficiency of 40% at 420 nm and 10% at 50 nm. New solar devices could be conceived based on optical properties of nanostructured materials [29, 30].

5. Optical transmission system with laser chaotic carrier

5.1. The Pecora-Carroll synchronization method

The method presented in this chapter focuses on the transmission of information by masking it in a chaotic signal, the amplitude of the message being added to that of the carrier. Two chaotic systems can be synchronized if they have similar parameters as is shown in Ref.s [35, 36]. This phenomenon has a very good potential application in coding the transmission of information. The transmission is made by using an emergent wave from a laser as a chaotic transmitter. The signal is attached to a carrier wave which is of a chaotic nature and has much higher amplitude. This ensures a higher degree of difficulty in intercepting and decoding. For attaching the signal to the carrier chaotic masking, modulation can be used. The properties of transmission and reception of the data as well as the synchronization of the lasers can be studied by using a pair of master–slave lasers. Modeling of the lasers is made by the use of the rate equations as in [35].

A communication scheme compatible with the Pecora-Carroll synchronization method given in [36, 40] is presented in **Figure 17**. The link between the master system and the slave subsystems in the transmission area is unidirectional. The encryption is done by using the chaotic signal of the slave system at the transmitter as carrier for the message. At the receiver, the slave system synchronizes with its replica at the transmitter through the one linking drive signal. This allows the extraction of the information from the total transmitted signal.

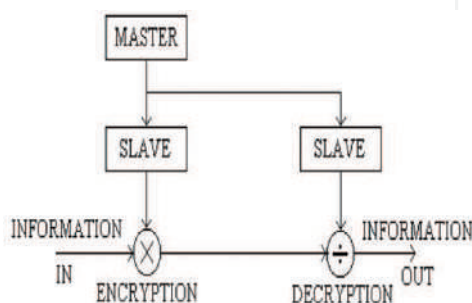


Figure 17. Block scheme of a communication system based on the synchronization of two chaotic subsystems.

5.2. Optical communications channel with chaotic laser carrier

It was shown that an amplitude modulator-demodulator with chaotic carrier can be implemented using a pair of self-pulsating laser diode (SPLDs), with closely matched parameters. If a sinusoidal injection current is superimposed over a polarization current for which self-pulsations occur, then the pulses become chaotic both in amplitude and in repetition interval. When the sinusoidal current is modulated with an information signal having amplitude and frequency much smaller than the disorder maker current, then the transmitted signal spectrum does not present a clear component having the frequency of the message, and the filtering operation is of no use in recovering the transmitted information. If a small part of the transmitted chaotic signal (SPLD-T) is coupled into the received signal (SPLD-R), the information can be recovered based on the property that the receiver output field synchronizes only with the chaotic carrier and not with the whole transmitted optical field. An SPLD is an active optical device able to produce a continuous train of pulses with repetition rate dependent on the injection current (**Figure 18**).

The self-pulsating laser diode (SPLD) is driven by an injection current $I^{R,T}(t)$:

$$I^{R,T} = I_{\text{bias}}^{R,T} + I_A^{R,T} \sin(2\pi ft) \quad (39)$$

where I_{bias} is the continuous component of the injection current, while I_A and f are the amplitude and frequency of a sinusoidal current superimposed over the continuous injection bias component, respectively. The laser parameters for numerical simulations can be found in [10]. It is noted that δ is the coupling factor of the transmitted field into the receiver SPLD.

If a sinusoidal current is superimposed over I_{bias} , then the self-pulsations became chaotic either in repetition interval or in amplitude (**Figure 19**). The two identical SPLD-R and SPLD-T have similar outputs but uncorrelated [35].

When a small part of the transmitted chaotic carrier is coupled into the receiver device, synchronization between the two lasers becomes possible (**Figures 20 and 21**), independently of the initial conditions of the two systems.

To investigate the possibility of transmission information, we introduce the information as an amplitude modulation of the sinusoidal injection current into the transmitter laser. For simplicity,

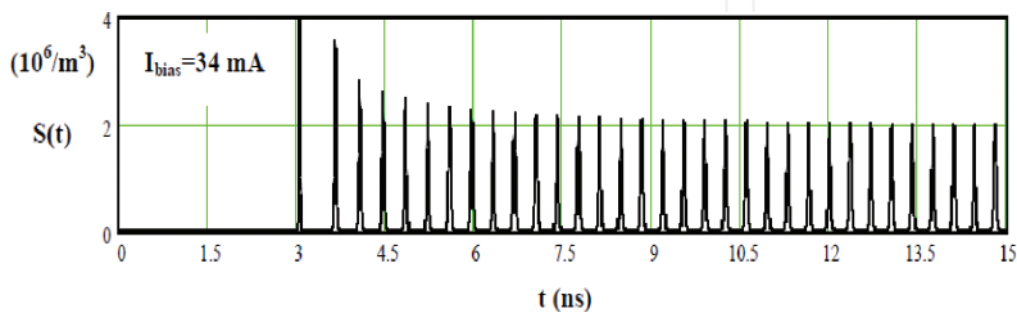


Figure 18. Temporal dynamics of SPLD for the injection current $I_{\text{bias}} = 34 \text{ mA}$.

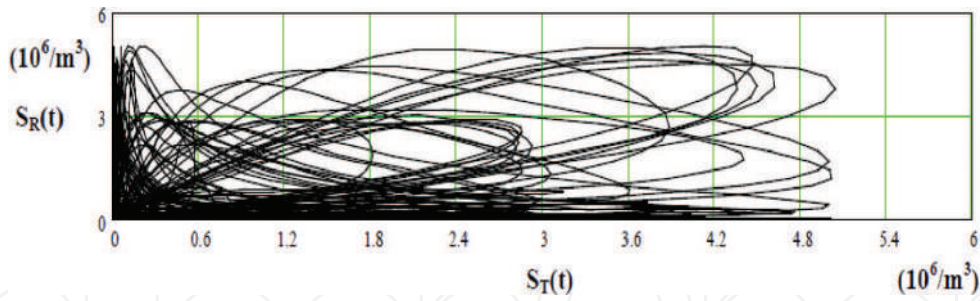


Figure 19. The output $S_R(t)$ of SPLD-R versus $S_T(t)$ SPLD-T. The two photon densities are not synchronized.

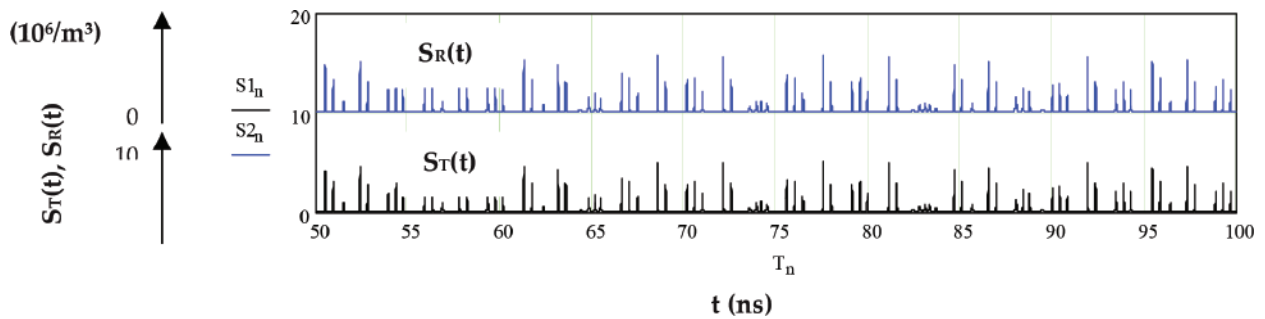


Figure 20. The graphical representation of the photon densities $S_R(t)$ and $S_T(t)$, synchronized, for $\delta = 0.04$.

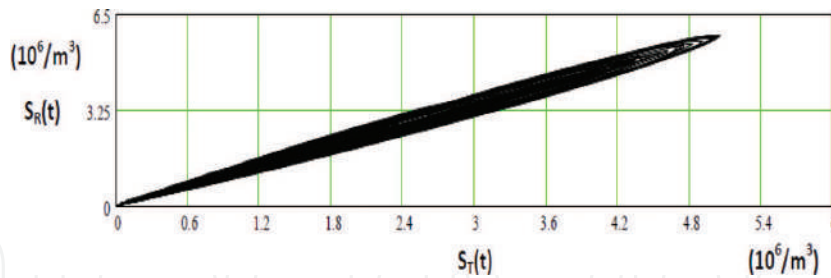


Figure 21. The output $S_R(t)$ of SPLD-R versus $S_T(t)$ SPLD-T. The two photon densities are closely synchronized.

we consider a sinusoidal message signal $I_m(t) = I_{m,A} \sin(2\pi f_m t)$, where $I_{m,A} \ll I_{bias}$ and $f_m \ll f$ for secrecy and small modulation distortion reasons. Numerical simulations show that the receiver output synchronizes with the carrier field, rather than to the transmitted signal; the decoded signal is obtained as $S_d(t) = S_T(t) - S_R(t)$ In **Figure 22**, a typical method of recovering information in such a kind of transmission is presented.

The useful message can be recovered by low filtering of the quantity $[S_T(t) - S_R(t)]/S_R(t)$. As SPLDs are widely available, cheap, and compact, their use in private communication systems, but not only, for transmissions with information encrypted is recommended.

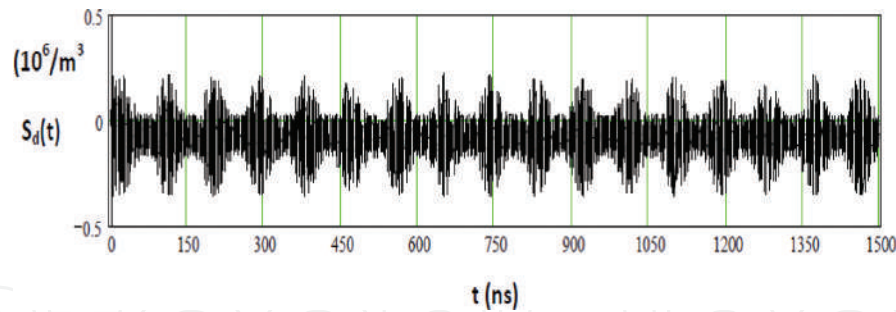


Figure 22. The decoded signal versus time. $S_d(t) = \frac{S_T(t) - S_R(t)}{S_R(t)}$ for $I_m(t) = (7/50)\sin[2\pi(f/50)t]$ mA.

6. Conclusions

The mathematical models presented in this chapter highlight the possibility of unitary, describing the nonlinear dynamics in the optoelectronics structures with quantum well fact which is essential for their design and applications.

The obtained results by numerical simulations show how the dynamics is characterized by bifurcation points and chaos, being close to those obtained experimentally and reported in the literature.

The results based on the hybrid model of the MQW solar cells show that the number of quantum well of the structure can be determined by numerical simulations for improving the conversion efficiency, based on optical properties of nanostructured materials used in research and fabrication.

The broadband modulation and the low injection current at the oscillation threshold of the quantum well lasers compared to bulk laser ones recommends these optoelectronics structures for high-speed optical communications, providing unwanted nonlinear effects as the points of bifurcation and chaos are avoided, for the stable operation and the control of their dynamics.

Conflict of interest

The authors declare that there is no conflict of interest regarding the publication of this chapter.

Author details

Andreea Rodica Sterian

Address all correspondence to: andreea.sterian1@yahoo.com

Faculty of Applied Sciences, Physics Department, Academic Center of Optical Engineering and Photonics, Polytechnic University of Bucharest, Bucharest, Romania

References

- [1] Weiss U. Quantum Dissipative Systems. Toh Tuck Kink, Singapore: World Scientific Publishing Co. Pte.Ltd.; 2012
- [2] Sterian PE. Analytical model of dissipative coupling coefficients in laser structures. Proceedings of the Romanian Academy A. 2002;3(3):123-126
- [3] Peter SZ, Zory J. Quantum Well Lasers. Vol. 347. Boston: Academic Press; 1993
- [4] Sterian P. Exact quantum master equations for Markoffian systems. Optical Engineering. 1996 Jun 1;35(6):1573-1575. DOI: 10.1117/1.601001
- [5] Sterian PE. Fotonica. Printech; 2000
- [6] Stefanescu E, Sterian AR, Sterian P. Study on the fermion systems coupled by electric dipol interaction with the free electromagnetic field. In: 21st European Mask and Lithography Conference 2005 Jun 7 (pp. 160–165). International Society for Optics and Photonics. DOI: 10.1117/12.63368
- [7] Sterian AR. Coherent radiation generation and amplification in erbium doped systems. In: Advances in Optical Amplifiers. Croatia: InTech; 2011
- [8] Iordache DA, Sterian P, Sterian AR, Pop F. Complex computer simulations, numerical artifacts, and numerical phenomena. International Journal of Computers Communications & Control. 2010 Dec 1;5(5):744-754. DOI: 10.15837/ijccc.2010.5.2234
- [9] Barnham KW, Duggan G. A new approach to high-efficiency multi-band-gap solar cells. Journal of Applied Physics. 1990 Apr 1;67(7):3490-3493. DOI: 10.1063/1.345339
- [10] Sterian AR. Amplificatoare optice. Editura Printech; 2006. DOI: 10.1109/3.748833
- [11] Ghoniemy S, MacEachern L, Mahmoud S. Extended robust semiconductor laser modeling for analog optical link simulations. IEEE Journal of Selected Topics in Quantum Electronics. 2003 May;9(3):872-878. DOI: 10.1109/JSTQE.2003.818841
- [12] Sterian AR. Numerical simulations on nonlinear dynamics in lasers as related high energy physics phenomena. Advances in High Energy Physics. 2013 Oct 27;2013. DOI: 10.1155/2013/516396
- [13] Sterian AR. The structure of an automatic decision system for a large number of independent particle detectors. Advances in High Energy Physics. 2013 Mar 10;2013. DOI: 10.1155/2013/839570
- [14] Anghel DA, Sterian AR, Sterian PE. Modeling quantum well lasers. Mathematical Problems in Engineering. 2012 Mar 7;2012. DOI: 10.1155/2012/736529
- [15] Tsou BP, Pulfrey DL. A versatile SPICE model for quantum-well lasers. IEEE Journal of Quantum Electronics. 1997 Feb;33(2):246-254. DOI: 10.1109/3.552265
- [16] Dehghan M, Derakhshan P. A novel dynamic analysis and simulation for quantum-well distributed feedback laser,(qw-dfb). Progress in Electromagnetics Research B. 2008;3:105-114

- [17] Popescu IM, Preda AM, Tudorache SS. *Aplicatii ale laserilor*. Bucuresti: Tehnica; 1979
- [18] Gao DS, Kang SM, Bryan RP, Coleman JJ. Modeling of quantum-well lasers for computer-aided analysis of optoelectronic integrated circuits. *IEEE Journal of Quantum Electronics*. 1990 Jul;**26**(7):1206-1216. DOI: 10.1109/3.59660
- [19] Javro SA, Kang SM. Transforming Tucker's linearization laser rate equations to a form that has a single solution regime. *Journal of Lightwave Technology*. 1995 Sep;**13**(9):1899-1904. DOI: 10.1109/50.464741
- [20] Mena PV, Kang SM, DeTemple TA. Rate-equation-based laser models with a single solution regime. *Journal of lightwave Technology*. 1997 Apr;**15**(4):717-730. DOI: 10.1109/50.566695
- [21] Sterian AR. Computer modeling of the coherent optical amplifier and laser systems. In: *International Conference on Computational Science and Its Applications 2007 Aug 26*. Springer, Berlin, Heidelberg. pp. 436-449
- [22] Bulinski M, Pascu ML. Chaos in laser diode light emission. *Romanian Journal of Optoelectronics*. 2001 Apr;**9**(2):1-34
- [23] Lee CH, Yoon TH, Shin SY. Period doubling and chaos in a directly modulated laser diode. *Applied Physics Letters*. 1985 Jan 1;**46**(1):95-97. DOI: 10.1063/1.95810
- [24] Bennett S, Snowden CM, Iezekiel S. Nonlinear dynamics in directly modulated multiple-quantum-well laser diodes. *IEEE Journal of Quantum Electronics*. 1997 Nov;**33**(11):2076-2083. DOI: 10.1109/3.641323
- [25] Ninulescu V, Nicolae VB, Sterian A. Quantum well lasers for medical industry. In *BIRD*. 2008. pp. 563-570
- [26] Nagarajan R, Ishikawa M, Fukushima T, Geels RS, Bowers JE. High speed quantum-well lasers and carrier transport effects. *IEEE Journal of Quantum Electronics*. 1992 Oct;**28**(10):1990-2008. DOI: 10.1109/3.159508
- [27] Marcuse DI. Computer simulation of laser photon fluctuations: Theory of single-cavity laser. *IEEE Journal of Quantum Electronics*. 1984 Oct;**20**(10):1139-1148. DOI: 10.1109/JQE.1984.1072276
- [28] Sterian AR, Ninulescu V, Sterian L. Modulated laser diode for medical applications. In: *Proc. of SPIE Vol 2004 Oct 21 Vol. 5581*. p. 275. DOI: 10.1117/12.582837
- [29] Barnham KW, Barnes JM, Braun B, Connolly JP, Haarpaintner G, Nelson JA, Paxman M, Button C, Roberts JS, Foxon CT. A novel approach to higher efficiency-the quantum well solar cell. In: *Proceedings of the 11th EC Photovoltaic Solar Energy Conference 1992* pp. 146-149
- [30] Fara L, editor. *Advanced Solar Cell Materials, Technology, Modeling, and Simulation*. IGI Global; 2012 Jul 31
- [31] Fara S, Sterian P, Fara L, Iancu M, Sterian A. New results in optical modelling of quantum well solar cells. *International Journal of Photoenergy*. 2012 May 16:2012. DOI: 10.1155/2012/810801

- [32] Fara L, Moraru AG, Sterian P, Bobei AP, Diaconu A, Fara S. Building integrated photovoltaic (BIPV) systems in Romania. Monitoring, modelling and experimental validation. *Journal of Optoelectronics and Advanced Materials*. 2013 Jan 1;**15**(1–2):125-130
- [33] Iordache DA, Sterian PE, Tunaru I. Charge coupled devices as particle detectors. *Advances in High Energy Physics*. 2013 Mar;**19**:2013. DOI: 10.1155/2012/810801
- [34] Popescu DG, Sterian P. Photonic crystal fiber mode characterization with multipole method. *UPB Scientific Bulletin, A Series*. Bucharest: University “Politehnica” of Bucharest; 2013 Jan 1;**75**:205-215
- [35] Sterian P, Ninulescu V, Sterian AR, Lazar B. Optical communication methods based on chaotic laser signals. *University Politehnica of Bucharest scientific bulletin-series A-applied mathematics and. Physics*. 2010 Jan 1;**72**(1):83-94
- [36] Pecora LM, Carroll TL. Driving systems with chaotic signals. *Physical Review A*. 1991 Aug 1;**44**(4):2374. DOI: 10.1103/PhysRevA.44.2374
- [37] Sterian PE. *Transmisia optica a informatiei*. Bucharest: Editura Tehnică; 1981
- [38] FAZACAȘ A, Sterian P. Propagation of the Raman soliton in optical fibers. *Romanian Reports in Physics*. 2013;**65**(4):1420-1430
- [39] Sanchez-Diaz A, Mirasso CR, Colet P, Garcia-Fernandez P. Encoded Gbit/s digital communications with synchronized chaotic semiconductor lasers. *IEEE journal of quantum electronics*. 1999 Mar;**35**(3):292-297
- [40] Sterian PE. Communication based on chaotic signals. *Proceedings of the Romanian Academy*. 2002;**3**(1–2):45-48

We are IntechOpen, the world's leading publisher of Open Access books Built by scientists, for scientists

6,300

Open access books available

171,000

International authors and editors

190M

Downloads

Our authors are among the

154

Countries delivered to

TOP 1%

most cited scientists

12.2%

Contributors from top 500 universities



WEB OF SCIENCE™

Selection of our books indexed in the Book Citation Index
in Web of Science™ Core Collection (BKCI)

Interested in publishing with us?
Contact book.department@intechopen.com

Numbers displayed above are based on latest data collected.
For more information visit www.intechopen.com



Infrared Sensors for Autonomous Vehicles

Rajeev Thakur

Additional information is available at the end of the chapter

<http://dx.doi.org/10.5772/intechopen.70577>

Abstract

The spurt in interest and development of Autonomous vehicles is a continuing boost to the growth of electronic devices in the automotive industry. The sensing, processing, activation, feedback and control functions done by the human brain have to be replaced with electronics. The task is proving to be exhilarating and daunting at the same time. The environment sensors – RADAR (Radio Detection And Ranging), Camera and LIDAR (Light Detection And Ranging) are enjoying a lot attention with the need for increasingly greater range and resolution being demanded by the “eyes” and faster computation by the “brain”. Even though all three and more sensors (Ultrasonic / Stereo Camera / GPS / etc.) will be used together; this chapter will focus on challenges facing Camera and LIDAR. Anywhere from 2 – 8 cameras and 1 – 2 LIDAR are expected to be part of the sensor suite needed by Autonomous vehicles – which have to function equally well in day and night. Near infrared (800 – 1000nm) devices are currently emitters of choice in these sensors. Higher range, resolution and Field of view pose many challenges to overcome with new electronic device innovations before we realize the safety and other benefits of autonomous vehicles.

Keywords: autonomous vehicles, infrared, sensors, LIDAR, camera

1. Introduction

The Federal Automated Vehicles Policy [2] document released by NHTSA in September 2016 states that 35,092 people died on US roadways in 2015 and 94% of the crashes were attributed to human error. Highly automated vehicles (HAVs) have the potential to mitigate most of these crashes. They also have such advantages as not being emotional, not fatiguing like humans, learning from past mistakes of their own and other HAVs, being able to use complementary technologies like Vehicle-to-Vehicle (V2V) and Vehicle-to-Infrastructure (V2I) – which could further enhance system performance. Add in the potential to save energy

Level	Name	Narrative definition	Dynamic Driving Task (DDT)		DDT fallback	Operational Design Domain (ODD)
			Sustained lateral and longitudinal vehicle motion control	Object and Event Detection and Response (OEDR)		
Driver performs part or all of the Dynamic Driving Task (DDT)						
0	No Driving Automation	The performance by the <i>driver</i> of the entire <i>DDT</i> , even when enhanced by <i>active safety systems</i> .	<i>Driver</i>	<i>Driver</i>	<i>Driver</i>	n/a
1	Driver Assistance	The <i>sustained</i> and <i>ODD</i> -specific execution by a <i>driving automation system</i> of either the <i>lateral</i> or the <i>longitudinal vehicle motion control</i> subtask of the <i>DDT</i> (but not both simultaneously) with the expectation that the <i>driver</i> performs the remainder of the <i>DDT</i> .	<i>Driver</i> and <i>System</i>	<i>Driver</i>	<i>Driver</i>	Limited
2	Partial Driving Automation	The <i>sustained</i> and <i>ODD</i> -specific execution by a <i>driving automation system</i> of both the <i>lateral</i> and <i>longitudinal vehicle motion control</i> subtasks of the <i>DDT</i> with the expectation that the <i>driver</i> completes the <i>OEDR</i> subtask and <i>supervises</i> the <i>driving automation system</i> .	System	<i>Driver</i>	<i>Driver</i>	Limited
Automated Driving System (“System”) performs the entire DDT (while engaged)						
3	Conditional Driving Automation	The <i>sustained</i> and <i>ODD</i> -specific performance by an <i>ADS</i> of the entire <i>DDT</i> with the expectation that the <i>DDT fallback-ready user</i> is <i>receptive</i> to <i>ADS</i> -issued <i>requests to intervene</i> , as well as to <i>DDT performance-relevant system failures</i> in other <i>vehicle systems</i> , and will respond appropriately.	<i>System</i>	<i>System</i>	<i>Fallback ready user (Driver is fallback)</i>	Limited
4	High Driving Automation	The <i>sustained</i> and <i>ODD</i> -specific performance by an <i>ADS</i> of the entire <i>DDT</i> and <i>DDT fallback</i> without any expectation that a <i>user</i> will respond to a <i>request to intervene</i> .	<i>System</i>	<i>System</i>	<i>System</i>	Limited
5	Full Driving Automation	The <i>sustained</i> and unconditional (i.e., not <i>ODD</i> -specific) performance by an <i>ADS</i> of the entire <i>DDT</i> and <i>DDT fallback</i> without any expectation that a <i>user</i> will respond to a <i>request to intervene</i> .	<i>System</i>	<i>System</i>	<i>System</i>	Unlimited

Table 1. SAE J3016 – summary of levels of driving automation [3].

and reduce pollution (better fuel economy, ride sharing and electrification) – creating a huge impetus to implement autonomous vehicle technology as soon as possible.

On the other hand we have the consumer industry from Silicon Valley eyeing autonomous vehicles as a huge platform to engage, interact, customize and monetize the user experience. Think online shopping, watching a movie, doing your email or office work, video chats, customized advertisements based on user profile and location, etc. – all while our transport takes us to our destination. The innovation and business potential presented by the HAVs is only limited by imagination and savvy to overcome the challenges.

Among the various challenges to overcome are those of sensing the environment around and even inside the vehicle. Two of these sensing technologies are LIDAR and camera. Each of them are evolving fast to meet the industry demands. Levels 3–5 of autonomous vehicles as defined by NHTSA and SAE (**Table 1**) will need a high resolution and long range scanning LIDAR [3]. They will also need cameras which operate in infrared (and visible) spectrum to be able to function at night and low light conditions.

We will start with discussing the infrared spectrum, its advantages and disadvantages and then move onto LIDAR and Camera in some level of detail.

2. Infrared spectrum

2.1. Infrared radiation

The sun radiates electromagnetic energy in a wide spectrum from the shortest X-rays to radio waves. **Figure 1** shows the portion visible to the human eye (~380–750 nm) and the infrared region [4]. The near infrared region (~750–1400 nm) is used in many sensing applications

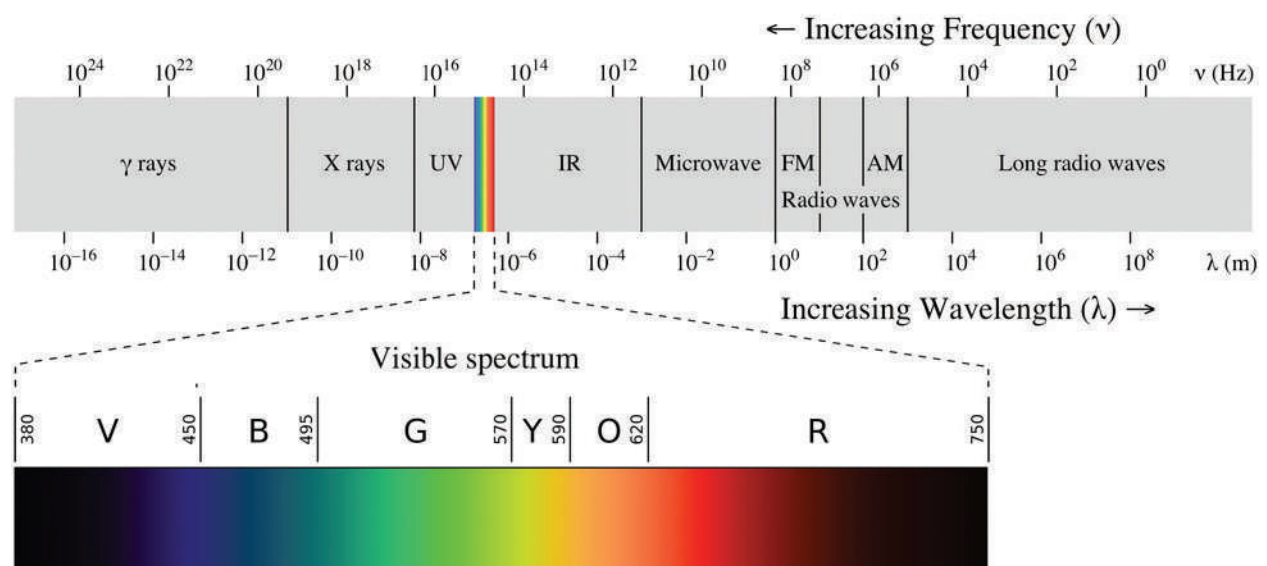


Figure 1. Electromagnetic spectrum with visible light highlighted [4].

including the night vision camera and LIDAR. The active night vision cameras (use light from artificial sources) are different from the passive thermal imaging cameras which operate at higher wavelengths (8–15 μm) and use natural heat as sources of radiation. **Figure 1** also shows the wide range of infrared radiation from 750 nm to 1 mm wavelength.

2.2. Sensitivity

Figure 2 shows the human eye and camera sensitivity to the visible – Near infrared (NIR) spectrum. The advantage and disadvantage for sensing applications primarily arises from the fact that infrared is mostly invisible in the far field. A fair amount of red color can be seen by most humans till 850 nm; beyond that lies a fair amount of subjectivity. The fact that the human eye is not very sensitive to NIR light allows cameras to be used unobtrusively (especially at night/poor lighting conditions). The disadvantage lies in the fact that silicon based image sensors have poor sensitivity in this wavelength (~35% QE at 850 and 10% at 940 nm). In addition these wavelengths can reach the retina of the eye – so the exposure has to be controlled to avoid damage.

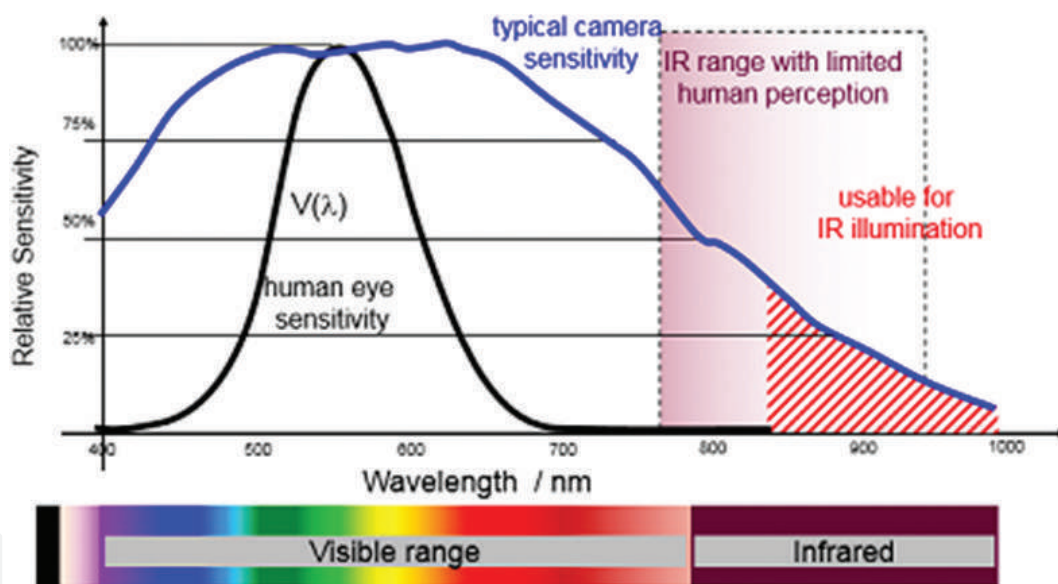


Figure 2. Sensitivity of photo detectors and cameras vs. human eye.

2.3. Spectral irradiance

The solar radiation outside the earth's atmosphere and that reaching the surface is shown in **Figure 3** [8].

Dips in the spectral irradiance at surface are primarily due to water in the atmosphere. In the infrared spectrum of interest they occur at 810, 935, 1130, 1380, 1880 nm and beyond. This means the ambient noise is lower at these specific wavelengths. However, wavelengths of many semiconductor devices shift with temperature ($\sim 0.3 \text{ nm}/^\circ\text{C}$ for Gallium arsenide and aluminum gallium

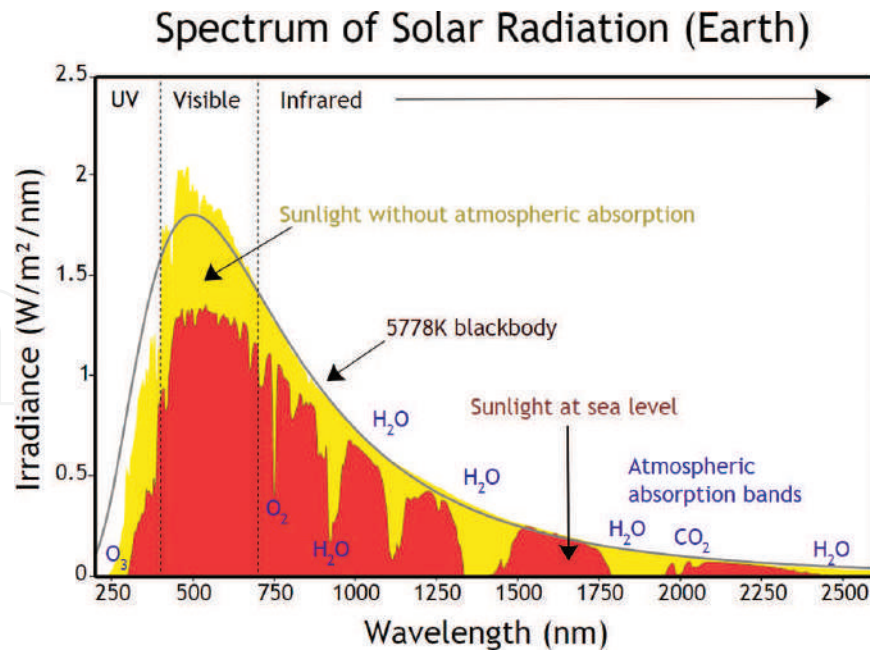


Figure 3. Solar spectral irradiance on earth [8].

arsenide materials used in infrared spectrum); for automotive applications this shift is ~44 nm from -40 to 105°C. Ideally we need a peak with flat ambient noise variation around it for good design.

Another observation from **Figure 3** is the lower ambient noise as we go to the longer wavelengths. However, past ~1000 nm the material base for detectors changes from silicon to germanium or indium gallium arsenide – which can be expensive.

3. Light Detection And Ranging (LIDAR)

3.1. Need for LIDAR in automotive

LIDAR, Radio Detection And Ranging (RADAR) and Camera are the environment sensors central to the autonomous car operation. They are used to detect and classify the objects around the car by location and velocity. Each of the sensors has limitations and the information obtained from them is fused together with confidence prior to making a decision on the vehicles trajectory.

Table 2 provides a brief summary of the above sensing technologies.

3.2. Types

LIDAR sensors could be classified on any of its various key parameters:

- Operating principle: Time of Flight (ToF)/Frequency Modulated Continuous Wave (FMCW)

- Scanning technology: Mechanical/Micro-Mechanical-Mirror (MEMS)/Optical Phase Array (OPA)
- Scanning/Flash
- Solid State/Mechanical
- Wavelength: 905 /1550 nm
- Detection technology: Photodiode/Avalanche Photodiode/Single Photon Multiplier
- ...and many other ways

Sensor	Typical range	Horizontal FOV	Vertical FOV	2020 price range	Comments
24 GHz RADAR	60 m [6]	56° [6]	~±20°	<\$100	USA Bandwidth Max 250 MHz [7] Robust to snow/rain Poor angular resolution; sensitive to installation tolerances and materials
77 GHz RADAR	200 m [6]	18° [6]	~±5°	<\$100	Similar to 24 GHz RADAR with more bandwidth (600 MHz [7]); sensitive to installation tolerances and materials
Front Mono Camera	50 m [6]	36° [6]	~±14°	<\$100	Versatile sensor with high resolution; Poor depth perception; High processing needs; low range; sensitive to dirt/obstruction
LIDAR (Flash)	75 m	140°	~±5°	<\$100	Better resolution than RADAR and more range than Camera. Eye safety limits; Poor in bad weather; sensitive to dirt/obstruction
LIDAR (Scanning)	200 m	360°	~±14°	<\$500	Similar to Flash LIDAR with higher resolution and Cost; sensitive to dirt/obstruction

Table 2. RADAR – camera – LIDAR comparison.

3.3. Time of Flight LIDAR Operating Principle

The Time of Flight LIDAR operation can be explained using **Figure 4**.

A laser is used to illuminate or “FLASH” the field of view to be sensed. The laser pulse travels till it is reflected off a target and returned to a detector. The time taken for the pulse to travel back and forth provides the range. The location of the target is based off optics mapped over the field of view and detector array. Two or more pulses from the target provide the velocity. The angular resolution depends on the number of detector pixels which map the field of view. The more pixels we have – the better the resolution.

The same principle is used by 3D cameras or high resolution flash LIDAR. Higher power and more detector pixels are used.

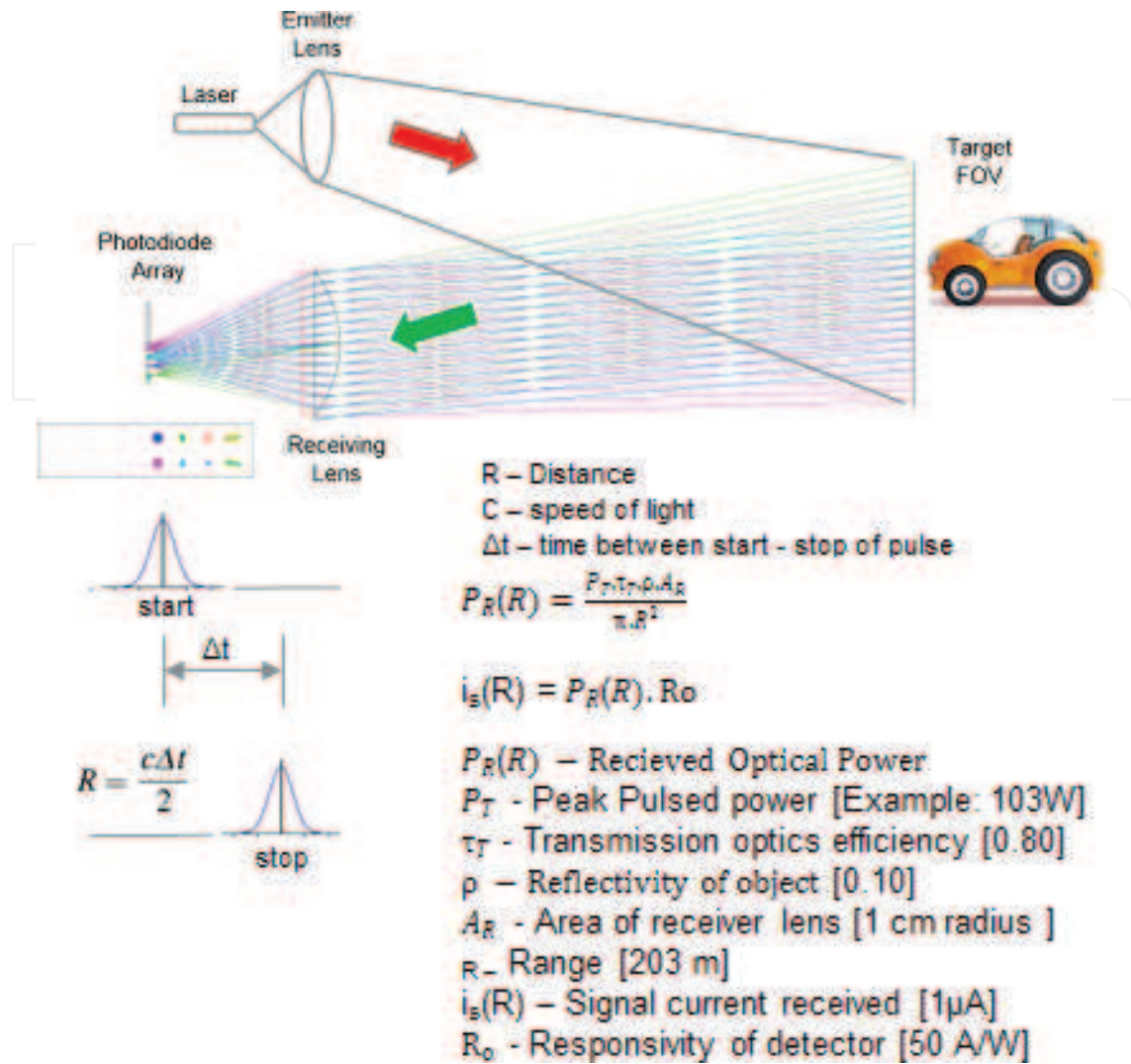


Figure 4. Time-of-Flight FLASH LIDAR.

3.4. Emitter and detector options

As shown in **Figure 4**, to increase the range by 2× – the needed power is 4×. As we increase the power – we start running into eye safety limits. Infrared light below 1400 nm can reach the retina of the eye. If the exposure limit is exceeded, permanent eye damage can occur.

There are many levers available to achieve the needed range – including better detectors, bigger lenses, and shorter pulse widths. Of course, the best option would be to use light above the 1400 nm wavelength. However, to use lasers and detectors in this wavelength region (>1400 nm) – we typically have to use more expensive materials (indium-gallium-arsenide – phosphide lasers and germanium-based detectors).

3.5. Eye safety

Sunlight on the earth’s surface is composed of ~52% infrared (>700 nm), ~43% visible (400–700 nm) and ~3% Ultraviolet (<400 nm) [9]. The intensity of infrared is low enough that it does not cause

eye damage under normal exposure. When light is visible and bright, the eye has a natural blink response and we do not stare at it – helping to avoid eye damage. Infrared light is not visible and so can cause eye damage if exposure limits are not regulated.

The safe levels of infrared levels are regulated by IEC-62471 for Light Emitting Diodes and IEC-60825 (2014) for lasers. In USA, the equivalent federal standards are in 21 CFR 1040 (Code of Federal Regulations).

The standards have hazard exposure limits for the cornea of the eye, thermal hazard limit for skin and eye retinal thermal hazard exposure. For exposures above 1000 s, the irradiance limit is 100 W/m² at room temperature and 400 W/m² at 0°C. The retina exposure limits tend to be more stringent. The calculations are complex and depend on wavelength, size of the emitter, exposure time and other factors.

3.6. Signal processing challenges

As sensors demand higher resolution and faster response – it increase the computational needs. At the raw signal level, using the forward camera as an example:

Number of pixels to be processed = frames per seconds × horizontal field of view/resolution × vertical field of view/resolution.

Example: 30 fps camera, 40° HFOV, 40° VFOV, 0.1° resolution

- $30 \times 400 \times 400 = 4.8 \text{ Mpx/s}$

A similar amount of data needs to be processed by the LIDAR, RADAR and other sensors. At some level, this information has to be fused to recognize and classify objects and their trajectory.

As more and more sensing data is collected, processed and acted upon in real time (time between collection and use is extremely short), creating ways of storing/processing and updating data are being developed. For example – the 3 dimensional roadway maps needed for autonomous driving are stored in the cloud (remote server) and real time data is processed to look only for changes and updates; thus reducing the amount of data crunching to be done in real time. Another trend is to collect and process the raw analog signal when possible – thus reducing the downstream processing needs.

Security of data in autonomous vehicles is another growing concern and business opportunity for innovation. Automotive Information Sharing and Analysis Center (Auto-ISAC) (www.automotiveisac.com) was formed in 2015 by automakers to share the best practices related to cyber threats in the connected car.

4. Camera

Camera's in automobiles continue to grow as their functional versatility is exploited with increasing innovation. They have become central to Advanced Driver Assistance Systems

(ADAS) like adaptive cruise control, adaptive high beam, automatic emergency braking, lane departure warning, blind spot detection, driver monitoring, traffic sign detection and others.

The latest Tesla Model 3 is believed to have up to eight exterior cameras. Other OEM's are also using interior driver monitoring and gesture recognition cameras. A presentation from IHS Markit [13] shows typically five exterior and one interior camera for Level 3; eight exterior cameras and 1 interior camera for Level 4 being planned by a number of Original Equipment Manufacturers.

4.1. Exterior infrared camera (night vision)

Cameras need light to illuminate the objects in its field of view. Currently most cameras used in ADAS functions work with visible light – which is fine for daytime operation. However, at night the prime source for visible light is usually the headlamps of the car. The visible light from the headlamps is strictly regulated by NHTSA with its Federal Motor Vehicles Safety Standard 108 (FMVSS 108). **Figure 5** below shows a bird's eye view of the permitted illumination region in the USA.

It can be observed that in essence, visible light can only be legally used for a limited range of ~60 m in front of the vehicle. Illumination outside the car lane and around the car is very limited (if any). These legal requirements are not expected to be changed anytime soon – since we will have cars driven by humans for at least another 20–30 years. This means to illuminate to longer and wider fields of view, the cameras have to work with infrared light (which is not regulated by FMVSS 108). As long as the infrared light is within eye safe limits, it can be used all around the car.

Figure 6 shows a graphic overview of the regions around the car that are covered by cameras. The forward camera needs to ideally sense as far as the RADAR and LIDAR to permit good sensor fusion.

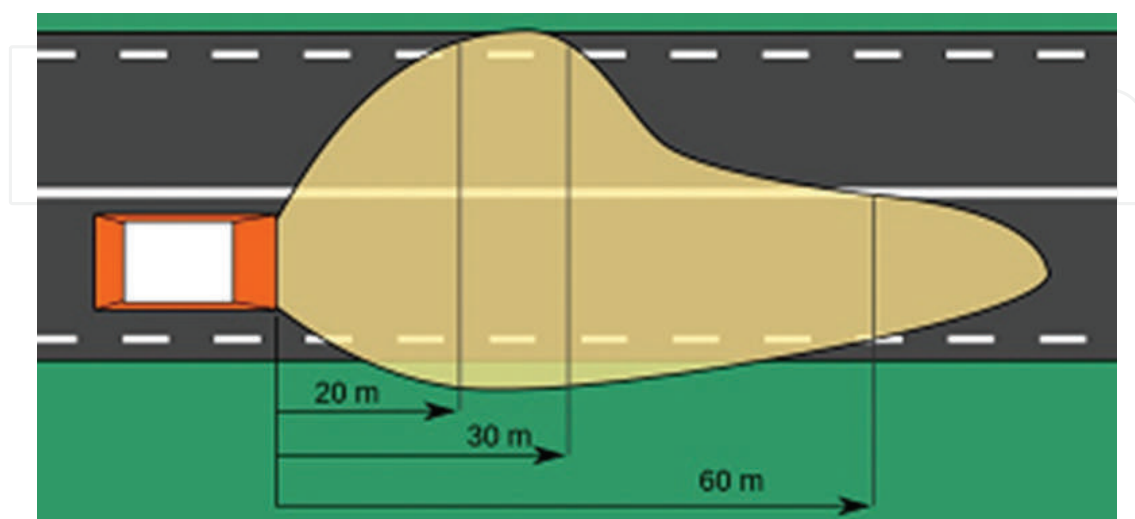


Figure 5. FMVSS 108 low beam visible light illumination.

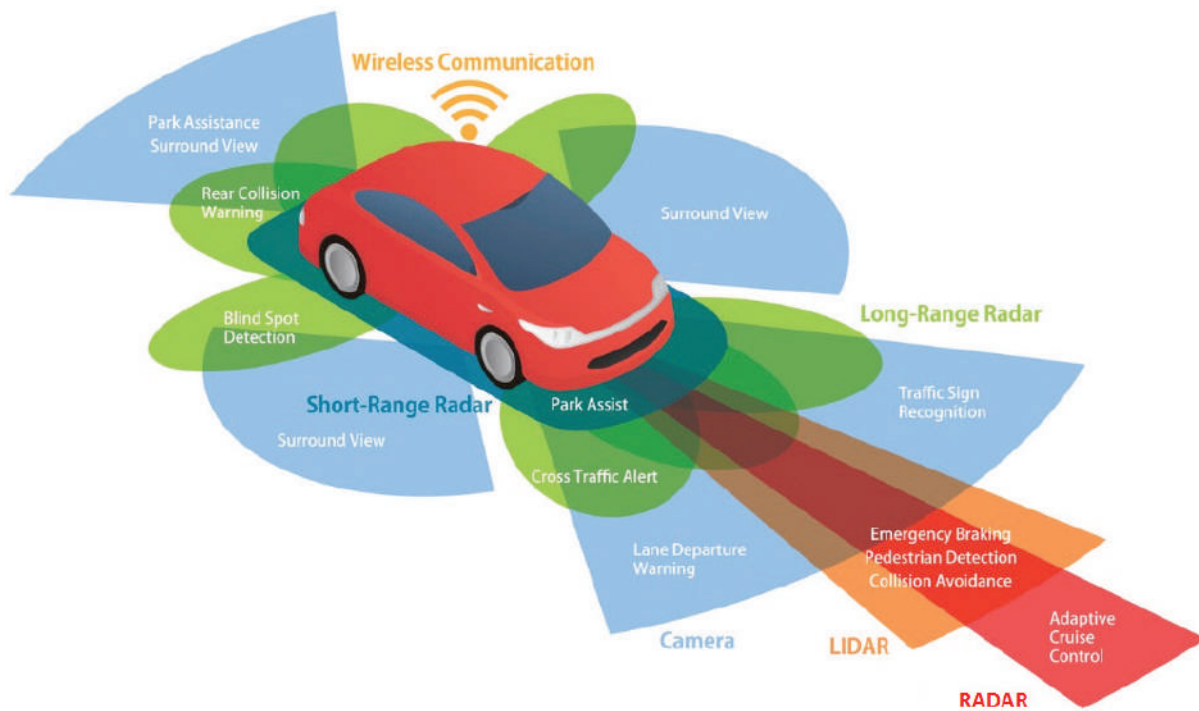


Figure 6. Environment sensors needed for autonomous cars.

The target range for RADAR and LIDAR is at least 200 m (Forward direction) and 50–100 m in all other directions.

4.2. Exterior camera illumination challenges

The spectral sensitivity of CMOS image sensors at 850 nm is ~35% compared to its peak at 550 nm (green). Further down at 940 nm, this reduces to ~10%. This means a larger number of infrared photons is needed to generate a clear image.

To illuminate targets at longer ranges and wider field of view more light is needed. In addition, different targets have different reflectivity – which can have a significant effect on the image quality. So while we put out more and more light to get a better signal – we need to ensure the intensity is still eye safe. We also start eating up more energy from the battery for illumination. Calculations show the amount of infrared flux needed could be anywhere from 6 W (100 m range, 12° FOV, 50% reflectivity, 850 nm, 0.15 $\mu\text{W}/\text{cm}^2$, Lens F#1) to 1250 W (200 m range, 40° FOV, 10% reflectivity, 850 nm, 0.15 $\mu\text{W}/\text{cm}^2$, Lens F#1) [10, 11].

A typical headlamp today may have 5 W of visible light used per lamp currently. Imagine the complexity of adding 100's of more Watts to the headlamp. The self-driving eco system has not yet come to grasp the scope of challenge that it has to deal with here. The alternative would be to rely more on the LIDAR and RADAR sensors at the longer ranges and use the camera only in the short ranges. This option may not provide needed reliability – since all of these technologies have weakness (RADAR does not same resolution as camera at long ranges and LIDAR is more prone to poor performance in bad weather).

Potential solution options which have not been fully vetted are to use pulsed infrared lasers to illuminate the CMOS based cameras; use of infrared matrix lighting architectures where rows of LED's are turned on in sequence with a rolling shutter camera more to come as we make progress.

4.3. Interior camera – market need

The need for an interior camera arises out of multiple market forces. The first is the introduction of self-driving cars which are autonomous only in certain driving conditions (highways/traffic Jams). The cars switch between the human driver and the computer as needed. To do this effectively, the human driver has to be monitored as part of the environment in and around the car. This is to ensure adequate warning is given to the driver to leave their current engagement and get ready to take over the task of driving.

The second market force is the increase of distracted driving. In 2014, 3179 (10% of Total) people were killed and an additional 431,000 (18% of total) were injured in collisions involving distracted drivers in the USA [10]. NHTSA has a blueprint to reduce accidents related to distracted driving – which encourages OEM's to put in place measures to ensure the driver keeps their eyes on the road when the vehicle is moving. A definition of distraction in terms of driver gaze and time elapsed away from looking straight is provided in other-related NHTSA documents [12]. At a high level, looking more than 2 s in a direction 30° sideways of up-down when the vehicle speed is more than 5 mph would be classified as distracted. The increase in distracted driving is attributed to cell phone/smartphone/texting and related activities.

Additional benefits and applications are continuing to generate from the driver monitoring infrared camera system. It lends itself well to also catch drowsy drivers (eyelids shut or drowsy pupils); face recognition – not strong enough to be a biometric device, but enough to at least enable customized settings for different drivers in family and many more to come.

The auto industry is responding to these two needs (autonomous cars, distracted driving) by installing an infrared camera to monitor the gaze of the driver. Infrared illumination is needed – since we do not want to distract the driver at night with visible light. The wavelength for illumination is in the 850–950 nm range. The eye safety and camera sensitivity challenges of illumination in this spectrum were briefly discussed earlier sections. A few other challenges are discussed in the next section.

4.4. Interior camera illumination challenges

When we use an infrared camera facing the driver, the LED's are shining the light right on our eyes and face. Light at 850 nm can be red enough to be seen easily by most people – especially at night. Measures to put in a dark filter and smudge the bright red LED spot with optics are partially successful. The problem arises from the fact that anything done to reduce the brightness will usually also reduce the illumination – which would result in poor image quality and failure to detect distraction in gaze by the software processing the image.

One solution is to go to higher wavelengths (940 nm) – the challenge here is lower camera sensitivity. This has been overcome by pulsing higher peak currents at lower duty cycle using a global shutter image sensor. The typical cameras used are 30 fps and these are fast enough – since gaze while driving does not change that often and fast.

On the eye safety side, measures are needed to ensure that when the eyes are too close to the Infrared LED (IRED) – then they either need to be shutoff or reduced in intensity. Typically the distance to the eye is estimated with the camera itself, as an added measure we can have proximity sensors.

Since these cameras work in infrared with a filter block for visible wavelengths, the biggest challenge for illumination tends to be during daytime under full sunlight. The IREDs have to typically overcome ambient noise from the sun. Polaroid sunglasses can also sometimes prevent function if the coating prevents the wavelength to pass through.

The last challenge worth mentioning is that of consumer acceptance and loss of privacy. From a legal perspective, if the camera is recording the driver's face – the information can be pulled up in court if needed by a lawyer. NHTSA regulations mandate that any information needed for vehicle safety has to be stored for a short duration – essentially a black box (As used in aircrafts) to help reconstruct an accident. Will consumers trade a loss of privacy for safety and convenience (of automated driving) is yet to be seen. OEM's may initially provide consumers with the option to turn off the camera (and related loss of function) to enable the transition.

4.5. Additional applications for interior camera

OEMs are evaluating the concept of using interior cameras to monitor all occupants in the car – to enable optimum deployment of airbags and other passive safety devices. At a basic level, if there is no occupant in the passenger seat (or just a cargo box) – do not deploy the airbag.

Another application is the use of gesture recognition. The idea is use gesture's seamlessly and conveniently to open windows/sunroofs/turn on radio/change albums/etc. The successful combination of voice, touch and gesture to operate devices depend a lot on the age group (and resultant car design) and how well the technologies are implemented.

Face recognition and iris recognition are already making their way into smartphones. They are expected to penetrate the auto market. Even though the technologies are available and mature, the business case/consumer demand/willingness to pay for these functions is yet to be explored.

4.6. Signal processing

As cameras become ubiquitous around the car, the questions become how many cameras are enough and what should be the range and resolution of the cameras. The same question can be asked of LIDAR and RADAR also. However, signal processing tends to be more demanding the high resolution (comparatively) of cameras.

Assuming a VGA format for the image sensor, we get 480 (H) × 640 (W) pixels per frame; with typically 30 fps coming in for processing. The resolution we get from this VGA image sensor depends on the optical field of view it covers and the maximum range at which the smallest object has to be recognized and resolved for action. At 100 m and a 40° HFOV the width covered by the 640 pixels is ~7279 cm. This means each pixel covers 11.4 cm or ~4.5 in. Is this level of resolution good enough for self-driving cars? The next section digs a little deeper into this topic.

4.7. Exterior camera resolution requirement

What is the smallest object that can change the trajectory of the car? One could argue this could be as small as a nail or sharp object on the road. Maybe with the newer tires which can roll over nails, we can overlook this object (They would then become mandatory for self-driving cars). The next object I can think of would be a solid brick placed on the road which even though small, could change the trajectory of the car. Other such objects like tires, tin cans, potholes, etc. could be imagined that would have a similar impact.

The autonomous car machine vision has to detect such an object at a far enough distance to take appropriate measures (steer, brake/slow down or prepare for collision). With a speed of 100 mph and a dry road with friction of 0.7, a braking/sensing range of 190 m is calculated [13]. A modular USA brick with dimensions of 194 × 92 × 57 mm would subtend an angle of ~2 arc min ($\tan^{-1} 65/100,000$). This level of resolution would be outside the capability of a standard VGA camera.

After detection, the object has to be classified before an action can be taken on how to deal with it. The kinds of objects the car could come across on its path depends very much geofenced location. Objects on the US road freeways and urban streets could be very different from those in India or china. This is the point where the admiration for the human senses and brain capacity start daunting current computer chips.

5. Sensor fusion

5.1. Need for sensor fusion

For self-driving cars to be accepted by society, they would have to demonstrate significantly lower probability of collision – when compared to human drivers. A 2016 study by Virginia Tech Transportation Institute [14] found that self-driving cars would be a comparable or a little better than humans for severe crashes, but significantly better at avoiding low severity level crashes (level 3). The level 3 crash rate was calculated at 14.4 crashes per million miles driven for humans and 5.6 crashes for self-driving cars.

To keep things in perspective, we could estimate an average person in USA to drive 900,000 miles in their lifetime (12,000 miles/year × 75 years). Also note that the above report uses only Google












Object_list	RADAR	Camera	LIDAR	Sensor Fusion
Car@150m		Don't See it (Noise)		
Not_Classified@100 m & low light				Evaluate TTC & brake if unresolved ?
@50m				Person on bicycle
Not classified	Don't see it (Noise)			Brake or ignore ?
Potholes & stuff				What can be safely ignored ?

Figure 7. The challenge of sensor fusion – illustrated.

self-driving car data. These cars are known to have a full suite of sensors (Multiple LIDAR, RADAR, Cameras, Ultrasonic, GPS and other sensors).

The point is that just like the human driver, the car has to integrate the information from multiple sensors and make the best decision possible in the circumstance. On top of that, it has to be way better to get people to start adopting the technology. Knowing that each of the sensor technologies has some limitation, the need to fuse multiple inputs reliably is a daunting task. Incorrect or poor implementation of the sensor fusion could quickly take the car back to the dealer show room.

5.2. Challenges to sensor fusion

Figure 7 below illustrates the challenge of sensor fusion.

The objective sensor fusion is to determine the environment around the vehicle trajectory with enough resolution, confidence and latency to navigate the vehicle safely.

Figure 7 row 1 shows the ideal case when two sensors agree on an object and the object is detected early enough to navigate the car.

Figure 7 row 2 shows a case where each of the sensors classifies the object differently. In this case, the best option maybe to just agree that it is big enough object to avoid if possible.

Figure 7 row 3 similar situation where a person on a bicycle maybe identified as a person or a bicycle. Again, we could agree that it is an unidentified large moving object that needs to be avoided.

The last two rows shows smaller objects that pose difficult questions. Is it better to run over a small dog than to risk braking and getting rear-ended? Can the pothole be detected and classified early enough to navigate? Is the pothole or object small enough to run over?

These questions will take a longer time to resolve with improving technology in sensing, computing, public acceptance and legislation. The 80/20 Pareto principle would imply that the last 20% of the problems for self-driving cars will take 80% of the time it takes to bring it to mass market.

6. Conclusions

The exponential growth of electronics in the auto industry can be estimated by the number of sensors and electronic control units (ECUs) being added to each newer cars. From a 2003 VW golf (~35 ECUs, 30 sensors); a 2013 Ford Fusion (~70 ECUs, 75 Sensors) to a projection for automated car in 2030 (~120 ECUs, >100 Sensors) [1]. One could be forgiven for imagining the future car to be a supercomputer with wheels.

We are in the initial growth spurt for autonomous cars. A lot of technology still remains to be innovated and matured before regulation and standards kick-in. LIDAR technology is still evolving – range, resolution, eye safety, form factor and cost of the technology is improving rapidly. Camera hardware for medium range and VGA resolution has matured – but needs improvement in range (200 m target), resolution (>8 Megapixel) and performance under poor lighting or with infrared. Sensor fusion architectures can only be optimized after sensors needed are standardized or at least well understood. Real time operation with use of Artificial Intelligence – Neural networks is still in early stage. Society has still to debate and accept the safety performance with known behavior of these robots on wheels. What a great time for electronics and the Auto industry!

Author details

Rajeev Thakur

Address all correspondence to: rajeev.thakur@osram-os.com

OSRAM Opto Semiconductors, Inc., Novi, United States of America

References

- [1] Carlson J. Evolution of ADAS architectures, sensor fusion, and the future of the autonomous car. In: ADAS Sensors Conference (2017); 17-18 May 2017; Detroit, Michigan
- [2] Federal Automated Vehicles Policy; Sept 2016; U.S Department of Transportation; www.nhtsa.gov; Docket No. NHTSA-2016-0090; page 5
- [3] Surface vehicle recommended practice; Taxonomy and Definitions of terms related to driving automation systems for on-road motor vehicles; SAE J3016_201609; Table 1, page 17

- [4] Philip Ronan, Gringer. Revised diagram with re-aligned spectrum; File – EM spectrum.svg and Linear visible spectrum.svg; 19 February 2013;13:51:42. Available from: https://en.wikipedia.org/wiki/Electromagnetic_radiation [Accessed: 2017-07-17]
- [5] Rfcafe. Solar Spectral Irradiance & PV Cell Operational Regions (ASTM G173-03) [Internet]. 2017. Available from: <http://www.rfcafe.com/references/electrical/ASTM-G173-03-Reference-Spectra.htm> [Accessed: 2017-07-18]
- [6] Vehicle-to-Vehicle Communications: readiness of V2V technology for application – DOT HS 812014; Table V-7; page 105
- [7] Millimetre Wave Receiver concepts for 77 GHz automotive radar in silicon Germanium Technology – D.Kissenger (Springer Brief's 2012); Table 2.1 and 2.2; Page 18
- [8] Wikipedia. Sunlight [Internet]. 2001; By Nick84 - http://commons.wikimedia.org/wiki/File:Solar_spectrum_ita.svg, CC BY-SA 3.0, [Accessed: 2017-09-05]
- [9] Thakur R. ADAS to autonomous – Evolution of LIDAR and infrared camera. In: ADAS Sensors Conference (2017); 17-18 May 2017; Detroit, Michigan
- [10] Weber R. Infrared LED Illumination for Sensor Applications [OSRAM Opto Semiconductors Inc - Webinar]; 3 Dec 2015; Detroit, Michigan
- [11] National Center for Statistics and Analysis. Distracted Driving 2014 (Traffic Safety Facts Research Note. Report No. DOT HS 812 260). Washington, DC: National Highway Traffic Safety Administration; 2016, April
- [12] Department of Transportation, National Highway Traffic Safety Administration Docket No. NHTSA-2010-0053. Visual-Manual NHTSA Driver Distraction Guidelines for In-Vehicle Electronic Devices
- [13] Thakur R. Infrared sensors for ADAS and beyond – LIDAR/infrared camera. In: TU-Automotive Conference (2015); 4 October 2015; Novi, Michigan
- [14] Blanco M, et al; Automated Vehicle Crash Rate Comparison Using Naturalistic Data (2016); Jan 2016; Virginia Tech Transportation Institute; figure 1; page iv

We are IntechOpen, the world's leading publisher of Open Access books Built by scientists, for scientists

6,300

Open access books available

171,000

International authors and editors

190M

Downloads

Our authors are among the

154

Countries delivered to

TOP 1%

most cited scientists

12.2%

Contributors from top 500 universities



WEB OF SCIENCE™

Selection of our books indexed in the Book Citation Index
in Web of Science™ Core Collection (BKCI)

Interested in publishing with us?
Contact book.department@intechopen.com

Numbers displayed above are based on latest data collected.
For more information visit www.intechopen.com



Experimental and Numerical Study of an Optoelectronics Flexible Logic Gate Using a Chaotic Doped Fiber Laser

Juan Hugo García-López, Rider Jaimes-Reátegui, Samuel Mardoqueo Afanador-Delgado, Ricardo Sevilla-Escoboza, Guillermo Huerta-Cuéllar, Didier López-Mancilla, Roger Chiu-Zarate, Carlos Eduardo Castañeda-Hernández and Alexander Nikolaevich Pisarchik

Additional information is available at the end of the chapter

<http://dx.doi.org/10.5772/intechopen.75466>

Abstract

In this chapter, we present the experimental and numerical study of an optoelectronics flexible logic gate using a chaotic erbium-doped fiber laser. The implementation consists of three elements: a chaotic erbium-doped fiber laser, a threshold controller, and the logic gate output. The output signal of the fiber laser is sent to the logic gate input as the threshold controller. Then, the threshold controller output signal is sent to the input of the logic gate and fed back to the fiber laser to control its dynamics. The logic gate output consists of a difference amplifier, which compares the signals sent by the threshold controller and the fiber laser, resulting in the logic output, which depends on an accessible parameter of the threshold controller. The dynamic logic gate using the fiber laser exhibits high ability in changing the logic gate type by modifying the threshold control parameter.

Keywords: optical logic devices, optoelectronics, fiber laser, chaos

1. Introduction

An important advantage of erbium-doped fiber lasers (EDFLs) over other optical devices is a long interaction length of the pumping light with active ions that leads to a high gain and a

single transversal-mode operation for a suitable choice of fiber parameters. The EDFL with coherent radiation at the wavelength of 1560 nm is an excellent device for applications in medicine, remote sensing, reflectometry, and all-optical fiber communications networks [1, 2]. Rare-doped fiber lasers subjected to external modulation from semiconductor pump lasers are known to exhibit chaotic dynamics [3–12]. Besides, a very important advantage of the EDFL working in a chaotic regimen is its application to the development of basic logic gates [13], since it can process different logical gates and implements diverse arithmetic operations. The simplicity in switching chaotic EDFL between different logical operations makes this device more suitable for general purposes than traditional computer architecture with fixed wire hardware.

Using a chaotic system as a computing device was proposed by Sinha and Ditto [14], who applied for this purpose a chaotic Chua's circuit with a simple threshold mechanism. After this pioneering work, chaotic computational elements received considerable attention from many researchers who developed new designs allowing higher capacity for universal general computing purposes enable to reproduce basic logic operations, such as AND, OR, NOT, XOR, NAND, and NOR [15–26]. Likewise, a single chaotic element has the ability in reconfiguring into different logic gates through a threshold-based control [15, 16]. This device is also known as reconfigurable chaotic logic gate (RCLGs) and, due to its inherent nonlinear components, has advantages over standard programmable gate array elements [19] where reconfiguration is obtained by interchanging between multiple single-purpose gates. Also, discrete circuits working as RCLGs were proposed to reconfigure all logic gates [17, 18]. Additionally, reconfigurable chaotic logic gates arrays (RCGA), which morph between higher-order functions, such as those found in a typical arithmetic logic unit (ALU), were invented [20]. Recently, some of the authors of this work proposed an optoelectronics flexible logic gate based on a fiber laser [27, 28].

Here, we describe in detail the implementation of the optoelectronics flexible logic gate based on EDFL, which exploits the richness and complexity inherent to chaotic dynamics. Using a threshold controller, NOR and NAND logic operations are realized in the chaotic EDFL.

This chapter is an extension of the article "*Optoelectronic flexible logic gate based on a fiber laser. Eur. Phys. J. Special Topics. 2014*" [27]. It is organized as follows. The theoretical model of the diode-pumped EDFL is described in Section 2. The experimental setup of the optical logic gate based on the EDFL is given in Section 3. Likewise, the discussion of theoretical and experimental results on the application of the NAND and NOR logic gates based on the EDFL as a function of the threshold controller is presented in Section 4. Finally, main conclusions are given in Section 5.

2. Theoretical arrangement

The EDFL is known to be extremely sensitive to external disturbances, which can destabilize its normal operation. This makes this device very promising for many applications where small-amplitude external modulation is required to control the laser dynamics. The mathematical

model and experimental arrangement of the EDFL used in this work have been developed by Pisarchik et al. [6–12].

2.1. EDFL theoretical model

Based on the power balance approach, we model diode-pumped EDFL dynamics by considering both the excited-state absorption (ESA) in erbium at the 1560-nm wavelength and the averaged population inversion along the pumped active fiber laser. The model addresses two evident factors, the ESA at the laser wavelength and the depleting of the pump wave at propagation along the active fiber, leading to undamped oscillations experimentally observed in the EDFL without external modulation [6, 12]. The energy-level diagram of the theoretical model used in this work is shown in **Figure 1**.

Using a conventional system for EDFL balance Equations [6, 7], which describe the variations of the intra-cavity laser power P (in units of s^{-1}), that is, the sum of the contrapropagating waves' powers inside the cavity and the averaged population N (dimensionless variable) in the upper laser level "2," we can write EDFL equations as follows:

$$\frac{dP}{dt} = \frac{2L}{T_r} P [r_\omega \alpha_0 (N[\xi - \eta] - 1) - \alpha_{th}] + P_{sp} \quad (1)$$

$$\frac{dN}{dt} = -\frac{\sigma_{12} r_\omega P}{\pi r_0^2} (\xi N - 1) - \frac{N}{\tau} + P_{pump} \quad (2)$$

where N can take values between $0 \leq N \leq 1$ and is defined as $N = \frac{1}{n_0} L \int_0^L N_2(z) dz$, with N_2 as the upper laser-level population density "2," n_0 is the refractive index of an erbium-doped fiber, and L is the length of the active fiber medium; σ_{12} is the cross section of the absorption transition from the state "1" to the upper state "2," σ_{21} is the stimulated cross section of the transition in return from the upper state "2" to the ground state "1," in

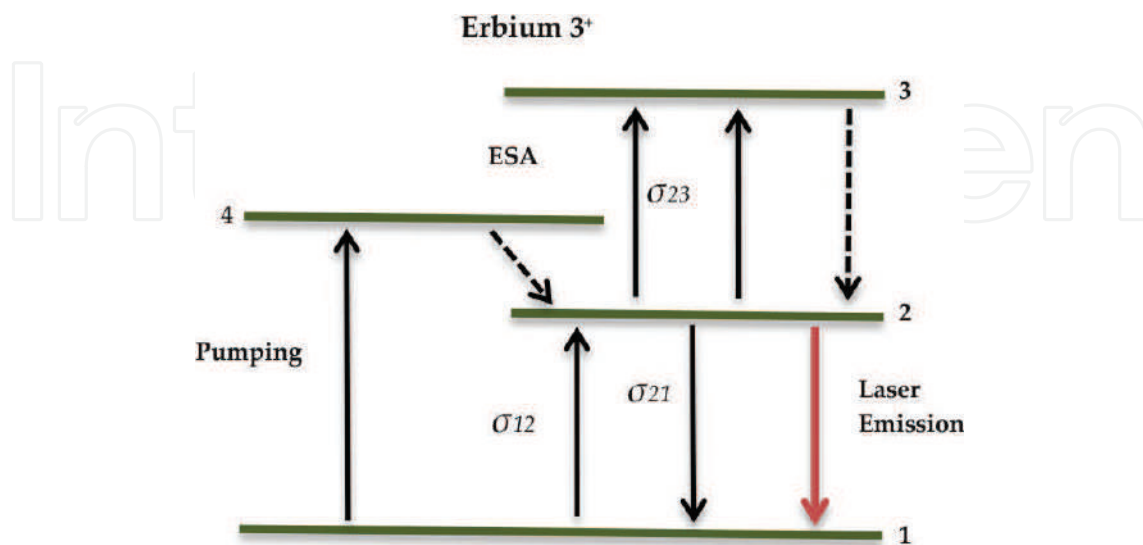


Figure 1. Erbium-doped fiber laser energy diagram.

magnitude practically are the same, that is, $\sigma_{21} = \sigma_{12}$, that gives $\xi = \frac{\sigma_{12} + \sigma_{21}}{\sigma_{12}} = 2$; $\eta = \frac{\sigma_{23}}{\sigma_{12}}$ is the coefficient ratio between excited-state absorption (σ_{23}) and the ground-state absorption cross sections (σ_{12}); $\tau_r = \frac{2n_0(L+l_0)}{c}$ is the photon round-trip time in the cavity (l_0 is the length intra-cavity tails of FBG couplers); $\alpha_0 = N_0\sigma_{12}$ is the small-signal absorption of the erbium fiber at the laser wavelength ($N_0 = N_1 + N_2$ is the total erbium ions' populations density in the active fiber medium); $\alpha_{th} = \gamma_0 + \frac{\ln(1/R_B)}{2L}$ is the cavity losses at threshold (γ_0 being the passive fiber losses, R_B is the total reflection coefficient of the fiber Bragg grating (FBG) couplers); τ is the lifetime of erbium ions in the excited state "2"; r_ω is the factor addressing a match between the laser fundamental mode and erbium doped core volumes inside the active fiber, given as

$$r_\omega = 1 - \exp\left[-2\left(r_0/w_0\right)^2\right], \quad (3)$$

where r_0 is the fiber core radius and w_0 is the radius fundamental fiber mode. The spontaneous emission P_{sp} into the fundamental laser mode is taken as

$$P_{sp} = \frac{y10^{-3}}{\tau T_\tau} \left(\frac{\lambda_g}{\omega_0}\right)^2 \frac{r_0^2 \alpha_0 L}{4\pi^2 \sigma_{12}}. \quad (4)$$

Here, we assume that the erbium luminescence spectral bandwidth (λ_g being the laser wavelength) is 10^{-3} . P_{pump} is the laser pump power given as

$$P_{pump} = P_p \frac{1 - \exp[-\beta\alpha_0 L(1 - N)]}{n_0 \pi r_0^2 L}, \quad (5)$$

where P_p is the pump power at the fiber entrance and $\beta = \frac{\alpha_p}{\alpha_0}$ is the dimensionless coefficient that accounts for the ratio of absorption coefficients of the erbium fiber at pump wavelength λ_p to that at laser wavelength λ_g . Eqs. (1) and (2) describe the laser dynamics without external modulation. We add the modulation to the pump parameter as:

$$P_{pump} = P_p^0 [1 + A_m \sin(2\pi F_m t)], \quad (6)$$

where P_p^0 is the laser pump power without modulation, A_m and F_m are the modulation amplitude and frequency, respectively.

We perform numerical simulations for the laser parameters corresponding to the following experimental conditions from references [6, 7]: $L = 90$ cm, $n_0 = 1.45$ and $l_0 = 20$ cm, giving $T_r = 8.7$ ns, $r_0 = 1.5 \times 10^{-4}$ cm, and $w_0 = 3.5 \times 10^{-4}$ cm. The value of w_0 is measured experimentally and using Eq. (3) resulting in $r_\omega = 0.308$. The coefficients characterizing the resonant-absorption properties of the erbium fiber at the laser and pump wavelengths are $\alpha_0 = 0.4$ cm⁻¹ and $\beta = 0.5$ (corresponding to direct measurements for doped fiber with erbium concentration of 2300 ppm); $\sigma_{12} = \sigma_{21} = 3 \times 10^{-21}$ cm² and $\sigma_{23} = 0.6 \times 10^{-21}$ cm² giving $\xi = 2$ and $\eta = 0.2$; $\tau = 10^{-2}$ s [6, 7]; $\gamma_0 = 0.038$ and $R_B = 0.8$ with a cavity losses at threshold of

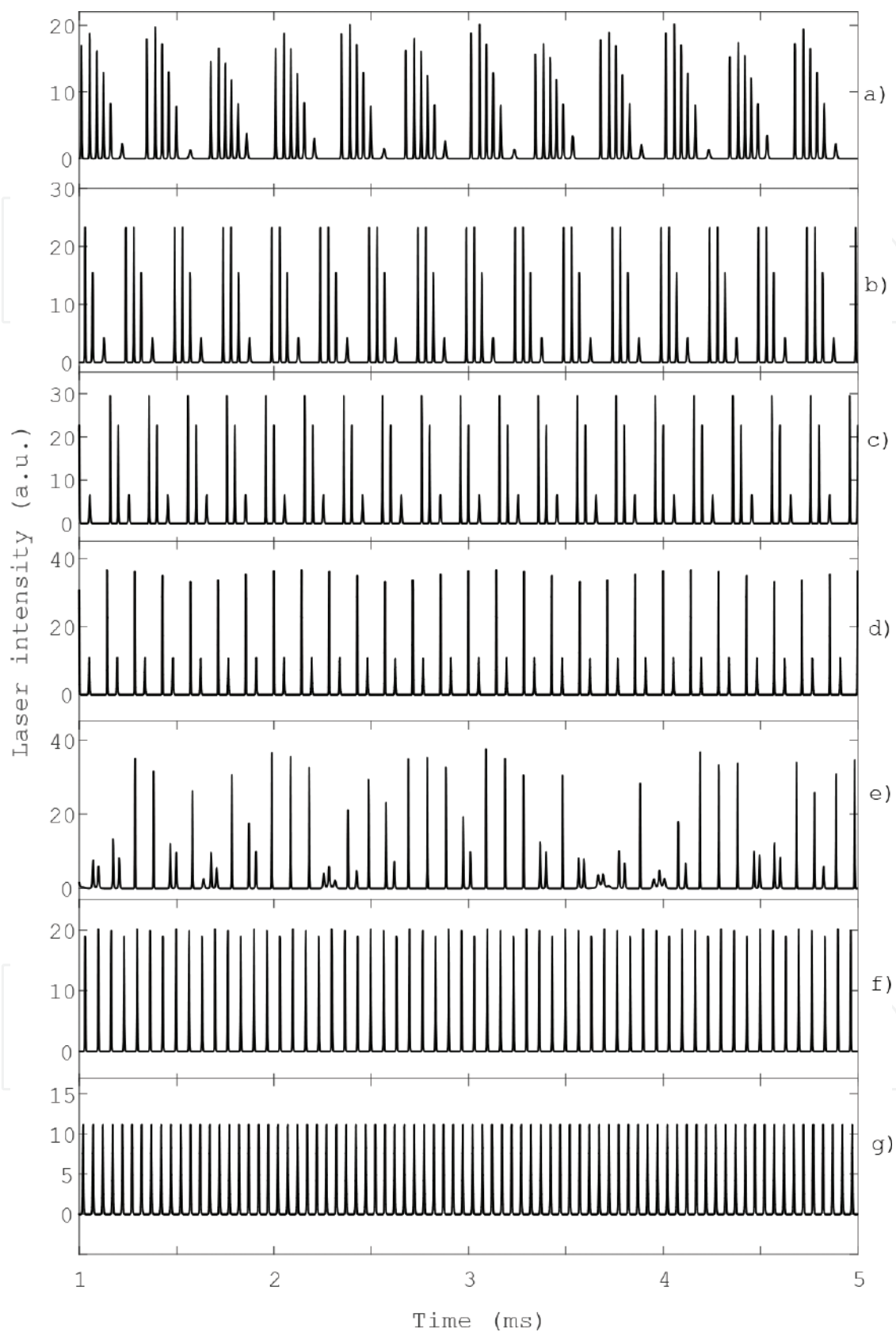


Figure 2. Time series of laser intensity P , with $A_m = 1$, and (a) $F_m = 3$ kHz, (b) $F_m = 4$ kHz, (c) $F_m = 3$ kHz, (d) $F_m = 7$ kHz, (e) $F_m = 10$ kHz, (f) $F_m = 15$ kHz, and (g) $F_m = 20$ kHz.

$\alpha_{th} = 3.92 \times 10^{-2}$. The laser wavelength is $\lambda_g = 1.56 \times 10^{-4}$ cm (photon energy $h\nu_g = 1.274 \times 10^{-19}$ J) corresponding to the maximum reflection coefficients of both FBG's.

The laser threshold is defined as $\varepsilon = P_p/P_{th}$, where

$$P_{th} = \frac{N_{th}}{\tau} \frac{n_0 \pi r \omega_p^2 L}{1 - \exp[-\beta \alpha_0 L (1 - y_{th})]} \quad (7)$$

is the threshold pump power, $N_{th} = \frac{1}{\xi} \left(1 + \frac{\alpha_{th}}{r_\omega \alpha_0}\right)$ is threshold population of the level "2" and the radius of the pump beam $w_p = w_0$. In the numerical simulations, we choose the pump power $P_p = 7.4 \times 10^{19} \text{ s}^{-1}$ that yields the laser relaxation oscillation frequency $f_0 \approx 30$ kHz.

In order to understand the dynamics of the EDFL, the bifurcation diagram of the local maxima of the laser power versus the pump modulation frequency F_m is calculated. To perform numerical simulations, we normalize Eqs. (1) and (2) (as described in the appendix of reference [29]) and obtain the following equations:

$$\frac{dx}{dt} = axy - bx + c(y + r_\omega), \quad (8)$$

$$\frac{dy}{dt} = -dxy - (y + r_\omega) + e \left\{ 1 - \exp \left[-\beta \alpha_0 L \left(1 - \frac{N_2 + r_\omega}{\xi_2 r_\omega} \right) \right] \right\}, \quad (9)$$

Figure 2 presents the time series of the laser intensity at the following driven frequencies: (a) $F_m = 3$ kHz, the laser behavior is chaotic, (b) $F_m = 4$ kHz, the EDFL response is a period 4, (c) $F_m = 3$ kHz, the EDFL response is a period 3, (d) $F_m = 7$ kHz, the EDFL response is a period 2, (e) $F_m = 10$ KHz, chaos, (f) $F_m = 15$ kHz and (g) $F_m = 20$ kHz, a period 1 with decreasing amplitude as the modulation frequency is increased.

The constant parameters of Eqs. (8) and (9) are shown in **Table 1** [30].

Figure 3 shows the numerical bifurcation diagram of the laser peak intensity versus the modulation frequency (0–20 kHz) for the 100% modulation depth ($A_m = 1$). The laser dynamical behavior (periodic or chaotic) is determined by the modulation frequency.

In this work, we are interested in a chaotic regime. **Figure 4** shows the times series corresponding to chaos for $F_m = 10$ kHz.

Constant parameter	Values (a.u.)
a	6.6207×10^7
b	7.4151×10^6
c	0.0163
d	4.0763×10^3
e	506

Table 1. Normalized constant parameters of Eqs. (8) and (9).

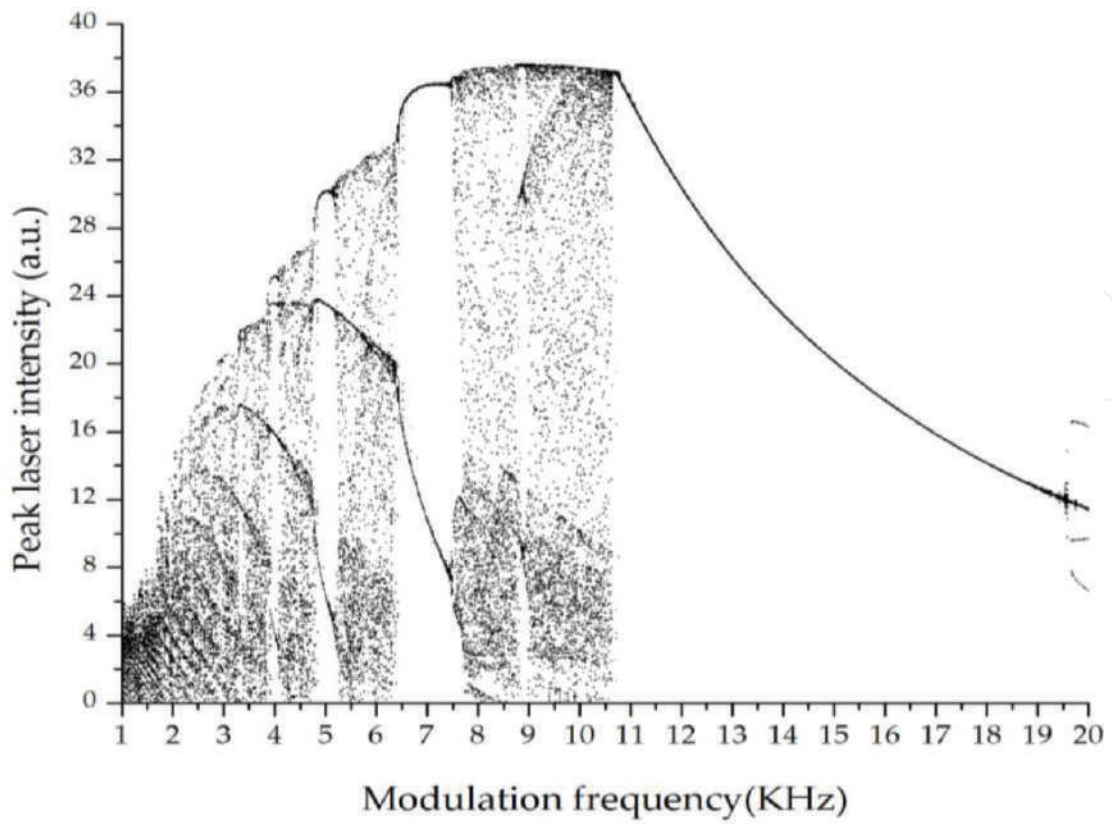


Figure 3. Numerical bifurcation diagram of laser peak intensity versus modulation frequency (F_m) for $A_m = 1$.

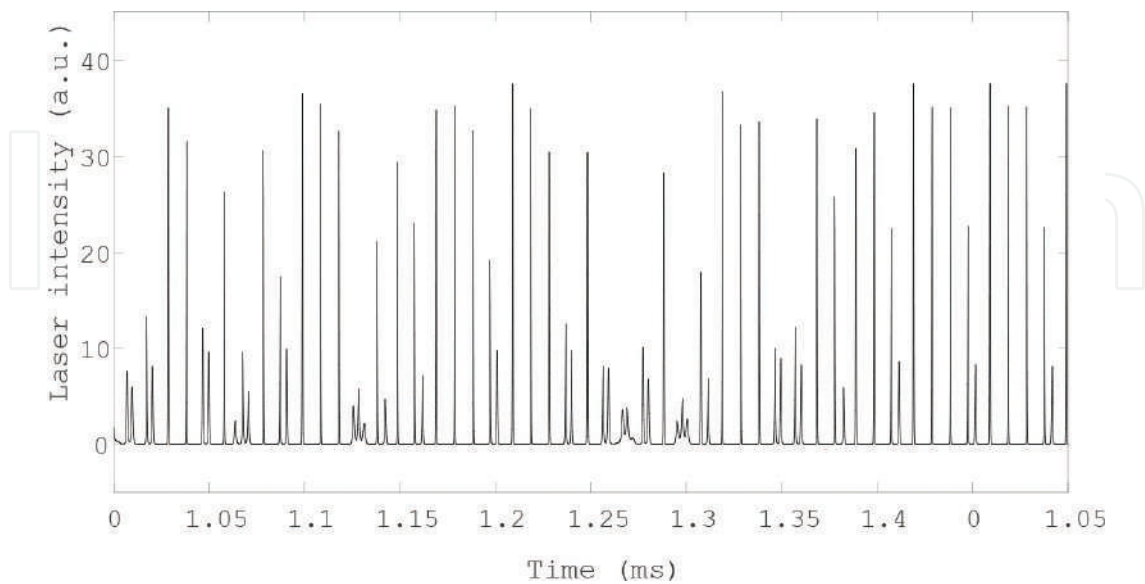


Figure 4. Time series of laser intensity P for $F_m = 10$ kHz and $A_m = 1$.

3. Implementation of the optoelectronics flexible logic gate using the EDFL

Figure 5 shows the scheme of the proposed optoelectronics flexible logic gate using the EDFL. The reconfigurable logical gate contains two principal elements: a chaotic EDFL and a threshold controller. The dynamics behavior of the EDFL is described by the balance Eqs. (1) and (2). The threshold controller compares laser power P with value V_T generated by the controller that releases output $V_T = E$ if $P > E$ and $V_T = P$ otherwise, with E as threshold value. This output signal V_T is added to the diode pump current P_{pump} with a coupling coefficient K . The logic gate output subtracts V_T from P yielding $V_0 = P - V_T$. Next, we consider the laser and the controller models separately.

3.1. Threshold controller

In our numerical simulations, we use the laser power P calculated by Eqs. (1), (2), and (6) as the input signal for the threshold controller. The output signal V_T from the controller is used to control the diode pump current as:

$$P_{pump} = P_p[1 + A_m \sin(2\pi F_m t) + KV_T] \quad (10)$$

The threshold controller has two logic inputs 0 and 1, which generate the corresponding values I_1 and I_2 , where $I_{1,2} = 0$ for input 0 and $I_{1,2} = V_{in}$ otherwise, where V_{in} is a certain value to define the threshold for E . A type of the logic gate is determined by a parameter V_c . The procedure to obtain this parameter is explained in detail in section Results and Discussions.

The controller generates an initial value E defined by the inputs I_1 and I_2 being either 0 or V_{in} and takes the value:

$$E = V_c + I_1 + I_2 \quad (11)$$

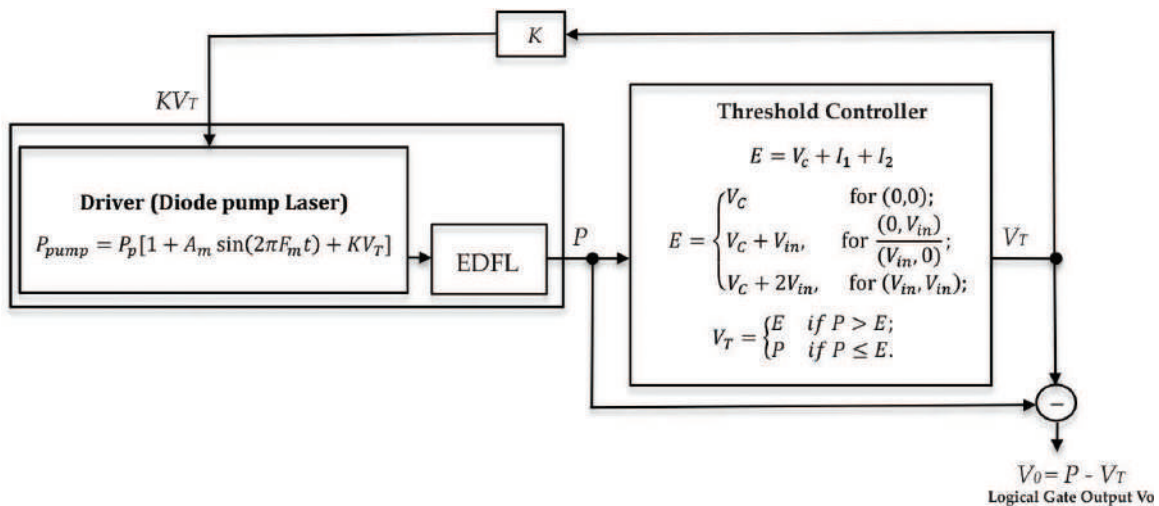


Figure 5. Arrangement of the optoelectronics logic gate. E is the threshold controller, V_c determines the logic response, $I_{1,2}$ is the logic input which takes the value of either V_{in} or 0, V_T is the output controller signal, P is the laser output intensity, P_{pump} is the diode laser pump intensity, P_p is the continuous component of the pumping, A_m and F_m are the modulation depth and frequency, and K is the gain factor.

so that there are three possible options:

$$E = \begin{cases} V_C & \text{for } (0, 0), \\ V_C + V_{in}, & \text{for } \frac{(0, V_{in})}{(V_{in}, 0)}, \\ V_C + 2V_{in}, & \text{for } (V_{in}, V_{in}). \end{cases} \quad (12)$$

The controller output is determined as:

$$V_T = \begin{cases} E & \text{if } P > E, \\ P & \text{if } P \leq E. \end{cases} \quad (13)$$

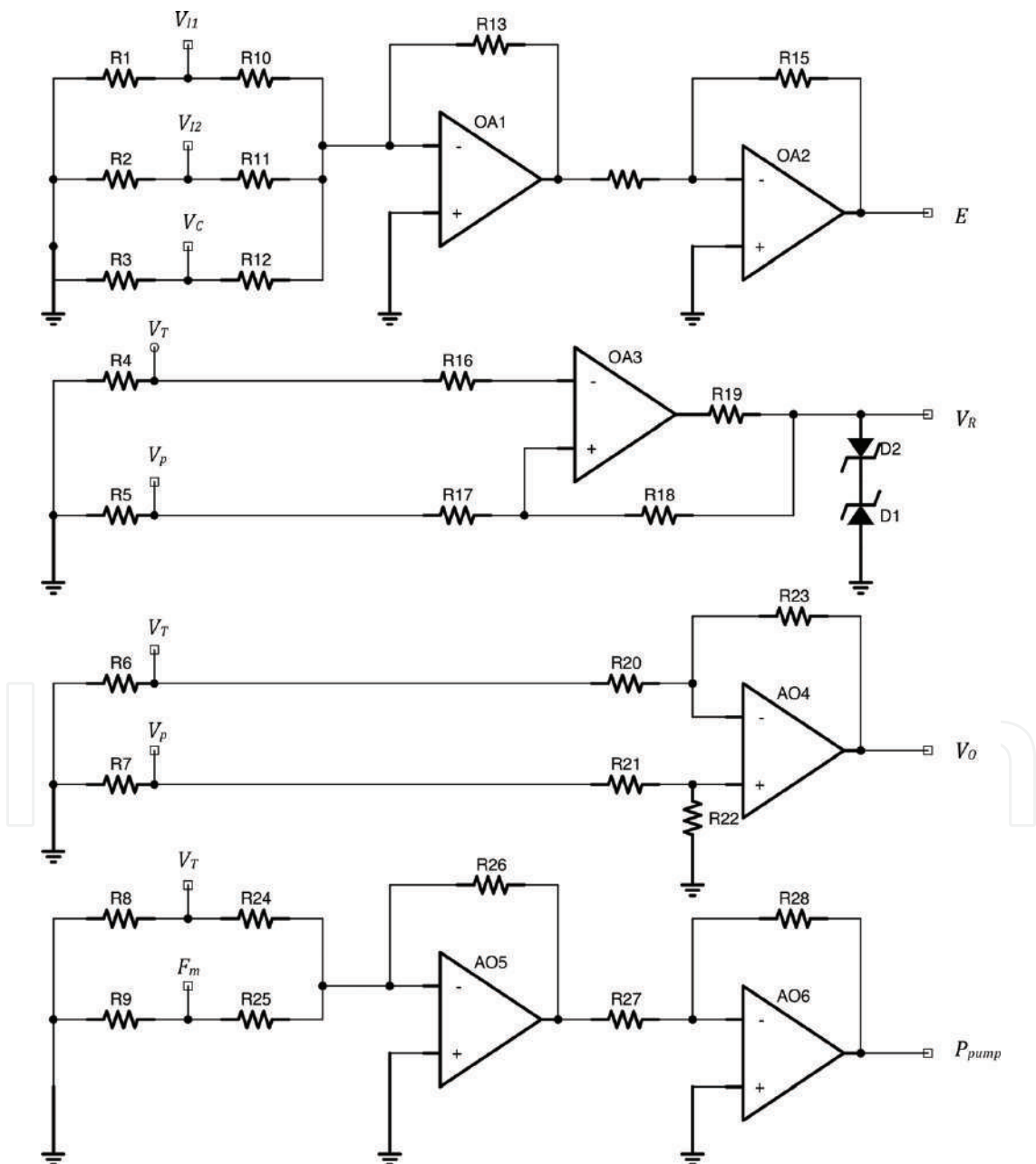


Figure 6. Electronic circuits of the threshold controller.

where V_T becomes the threshold signal.

Figure 6 shows the electronic circuits in the controller to generate E , V_R , V_0 , and P_{pump} signals. The electronic components used in the controller are presented in **Table 2**.

3.2. EDFL experimental arrangement

The experimental arrangement presented in **Figure 7** consists of EDFL pumped by a laser diode (LD) from Thorlabs PL980 operating at 1560 and 977 nm, respectively. The Fabry-Perot fiber laser cavity with total length of 4.81 m is formed by an active, long EDFL of 88-cm length, and a 2.7- μm core diameter, incorporating two fiber Bragg gratings (FBG1 and FBG2) with 0.288 and 0.544-nm full widths on half-magnitude bandwidth, having, respectively, $\sim 100\%$ and $\sim 96\%$

Electronic component	Value
R1–R9	100 Ω
R10–R15, R17, R19–R28	10 k Ω
R16	100 k Ω
R18	2.2 M Ω
C1, C2	100 μF
D1, D2	Zener diode
OA1 – OA6	LM741CN
I/O	Phoenix connector

Table 2. Parameters for electronic components of circuits shown in **Figure 6**.

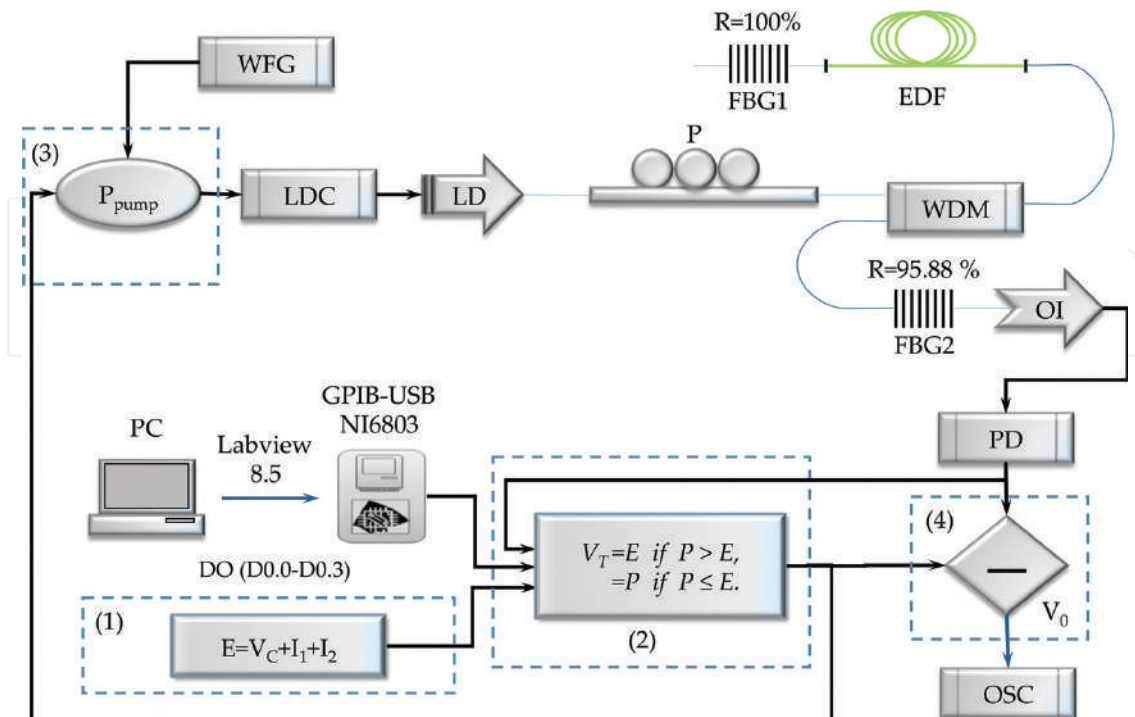


Figure 7. Experimental scheme of the optoelectronics logical gate based on EDFL.

reflectivity at the laser operating wavelength. A fiber laser formed by an erbium doped fiber (EDF) and two Bragg gratings (FBG1 and FBG2), is externally driven by the harmonic pump signal $P_{pump} = P_p[1 + A_m \sin(2\pi F_m t) + KV_T]$ (through a sum circuit CI 741) applied to a diode pump laser (LD) current via a laser diode controller (LDC) from a wave function generator (WFG). A single-mode fiber is used to connect the optical components.

The current and temperature of the LD are controlled by a laser diode controller (LDC) (Thorlabs ITC510). The 145.5-mA pump current is selected to guarantee that the laser relaxation oscillation frequency is around $F_r = 30$ kHz to provide a 20-mW power; which is above a 110-mA EDFL threshold current. A harmonic modulation signal $A_m \sin(2\pi F_m t)$ from wave function generator (WFG) (Tektronix AFG3102) is supplied to the diode pump current. The fiber laser output after passing through a polarization controller (P), wavelength division multiplexer (WDM), and an optical isolator (OI) is recorded with a photodiode (PD), and the electronic signal is compared with the signal generated by the threshold controller. The threshold controller with $E = V_c + I_1 + I_2$ is a summing circuit (CI 741) with dynamical control signal V_c and inputs logic signals $I_{1,2}$ controlled by a USB NI 6803, V_T is a comparator circuit between laser intensity P and threshold controller E . The logic gate output V_0 is sent back to the driver (P_{pump}) of the EDFL to change its dynamics. The signals P from the EDFL, $I_{1,2}$, V_T and V_0 from the threshold controller are analyzed with a multichannel oscilloscope.

4. Results and discussions

4.1. Numerical results

In order to use the arrangement of the optoelectronics logic gate shown in **Figure 5**, it is necessary to determine V_c and V_{in} signals and find the required logic gates NAND or NOR.

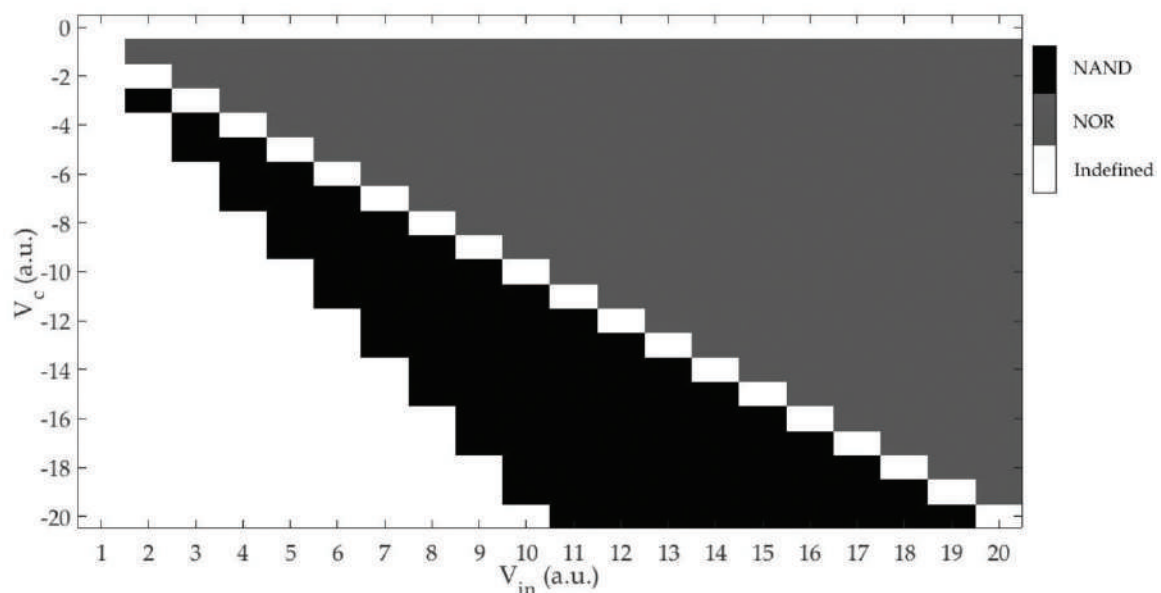


Figure 8. Diagram of values for V_c and V_{in} to determine the logic gate type, either NAND or NOR.

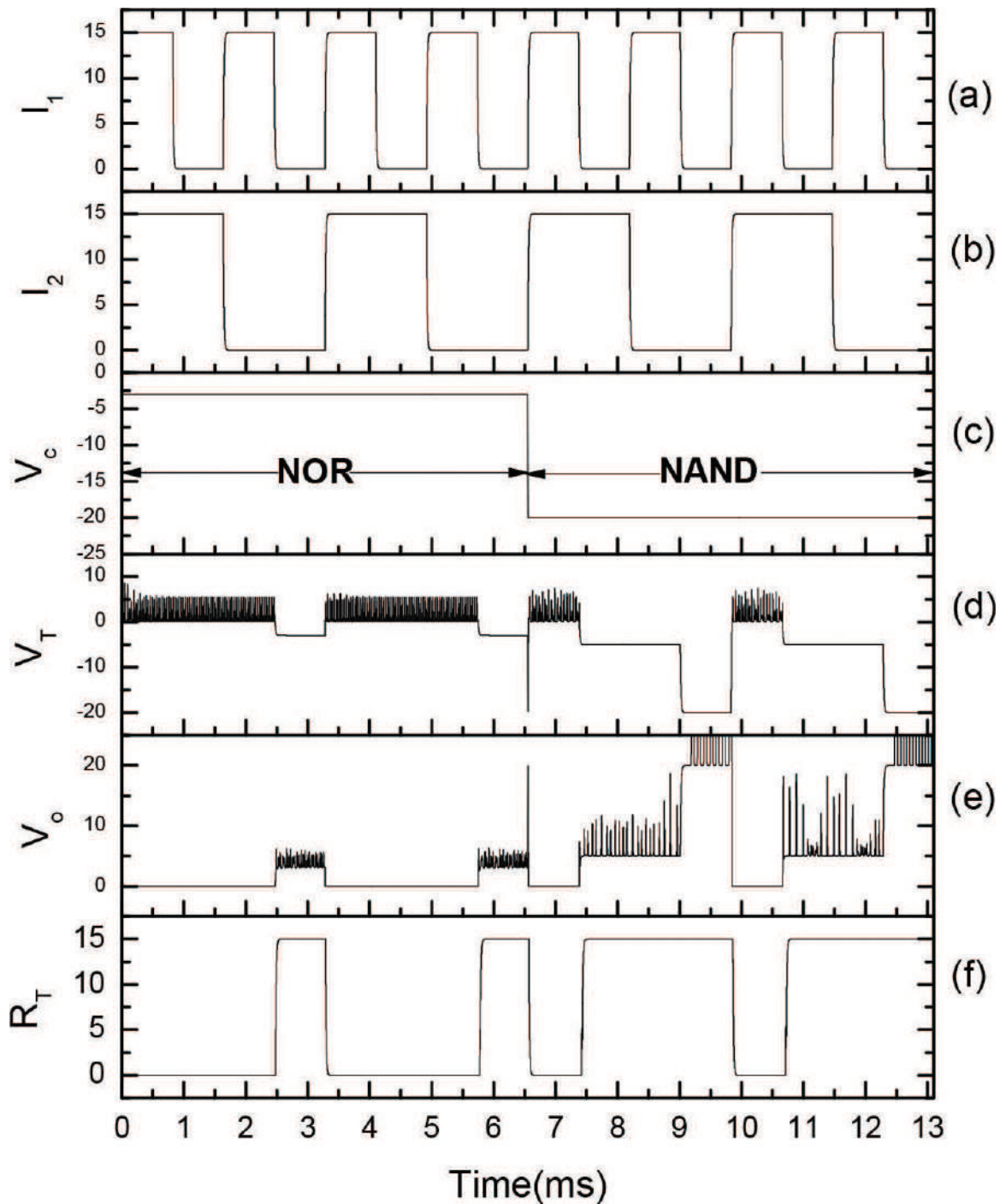


Figure 9. Numerical simulation results. (a)–(b) inputs $I_{1,2}$, (c) dynamical control signal V_c , (d) threshold controller signal V_T , (e) logic gate output V_o , and (f) recover logic output from signal V_o .

The value of V_c was gradually changed ($-20 \text{ V} < V_c < 2 \text{ V}$) and for each value of V_c the value of V_{in} was changed ($2 \text{ V} < V_{in} < 20 \text{ V}$). **Figure 8** shows the values of V_c versus V_{in} which we use to determine the logical gates NAND and NOR. If we set the parameter $V_{in} = 10 \text{ V}$ and V_c varies from -1 to -9 V , we get the NOR gate; but if V_c changes from -11 to -20 V , the NAND gate is used.

The numerical results of NOR and NAND operations of the reconfigurable dynamic logic gate Eqs. (1), (2), and (10)–(13) are shown in **Figure 9** for $A_m = 1$ V and $F_m = 10$ kHz.

For the time interval from $t = 0$ to 6.5 ms, we have a NOR logic gate, where the signal from $V_c = -3$ V to $V_{in} = 15$ V produces three different combinations of the threshold controller V_T as

1. For input $I_{1,2} = (V_{in}, V_{in})$, $E = 27$ resulting in $P \leq E$ and the threshold level $V_T = P$, that yields $V_0 = 0$.
2. For input $I_{1,2} = (0, V_{in})/(V_{in}, 0)$, $E = 12$ resulting in $P \leq E$ and the threshold level $V_T = P$, that yields $V_0 = 0$.
3. For input $I_{1,2} = (0, 0)$, $E = V_c = -3$ resulting in $P > E$ and the threshold level $V_T = E$, that yields $V_0 = P - E$.

For the time interval from $t = 6.5$ to $t = 13$ ms, **Figure 9** shows a NAND logic gate, where the signal from $V_c = -20$ V to $V_{in} = 15$ V produces three different combinations of the threshold controller V_T as

1. For input $I_{1,2} = (V_{in}, V_{in})$, $E = V_c + I_1 + I_2 = V_c + 2V_{in} = 10$ resulting in $P \leq E$ and the threshold level $V_T = P$, that yields $V_0 = 0$.
2. For input $I_{1,2} = (0, V_{in})/(V_{in}, 0)$, $E = V_c + I_1 + I_2 = V_c + V_{in} = -5$ resulting in $P > E$ and the threshold level $V_T = E$, that yields $V_0 = P - E$.
3. For input $I_{1,2} = (0, 0)$, $E = V_c = -20$ resulting in $P > E$ and the threshold level $V_T = E$, that yields $V_0 = P - E$.

4.2. Experimental results

Similar to the results of the numerical simulations, a change was made in the parameters for V_c versus V_{in} to determine required NAND or NOR logic gates. **Figure 10** shows the values of V_c

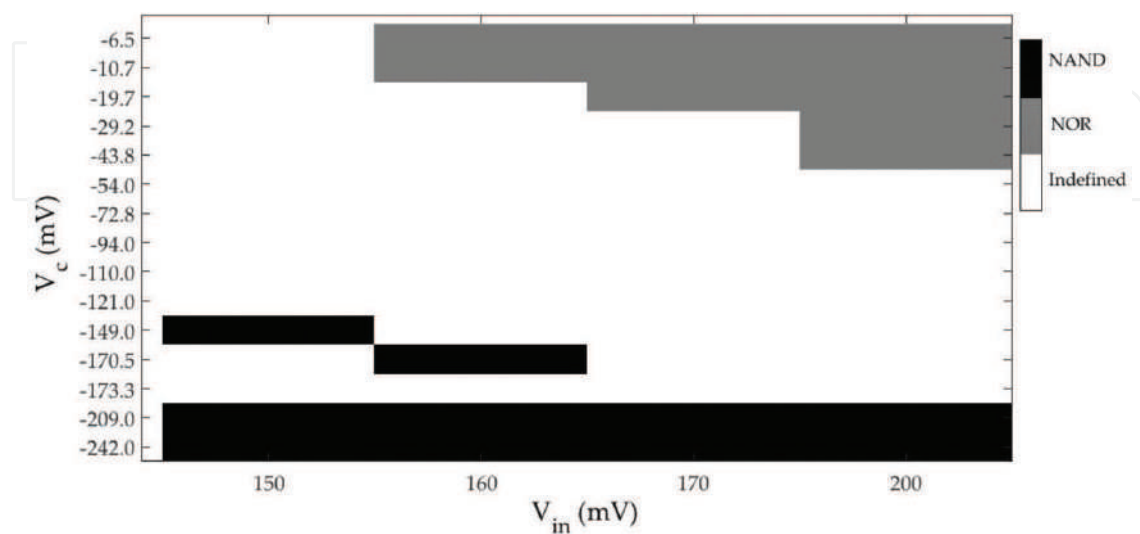


Figure 10. Diagram of values for V_c and V_{in} to determine the logic gate type, either NAND or NOR.

versus V_{in} which we use to determine the NAND and NOR logic gates. If we set the parameter $V_{in} = 160$ mV and changes $V_c = -10.7$ mV, we get the NOR gate, but if we change $V_c = -170.3$ mV, the NAND gate is used.

Figure 11 and **Table 3** show the experimental results of the dynamic NOR and NAND logic operations for $A_m = 700$ mV, $F_m = 15$ kHz, and $V_{in} = 200$ mV. The NOR gate corresponds to the time series from $t = 0$ ms to $t = 8$ ms for $V_c = -10.7$ mV, and for the NAND gate for the time series

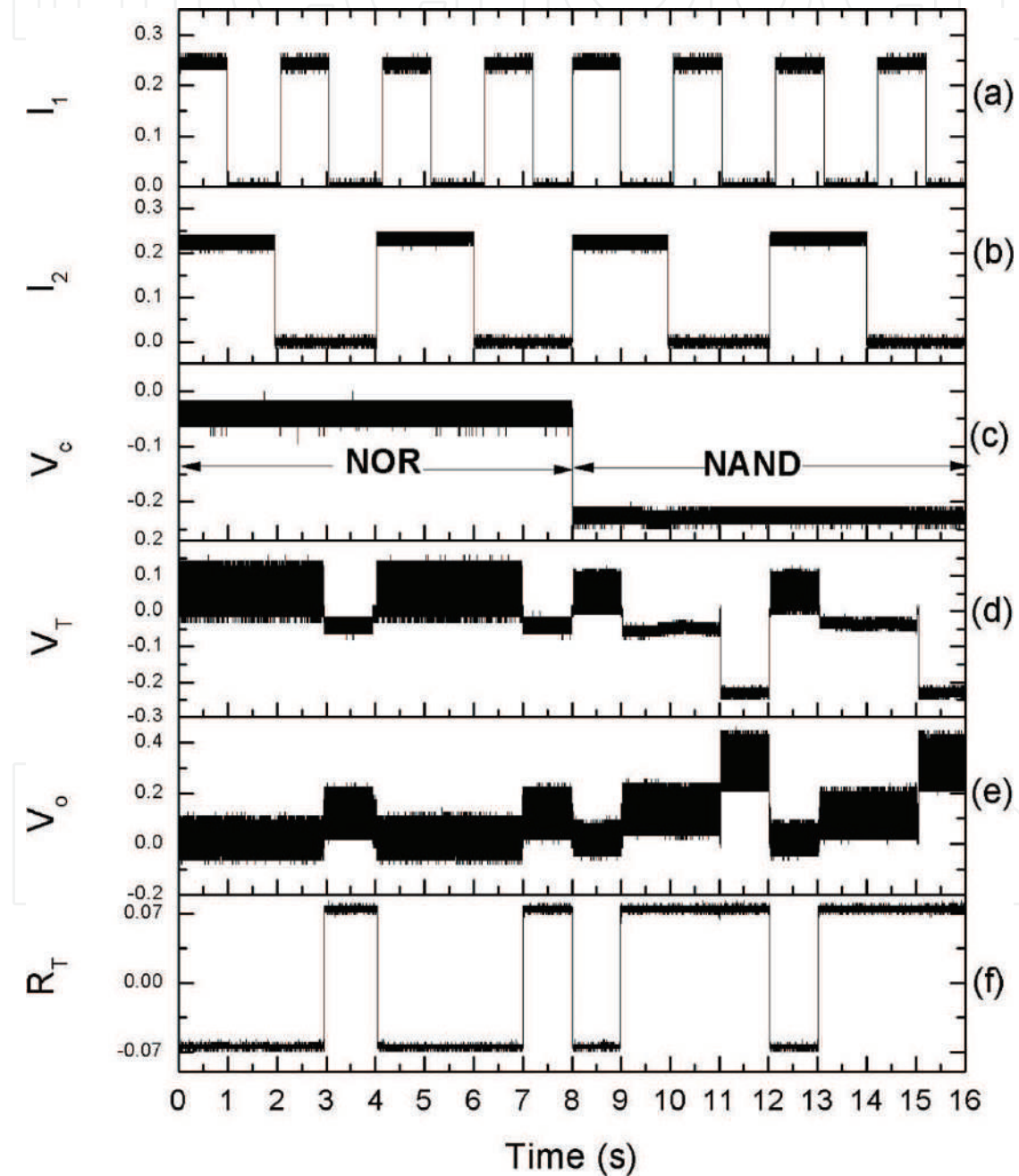


Figure 11. Experimental results. (a)–(b) inputs $I_{1,2}$, (c) dynamical control signal V_c , (d) threshold controller signal V_T , (e) logic gate output V_o , and (f) recover logic output from signal V_o .

	(I_1, I_2)	Time	Threshold controller E	V_T	V_O
	(mV)	(ms)	(mV)	(mV)	(mV)
NOR	(0, 0)	3–4	$E = V_c \sim -40$	$E \leq P$	$V_O = P - V_T = P - E$
		7–8		$V_T = E$	
	$(V_{in}, 0)$ or $(0, V_{in})$	1–3	$E = V_c + V_{in} \sim 160$	$E > P$	$V_O = P - V_T = P - P = 0$
		5–7		$V_T = P$	
	(V_{in}, V_{in})	0–1	$E = V_c + 2 * V_{in} \sim 360$	$E > P$	$V_O = P - V_T = P - P = 0$
		4–5		$V_T = P$	
NAND	(0, 0)	11–12	$E = V_c \sim -220$	$E \leq P$	$V_O = P - V_T = P - E$
		15–16		$V_T = E$	
	$(V_{in}, 0)$ or $(0, V_{in})$	9–11	$E = V_c + V_{in} \sim -20$	$E \leq P$	$V_O = P - V_T = P - E$
		13–15		$V_T = E$	
	(V_{in}, V_{in})	8–9	$E = V_c + 2 * V_{in} \sim 180$	$E > P$	$V_O = P - V_T = P - P = 0$
		12–13		$V_T = P$	

Table 3. Experimental data for implementation of NOR and NAND optoelectronics logical gates.

from $t = 8$ to $t = 16$ ms for $V_c = -220$ mV. By comparing **Figure 9** with **Figure 11**, we can see a good agreement between the numerical and experimental results.

5. Conclusions

In this chapter, we have described the implementation of an optoelectronics logic gate based on a diode-pumped EDFL. We have demonstrated good functionality of our system for NOR and NAND logic operations, taking advantage of optical chaos and a threshold controller. The system was controlled by a split signal from the threshold controller, allowing the diode pump laser to mismatch between the output threshold controller signal and the output EDFL signal. The numerical results obtained from the EDFL equations have displayed good agreement with the experimental results. We have demonstrated that the chaotic dynamic behavior of the diode-pumped EDFL and the electronic threshold controller can be successfully used to obtain NAND or NOR logic gates to be constructive bricks of different logic systems. The main contribution of the developed optoelectronics logic gate is addressed in optical computing. The proposed device is more adaptable and faster than a conventional wired hardware, since it can be implemented as an arithmetic processing unit or an optical memory RAM.

Acknowledgements

We gratefully acknowledge support and funding from the University of Guadalajara (UdeG), (R-0138/2016) under the project: Equipment of the research laboratories of the

academic groups of the CULAGOS with orientation in optoelectronics, Agreement RG/019/2016-UdeG, Mexico.

Author details

Juan Hugo García-López^{1*}, Rider Jaimes-Reátegui¹, Samuel Mardoqueo Afanador-Delgado¹, Ricardo Sevilla-Escoboza¹, Guillermo Huerta-Cuéllar¹, Didier López-Mancilla¹, Roger Chiu-Zarate¹, Carlos Eduardo Castañeda-Hernández¹ and Alexander Nikolaevich Pisarchik²

*Address all correspondence to: jhugo.garcia@academicos.udg.mx

1 Department of Exact Sciences and Technology, University of Guadalajara, Lagos de Moreno, Jalisco, Mexico

2 Center for Biomedical Technology, Technical University of Madrid, Madrid, Spain

References

- [1] Digonnet M, Snitzer E. Rare earth doped fiber lasers and amplifiers. In: Digonnet MJF, editor. Marcel Dekker, Chapter 5; 1993. ISBN-13: 978-0824704582, ISBN-10: 0824704584
- [2] Luo LG, Chu PL. Optical secure communications with chaotic erbium-doped fiber lasers. *Journal of the Optical Society of America B*. 1998;**15**:2524-2530. DOI: <https://doi.org/10.1364/JOSAB.15.002524>
- [3] Saucedo-Solorio JM, Pisarchik AN, Kiryanov AV, Aboites V. Generalized multistability in a fiber laser with modulated losses. *Journal of the Optical Society of America B*. 2003;**20**: 490-496. DOI: <https://doi.org/10.1364/JOSAB.20.000490>
- [4] Pisarchik AN, Barmenkov YuO, Kiryanov AV. Experimental characterization of the bifurcation structure in an erbium-doped fiber laser with pump modulation. *IEEE Journal Quantum Electronics*. 2003;**39**:1567-1571. DOI: 10.1109/JQE.2003.819559
- [5] Pisarchik AN, Barmenkov Yu O, Kiryanov AV. Experimental demonstration of attractor annihilation in a multistable fiber laser. *Physical Review E*. 2003;**68**. DOI: <https://doi.org/10.1103/PhysRevE.68.066211>
- [6] Reátegui RJ, Kiryanov AV, Pisarchik AN, Barmenkov Yu O, Ilichev NN. Experimental study and modelling of coexisting attractors and bifurcations in an erbium-doped fiber laser with diode-pump modulation. *Laser Physics*. 2004;**14**:1277
- [7] Pisarchik AN, Kiryanov AV, Barmenkov Yu O, Jaimes-Reategui R. Dynamics of an erbium-doped fiber laser with pump modulation: theory and experiment. *Journal of the Optical Society of America B*. 2005;**22**:2107. DOI: <https://doi.org/10.1364/JOSAB.22.002107>

- [8] Huerta-Cuellar G, Pisarchik AN, Barmenkov Yu O. Experimental characterization of hopping dynamics in a multistable fiber laser. *Physical Review E*. 2008;**78**. DOI: <https://doi.org/10.1103/PhysRevE.78.035202>
- [9] Pisarchik AN, Jaimes-Reátegui R. Control of basins of attraction in a multistable fiber laser. *Physics Letters A*. 2009;**374**:228. DOI: <https://doi.org/10.1016/j.physleta.2009.10.061>
- [10] Huerta-Cuellar G, Pisarchik AN, Kiryanov AV, Barmenkov Yu O, Del Valle Hernández J. Prebifurcation noise amplification in a fiber laser. *Physical Review E*. 2009;**79**:1. DOI: <https://doi.org/10.1103/PhysRevE.79.036204>
- [11] Pisarchik AN, Jaimes-Reátegui R, Sevilla-Escoboza R, Huerta-Cuellar G, Taki M. Rogue waves in a multistable system. *Physical Review Letters*. 2011;**107**:1. DOI: <https://doi.org/10.1103/PhysRevLett.107.274101>
- [12] Pisarchik AN, Jaimes-Reátegui R, Sevilla-Escoboza JR, Huerta-Cuellar G. Multistable intermittency and extreme pulses in a fiber laser. *Physical Review E*. 2012;**86**:1. DOI: <https://doi.org/10.1103/PhysRevE.86.056219>
- [13] Ditto WL, Murali K, Sinha S. Chaos computing: Ideas and implementations. *Philosophical Transactions of the Royal Society A*. 2008;**366**:653-664. DOI: 10.1098/rsta.2007.2116
- [14] Sinha S, Ditto W L. Dynamics based computation. *Physical Review Letters*. 1998;**81**:2156. DOI: <https://doi.org/10.1103/PhysRevLett.81.2156>
- [15] Sinha S, Munakata T, Ditto WL. Flexible parallel implementation of logic gates using chaotic elements. *Physical Review E*. 2002;**65**:1. DOI: <https://doi.org/10.1103/PhysRevE.65.036216>
- [16] Sinha S, Ditto WL. Computing with distributed chaos. *Physical Review E*. 1999;**60**:363. DOI: <https://doi.org/10.1103/PhysRevE.60.363>
- [17] Murali K, Sinha S, Ditto W L. Construction of a reconfigurable dynamic logic cell. *Pramana*. 2005;**64**:433. DOI <https://doi.org/10.1007/BF02704569>
- [18] Murali K, Sinha S, Ditto WL. Implementation of a NOR gate by a chaotic chua's circuit. *International Journal of Bifurcation and Chaos*. 2003;**13**:2669. DOI: <https://doi.org/10.1142/S0218127403008053>
- [19] Taubes G. Computer design meets Darwin. *Science*. 1997;**277**:1931. DOI: <https://doi.org/10.1126/science.277.5334.1931>
- [20] Ditto W, Sinha S, Murali K. US Patent Number 07096347. 2006
- [21] Prusha BS, Lindner J F. Nonlinearity and computation: implementing logic as a nonlinear dynamical system. *Physics Letters A*. 1999;**263**:105. DOI: [https://doi.org/10.1016/S0375-9601\(99\)00665-9](https://doi.org/10.1016/S0375-9601(99)00665-9)
- [22] Cafagna D, Grassi G. Dynamic behaviour and route to chaos in experimental boost converter. *International Symposium on Signals, Circuits and Systems*. 2005;**2**:745. DOI: 10.1109 /ISSCS.2005.1511348

- [23] Chlouverakis KE, Adams MJ. Optoelectronic realisation of NOR logic gate using chaotic two-section lasers. *Electronics Letters*. 2005;**41**:359. DOI: <http://dx.doi.org/10.1049/el:20058026>
- [24] Jahed-Motlagh MR, Kia B, Ditto WL, Sinha S. Fault tolerance and detection in chaotic computers. *International Journal of Bifurcation and Chaos*. 2007;**17**:1955-1968. DOI: <https://doi.org/10.1142/S0218127407018142>
- [25] Murali K, Miliotis A, Ditto W L, Sinha S. Logic from circuit elements that exploit nonlinearity in the presence of a noise floor. *Physics Letters A*. 2009;**373**:1346. DOI: <https://doi.org/10.1016/j.physleta.2009.02.026>
- [26] Ditto WL, Miliotis A, Murali K, Sinha S. The chaos computing paradigm. In: HeinzGeorg Schuster, editor. *Reviews of Nonlinear Dynamics and Complexity*. Vol. 3. Weinheim: WILEY-VCH Verlag GmbH & Co. KGaA; 2010. p. 1-35. ISBN: 978-3-527-40945-7
- [27] Jaimes-Reategui R, Afanador-Delgado SM, Sevilla-Escoboza R, Huerta-Cuellar G, Hugo G-LJ, Lopez-Mancilla D, Castañeda-Hernandez C, Pisarchik AN. Optoelectronic flexible logic gate based on a fiber laser. *The European Physical Journal Special Topics*. 2014;**223**: 2837-2846. DOI: [10.1140/epjst/e2014-02297-4](https://doi.org/10.1140/epjst/e2014-02297-4)
- [28] García-López JH, Jaimes-Reategui R, Afanador-Delgado SM, Sevilla-Escoboza R, Huerta-Cuellar G, Casillas-Rodríguez FJ, López-Mancilla D, Pisarchik AN. Optoelectronic flexible logic-gate using a chaotic erbium doped fiber laser, experimental results. In: *Latin America Optics and Photonics Conference*. OSA Technical Digest (online) (Optical Society of America, 2014), paper LTu4A.36. DOI: <https://doi.org/10.1364/LAOP.2014.LTu4A.36>
- [29] Jaimes-Reategui R. *Dynamic of Complex System with Parametric Modulation Duffing Oscillators and a Fiber Laser (Thesis)*. Leon, Guanajuato, Mexico: Center for Optical Research; 2004
- [30] Afanador Delgado SM. *Implementación opto-electrónica de una compuerta lógica dinámicamente configurable usando un láser de fibra (thesis)*. Lagos de Moreno, Jalisco, Mexico: CULagos, University of Guadalajara; 2014

We are IntechOpen, the world's leading publisher of Open Access books Built by scientists, for scientists

6,300

Open access books available

171,000

International authors and editors

190M

Downloads

Our authors are among the

154

Countries delivered to

TOP 1%

most cited scientists

12.2%

Contributors from top 500 universities



WEB OF SCIENCE™

Selection of our books indexed in the Book Citation Index
in Web of Science™ Core Collection (BKCI)

Interested in publishing with us?
Contact book.department@intechopen.com

Numbers displayed above are based on latest data collected.
For more information visit www.intechopen.com



Perovskite Solar Cells: The Challenging Issues for Stable Power Conversion Efficiency

Hilal Ahmad Reshi and Rayees Ahmad Zargar

Additional information is available at the end of the chapter

<http://dx.doi.org/10.5772/intechopen.75406>

Abstract

Despite the advanced processing advantages for low cost, flexible and highly efficient solar cells, the technology is still facing the challenges with regard to the stability of materials in terms of moisture, thermal, light and oxygen atmosphere. The recent discovery of lead halide perovskite has increased a surge of interest in the field of photovoltaics. The chapter highlights some ways that can improve the stability and reducing the toxicity without compromising the efficiency of perovskite. Most of the part includes the review on the actual knowledge and cutting edge research results of high efficiency perovskites. It further describes the materials (Oxides and hybrid halides) that can be used for real time solar cell applications.

Keywords: halide-perovskite, photovoltaics, solar cells

1. Introduction

The rapidly growing rate of consumption of natural resources increases the demand for clean and everlasting option capable of providing indefinite and sustainable energy. Tackling with this global energy crisis is undoubtedly one of the most substantial scientific challenges of present era. Not only this, but the levels of greenhouse gases being emitted in the atmosphere are alarming, which reveals that the existing energy trends are also problematic in terms of economic and environment point of view [1]. Utilization of renewable sources and particularly solar energy provides the most solid alternative viable long term solution to this problem. The growing awareness about the urgency and benefits of solar energy systems will automatically push the efforts towards largely decarbonized energy systems. Arguably the most abundant and renewable energy source is sunlight with over 1000 W/m² of energy

is falling at the surface of earth at sea level on clear sunny day. As a matter of fact, the solar energy that hits our planet in 1 hour is equal to the total amount of energy consumed by all humans of the world in a year. Indeed, coverage of less than 1% of the earth's surface would be sufficient to meet the world's energy needs using the latest commercially available solar panels. However, to compete the solar energy devices with fossil fuels in utility scale power generation, the necessary requirement is to reduce the total cost of solar energy either by low cost of solar device materials or by increased efficiency. Light energy conversion applications are of different types, among them photovoltaics consists of a number of established as well as emerging technologies. The solar cell is a photoelectric device which can directly convert solar energy into electric energy and offers the light absorbing capacity, long life cycle and less maintenance requirements. The first silicon based single crystal p-n junction solar cell was published in 1954 [2]. The study then increased exponentially over a half a century moving from crystalline silicon to inorganic, dye-sensitized, polymer and now perovskite solar cells. With regard to the commercialized modules, crystalline silicon devices are currently representing the 90% of global share [3]. Research and innovation over the years have led to the thriving performances of around 25% efficiency with a lifetime of 20 years in silicon based devices [4, 5]. This increased performance has forced many countries to initiate the economic programmes for producing electrical energy from renewable sources to civil and industrial sectors. During the last few years, the retail cost of silicon based photovoltaic devices/modules has reduced by ~70% which makes it possible to generate the revenues to develop this field further. Hence it makes some real image to realize innovative photovoltaic systems that can fulfill the actual demand of pollution free sustainable and stable energy. The perovskites is the most dominant of a wide family of materials with general formula ABX_3 type in which A = organic cation, B = metallic cation and X = halide anion. The A cation is found to be somewhat larger than B. **Figure 1** represents the crystal structure of $CH_3NH_3PbI_3$ perovskite a best known as a photoabsorbing material. Several properties such as ferroelectric, ferromagnetic, antiferromagnetic, piezoelectric, semiconducting, superconducting, conducting, insulating, catalysis etc. have been found in these materials since many years [6].

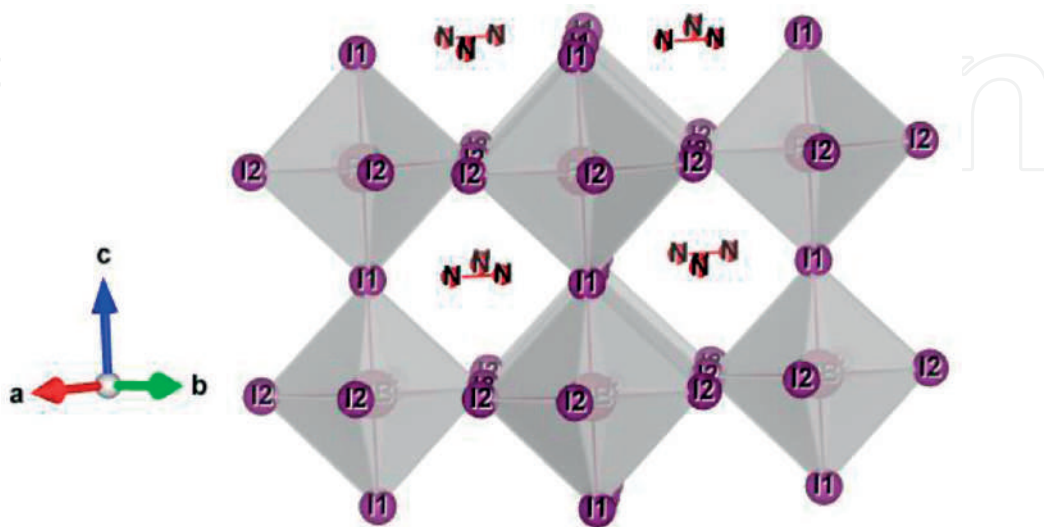


Figure 1. Typical perovskite crystal structure of $CH_3NH_3PbI_3$.

Organic solar cells have received an extensive amount of attention for renewable energy sources because of advantageous features such as low cost, flexibility, light weight and solution based fabrication [7]. However the first photovoltaic application was found in halide based perovskite $\text{CH}_3\text{NH}_3\text{Pb}(\text{I}_3, \text{Br}_3)$ by Miyasaka and his associates as an absorber material for the devices giving less than 1% power conversion efficiency for solid state cells [8]. The further optimization triggered in 2012 when the $\text{CH}_3\text{NH}_3\text{PbI}_3$ (MAPI) and its mixed halide crossed the 10% efficiency mark [9, 10]. The progress has been observed rapidly over the years and the power conversion efficiency exceeds 20% using organo-lead halide perovskite [11, 12]. The most studied perovskites in terms of multifunctional applications are oxides due to their electrical, magnetic and ferroelectric properties. Halide perovskites initially received a little attention until layered organo-metallic halide perovskites were reported to exhibit a semiconductor to metal transition with increased dimensionality [13]. In 2013, perovskite solar cell technology was declared as one of the biggest scientific breakthroughs by the editors of Science and Nature [14]. However this breakthrough observed in solution based perovskites has drawback that the high efficiency can be obtained only in lead based perovskites which is arguably a substantial hurdle for various applications due to its toxic nature, even though the amount of concentration of lead is very less. This opens a new area of research to find some alternative approach for the replacement of lead without hampering the cell efficiency, durability and stability.

For future large scale solar photovoltaic, a material is required to meet some important parameters such as the material should be earth abundant, cost effective, and non-toxic. In addition, to achieve the high power conversion efficiency, the material must meet some principle properties such as electrical, optical and some defect properties such as direct tunable bandgap, absorption coefficient, and long carrier diffusion length. Many research groups took up the challenge to substitute the lead in order to find out some new non-toxic and stable perovskite materials suitable for photovoltaic applications.

Current efforts are under way to improve the stability and durability of perovskite solar cells. There are two main strategies which deserve an immediate attention to develop the stable solar cell and that is to protect the absorber from the external assaults by developing specialized functional barrier structures and to improve the resilience and stability of the absorber itself. These strategies are possible only by either altering the elemental composition of the perovskite or by modifying the perovskite absorber with functional molecules with the purpose of making them less susceptible to moisture degradation.

Lead free perovskite photovoltaics as light harvesting semiconductors have not yet benefited from the same intensive research effort that has propelled lead based perovskites from a power conversion efficiency of 3.8% to >20%. MAPI exhibits a number of remarkable properties that makes it an ideal contender for optoelectronic applications. The compound is a direct band-gap semiconductor with a room temperature band gap of 1.6 eV which is within the range of Shockley-Queisser gap for single junction cells [15]. Despite the processing advantages of perovskites, before the technology can be commercialized the poor stability of the organic-inorganic hybrid combinations with regard to the humidity, heat, light, and oxygen has to overcome. Recent reports have highlighted some innovative and elegant ideas which should be the main focus of future research for the design and practical applicability of photovoltaics materials [16]. Herein we highlight some recent advances in improving the chemical

stability of perovskite materials by substitution of cation and anion elements. Our hope is to pave the way for the design of perovskites to realize the stable and reliable perovskite solar cells with unprecedented improvement in stability.

2. Photovoltaic effect

The absorption of photons with energy above the bandgap ($h\nu > E_g$) in a semiconducting material results the transfer of electrons from the valence band to the conduction band. In a particular material, the excited carriers will come back to the ground-state, with the energy being conserved by the emission of photons. The effect occurs when there is an asymmetric electric potential across the material and hence result the net flow of photogenerated charge carriers namely photocurrent. It is now possible to establish an asymmetric potential in a crystal such as p-n junction thereby giving a good rectification and hence better photovoltaic results. The good photovoltaic materials provide an opportunity to separate the charges as effectively as possible with minimal charge carrier relaxation by transporting them to the contacts and thus minimizing recombination between the electrons & holes. The overall power conversion efficiency represented by η of incident sunlight or power to electricity is directly proportional to the short circuit current (J_{sc}), open-circuit voltage (V_{oc}) and fill factor (FF). the overall equation can be written in mathematical form as:

$$\eta = \frac{J_{sc} V_{oc} FF}{P_{in}}$$

The potential difference developed across the cell when the terminals are not connected is known as open circuit voltage V_{oc} which depends upon the bandgap of the absorber layer. The J_{sc} is the short circuit photocurrent extracted when the voltage across the device is zero which depends upon the range of spectrum absorbed by the active layer in a device. The expected power at the maximum power point observed in J-V curve as a function of power is known as fill-factor.

3. Desired properties for best solar absorber

There are several key properties that generally benefit device efficiencies. Many of these properties are very difficult to measure experimentally, however these can be obtained relatively very cheaply from theoretical perspective. Here we highlight some of the key features which needs to be addressed during device fabrication.

a) Bandgap

The important property of a solar absorber is bandgap which determines the maximum theoretical power conversion efficiency. This is an intrinsic property and has eventually a direct influence on the actual performance of photovoltaic cell. The best solar cell efficiency can be achieved from the materials that possess band gap in the range of 1.1–1.56 eV. Bandgap is the property due to which we will be able to understand that whether the material is able to absorb the visible spectrum or not. How suitable the materials are for photovoltaic

applications would be determined by how close the photon energy is to the bandgap of the material. One of the promising strategies to realize the absorption enhancement is the synthesis of solar cell devices by using the materials having the bandgap as quantified by well-known Shockley-Queisser limit [17]. However to achieve the maximum efficiency, the bandgap of around 1.3 eV would be highly advantageous [18].

b) Effective mass of charge carriers

Some key features for photovoltaics solar energy generation is strong solar absorption, low non-radiative carrier recombination rates and the ability to capitalize for years. One of the important features is reasonably high carrier mobility for the development of solar cell architecture as it decides the range of properties accessible by forming mixed compounds within a compatible material. High charge carrier mobility plays an important role to establish the separation of electron-hole to improve the device performance. The dispersion of band edges particularly envisages the mobility in a material which is theoretically quantified by the effective mass of a carrier giving rise to smaller effective mass and thereby improves the carrier mobility. This carrier mobility is halted by scattering defects, phonons and other charge carriers. However, mobility is not the only important property, but the lifetime of minority carriers have also been considered to be an essential parameter for novel photovoltaic materials because of their role in Shockley-Read-Hall recombination mechanism [19]. Lot of parameters are necessarily required to achieve better performance among which high mobility, diffusion length, and long carrier lifetime are at the top as for as organic-inorganic halide composition is concerned [20].

c) Optical absorption

Optical absorption is among the important parameters and is playing a vital role to the development of high efficiency solar cells. Lot of studies have investigated that how the light-absorption of solar cells can be enhanced by forming antireflective surface techniques [21]. All photovoltaic devices exhibit a certain absorption threshold, and the energy of photons incident on the surface below the threshold do not contribute significantly to electricity conversion. It is noteworthy a strong absorption that can be achieved in a material having a direct bandgap, however, the materials with indirect bandgap may also perform well if a direct transition of suitable energy is also available. Strong absorption is characterized by sudden change in the absorption coefficient. The absorption coefficient reduces below the band edge without any deep states [22]. The absorption coefficient along with the optical band gap and high power conversion efficiency makes materials promising candidates for novel solar cell applications. The knowledge of absorption coefficient in a particular region where the absorber seems to be active is of paramount importance. Concrete information about the absorption coefficient of material provides the advantage over conventional materials and hence allows the fabrication of a desirable and thin cell structure.

d) Ferroelectric and dielectric behavior

Electric response is also playing a vital role to photovoltaic absorber. Considerable efforts have been made to optimize the properties of materials for photovoltaic use within the aim of converting sunlight very efficiently to electrical energy. The process requires the effective absorption of solar radiation to create the separation of photo-excited energy carriers and hence reduce the charge recombination rate as low as possible. Ferroelectric property provides

a viable route to separate charge carriers spontaneously and some noteworthy reports have also been published [23, 24]. However, most of the ferroelectric materials have wide bandgap ($E_g > 2.8$ eV in case of BiFeO_3 and $E_g > 3.5$ eV for Lead-Zirconate-Titanate) that is beyond the visible light spectrum region allowing the use of just a mere percentage (10–20%) of solar energy. However, the ferroelectric behavior perhaps offers most obvious benefit with regard to a high degree of charge screening, and inhibits radiative electron–hole recombination. Having large dielectric constant in ferroelectric materials enables smaller defect binding energies promoting shallow defect states. Thus ferroelectric behavior has been of considerable interest with regard to the hysteresis.

e) Defect tolerance

The physical properties of a material are generally dictated by impurities and defects. These imperfections exist fundamentally in two ways such as doping defects and impurities and create free carriers which enable charge recombination centers and charge scattering halts the mobility. Due to the strong interaction between the theory of defects and doping techniques, a lot of things have been understood about the physics and properties of defects. There are many routes that can be used to instill the defect tolerance in a compound and a specific approach can be adapted to design the device. From the application point of view an optimal material would combine the carrier concentrations with weak carrier scattering. The control on carrier concentration is the key factor in new generation quantum materials as the position of Fermi level which decides whether the specific band features are accessible. Recently, some compositions having ns^2 lone pair such as Bi^{3+} and Sn^{2+} have been reported, considered to be an excellent contenders with defect tolerance features [25].

4. Replacement of lead in perovskite structure

Concerns however have been raised about the possible environmental and legal problems associated with new designs and technology of lead based solar cell fabrication. Lead, as a matter of fact is one of the most studied materials in terms of its toxicity and is found to be hazardous in environment which damages the nervous system and can cause brain disorder. Therefore, lead is unquestionably a problem and the serious efforts are required to phase out lead from the technological materials. Without degrading the favorable photovoltaic properties by replacing lead in perovskite structures by a non-toxic or comparatively non-hazardous compared to lead would therefore be a topic of interest. In this regard, the possibility of replacing lead by different element will be explored by taking the consideration of Goldschmidt rule and some additional quantum mechanical properties. It is very important to consider a very serious parameter while replacing the natural minerals and keeping the crystal structure more or less unchanged is a difference of electronegativity [26]. In addition the formability of halide perovskites depends on some key requirements such as charge neutrality between cations and anions, stability of BX_6 octahedra and the ionic radii of A-site, B-site and the halide component. The octahedral stability can be understood by octahedral factor μ , which is the ratio between the ionic radii of B-site and halide component while as the Goldschmidt tolerance factor predicted by ionic radii derives the stability range of perovskite. Keeping these things in mind one can provide a conceptual toolbox towards replacing lead

and some additional photo-physical properties of perovskite halides. Also this approach is exemplified by focusing on the ions having the ionic radii close to lead ion which should be non-toxic and relatively less expensive, of course without seriously degrading the overall performance of solar cells. Such replacement may be possible in the representative compound MAPI with comparable properties that suits the photovoltaics applications rather than single compound. Various efforts have been made to replace lead by using different ions having same or somehow near to the same ionic radii of lead which are mostly located in the immediate vicinity of lead in the periodic table. This suggests that they could be expected to have naturally a similar electronic structure. Many studies focused on the optimization of materials by testing alternatives at lead site and more than hundred unique combinations have been considered which form stable halide salts. **Figure 2** shows the combination of different solar photovoltaic absorbers used to improve the efficiency along with the stability. Thus an outstanding performance is based on the exceptional properties of halide perovskites exhibiting balanced electron–hole concentration, high absorption coefficient, direct and tunable band-gap, high charge carrier mobilities, and long carrier diffusion lengths etc.

Thus the current limitations impeding the commercialization of lead-based halide perovskite are now well known. These shortcomings are currently tackled by flood of research worldwide by using restless efforts from various research groups around the world to achieve good progress in the field. The stability issue was resolved by introducing the changes in the composition by mere loss of 5% of the initial power conversion efficiency [27]. However the toxicity issue is still an unsolved problem and many research groups took up the challenge to try the substitute of lead with other elements to solve the pending issues to make the materials stable, efficient and environmentally reliable. Therefore, some modifications

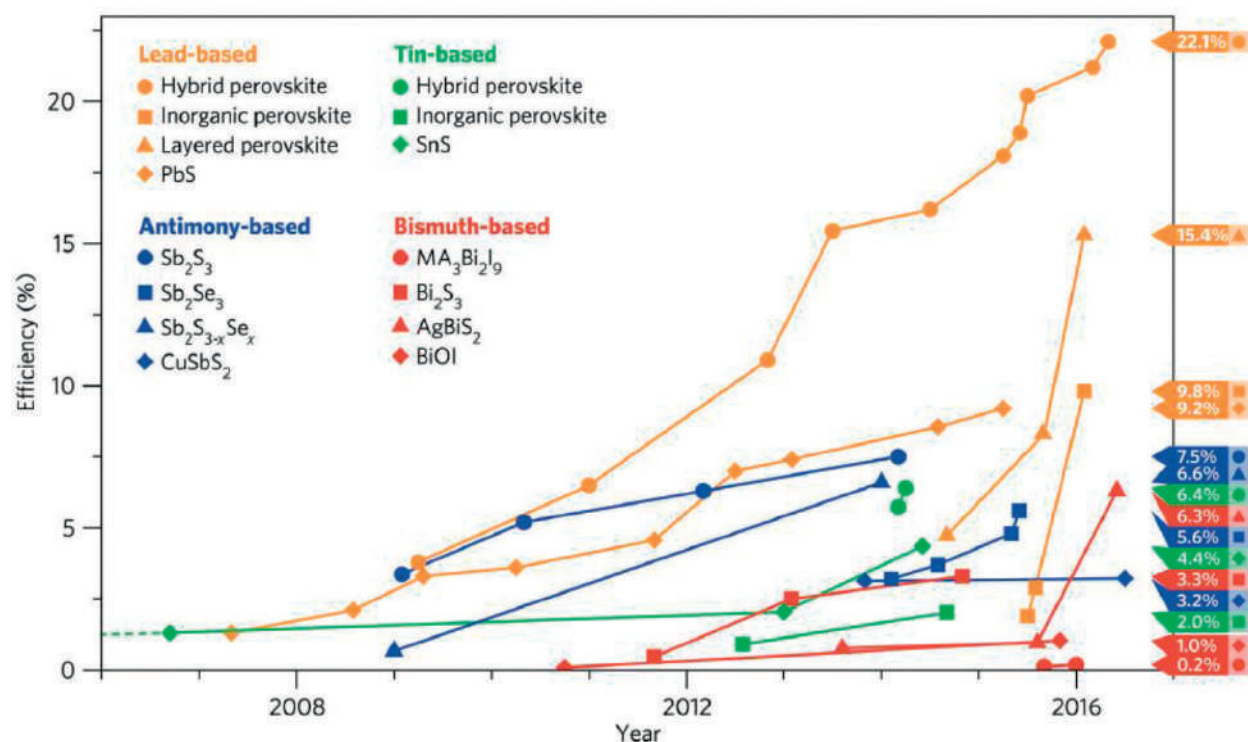


Figure 2. Improvement in the efficiency of different solar absorbers with years. [Source: Ref. 18].

of the well renowned MAPI compound must have the ability to increase the stability of the compound have become highly desirable. Depending upon the nature of the ions within the perovskite structure, a range of different divalent metal cations such as Pb^{2+} , Ge^{2+} , Ca^{2+} , Ba^{2+} , Cu^{2+} , Sr^{2+} , Fe^{2+} , Pd^{2+} , Sn^{2+} , Eu^{2+} , and Mg^{2+} have already been investigated at B-site of hybrid halide perovskites. By comparing the ionic radius for metallic cations with the oxidation state of +2 and after filtering with an ionic radius Pb^{2+} , as in 6-coordinated systems according to Shannon, only nine elements are found to be feasible to substitute for Pb in perovskite structure. To avoid the mixed oxidation state, structural frustration and formation of vacancies in the structure, only three elements are perhaps found the perfect possibility to substitute for lead i.e. Ba^{2+} , Ca^{2+} and Sr^{2+} . The corner sharing of BX_6 octahedra forms a three dimensional network in perovskite structure in which A-site cations occupy the 12-fold coordination to maintain the charge neutrality which is an important parameter for the stability of structure.

The most obvious choice for lead replacement is to see the group 14 metal, such as Sn or Ge and would be an important and fruitful development. Owing to their optical bandgap in the red or infrared region with outstanding carrier mobilities, these materials may constitute promising optoelectronic applications. Consequently the record efficiency for tin based halide perovskite lags behind that of lead halide perovskite. The low energy formation of tin based perovskite is because the oxidation state of tin transfers from +2 to +4 oxidation state upon exposure to ambient conditions, a transformation that does not occur easily in lead perovskites [28]. It was also noticed that tin perovskite had to be performed in nitrogen atmosphere to avoid the quick degradation of the samples. The tin based perovskites have also proved problematic making it difficult to achieve high device fill factor due to high rates of defect-mediated charge carrier recombination. Therefore, it is interesting to find other perovskite which may be more stable and reliable at ambient conditions for photovoltaic device fabrication. Beyond that, tin halide perovskites offer a variety of properties which make them attractive for use in photovoltaics provided the challenge with stability, including narrow bandgap, binding energies, and high charge mobilities than lead halides can be addressed.

The reports suggest that alkaline-earth metals such as magnesium, strontium, barium, calcium etc. can have the potential as substitutes to form perovskite structures due to their suitable ionic radii, abundance on the earth, +2 stable oxidation states similar to Pb^{2+} except toxicity [29]. The simulations performed very recently reveals that Mg^{2+} can replace lead in the structure by forming magnesium halide perovskites with optimum absorption, direct tunable bandgap within visible spectrum and low effective mass [30]. The bandgap has been found to be tunable by introducing different A-site cations. Despite the smaller ionic radius of Mg^{2+} compared to lead, theoretical calculations predicted the stable halide perovskite structure [30]. Since magnesium based halide perovskite structures have not been explored as absorbing materials in solar photovoltaics yet, therefore, this composition requires some special attention.

It is well known that Ba^{2+} has an ionic radius slightly larger than Pb^{2+} and accordingly will also have a slight variation in the tolerance factor of compositions such as $\text{CH}_3\text{NH}_3\text{BaI}_3$ and $\text{CH}_3\text{NH}_3\text{PbI}_3$. However, the density functional theory (DFT) calculations have predicted that stable Ba based perovskite materials have bandgap of 3.3 eV which is quite large as compared

to Pb based compounds (1.57 eV). The reports suggest that the high bandgap is a reason of low electronegativity and low work function [29]. Also these halide perovskites have an issue of synthetic conditions due to their moisture sensitivity which hampers their synthesis formation, characterization and in particular their photovoltaic applications [30].

The best materials among the non-toxic, abundant and low cost alkaline-earth metal is none other than calcium (Ca^{2+}) with an ionic radius almost similar to lead (Pb^{2+}) and hence may be capable of filling the void as non-toxic element in halide perovskite structure [30]. However, as reported earlier, the high bandgap, instability in humid conditions, and less mobility hampers the calcium to be a suitable material for photovoltaics applications [31].

One of the obvious implementation has been done to find a lead free absorber in meso-structured perovskite solar cells such as CsGeI_3 and $\text{CH}_3\text{NH}_3\text{GeI}_3$. However, the power conversion efficiency values were observed to be 0.11 and 0.20% respectively [32]. After some competitive efforts made to improve the efficiency in germanium based perovskites, a power conversion efficiency of approximately 3% in meso-structured cell architecture were claimed. The value is still much less compared to the theoretically possible PCE of >27% as predicted by Qian et al. [33]. Various efforts are still on the way to improve the efficiency of the said perovskites, however, for promising photovoltaic applications and full potential of the Ge based materials is by far not fully exploited yet.

Strontium is fairly a nontoxic and highly abundant metal on earth making it relatively an inexpensive with ionic radii almost similar to lead suggesting that exchange could be possible without affecting the crystal structure. Density functional theory revealed that strontium perovskite such $\text{CH}_3\text{NH}_3\text{SrI}_3$ has similar bonding patterns leading to be a stable phase, despite the difference of electronegativity between lead and strontium [34]. The electronic properties of both Sr. and lead based halide perovskites revealed by simulation suggests that strontium has higher degree of ionic interaction as a consequence of lower electronegativity of strontium. This lower electronegativity together with the missing d-orbitals in the valence of Sr^{2+} is responsible for higher bandgap of around 3.6 eV. This is the main hurdle in Sr. based halide-perovskite that limits its possible application as an absorber material in photovoltaics technology. Another crucial issue related to $\text{CH}_3\text{NH}_3\text{SrI}_3$ is the poor stability at ambient conditions due to its hygroscopic nature.

Transition metal halide and oxide perovskite structures were studied extensively over the decades particularly of their electronic and magnetic transport, magnetic properties, phase transitions and particularly of their high abundance [35–39]. As for as the transition metal oxides/halide perovskites are concerned with regard to their optoelectronic applications, various alternatives of lead-free transition metal perovskites have been predicted to be promising replacement candidates, however, the problems associated to their chemical stability, ionic radii hinders their functionality for photovoltaics. The factors responsible for the low photovoltaic performance from copper halide perovskites are low absorption coefficient, intrinsically low conductivity and high effective mass of holes. The small ionic radii of divalent iron metal (Fe^{2+}) cation compared to lead effectively hinders the formation of three dimensional structures. Several compositions of iron halide perovskites have been studied with regard to their magnetic properties, very few research groups pay attention to the optical properties. The drawback that limits the stability of iron is its multiple oxidation states which follow the

same trend like germanium and tin based perovskites. Therefore a lot of survey is required by iron halide to find its applicability as an absorber for photovoltaic applications.

Rare-earth ions have been investigated in terms of optical applications such as Eu^{2+} , Yb^{2+} , Tm^{2+} , but the applicability of these materials in optoelectronic devices is limited due to their sensitivity towards moisture. Since the photovoltaic properties of lanthanides and actinides still have not been explored, however it is expected that these families may have some interesting optical properties and might be the potential absorbers for photovoltaic devices.

The most exciting developments have been initiated in the materials science of new halide perovskites with an emphasis on alternatives to lead. In the recent developments of new perovskites and perovskite-related materials was found that double perovskites have a potential to touch the new heights in the development of photovoltaic research [40]. Recently, various groups have started to work on double perovskite structures particularly on $\text{Cs}_2\text{AgBiX}_6$ (CABX) family. The photoluminescence behavior of CABX has been studied by Slavney et al. and observed long decay time of the sample as reported in MAPI with an indirect bandgap of 1.95 eV which altogether is an attribute of long recombination lifetime [41]. The group also revealed stability of compound above room temperature after incorporated with bromide up to several days. A wide theoretical screening has been done using DFT calculations and observed that Ag compounds have higher bandgap while Au shares the lowest. The compounds such as $\text{Cs}_2\text{AgSbI}_6$, $\text{Cs}_2\text{BiAuBr}_6$ and $\text{Cs}_2\text{BiCuI}_6$ are those observed to have bandgap within the optimal range [42]. It is clear that double perovskite structures allows us to replace the lead in the composition, however, their stability issue and high indirect bandgap may be a big issue to be resolved before their practical application in photovoltaic technology.

5. Modifications for better and possible photovoltaic materials

The instability with respect to the phase separation of MAPI due to the low formation energy has garnered significant attention to modify the compound in a way to increase the stability due to its record breaking efficiency. However, there are growing concerns surrounding its toxicity and long term stability. Here we will discuss about the other possibilities with the aim of identifying those combinations that will likely to achieve stable and high efficiency.

The method of turning the electronic properties of MAPI is by changing the organic cation. However, the formamidinium as a successful replacement for methylammonium has rather complicated the phase formation while its large bandgap adversely affects the device performance [43]. Instead of using organic cation, inorganic cation can be a best alternative to produce a compound an all-inorganic which may have some possibility to increase the stability. Various attempts made to replace A-site with other organic/inorganic cations have almost proved to be very challenging and difficult. Therefore, to introduce the inorganic cation at A-site by achieving a high efficiency will be a remarkable step towards the stability of perovskite photovoltaics. The tuning of stability and optical properties of a material can play a crucial role to enable the device moisture tolerant with exceptional absorbing characteristics.

The bandgap along with effective mass tuning is possible by replacing the ions in the structure. By replacing the organic part of perovskite structure may be more promising than inorganic one. It has been reported earlier that replacing the methyl ammonium content slightly with formamidinium ion in lead based perovskites can decrease the bandgap somehow and there are also some theoretical arguments which suggest that smaller cation could reduce the bandgap [44]. Therefore, the bandgap of strontium based perovskite may be reduced if the organic cation would be replaced by inorganic cation or changing the cation size will directly affect the geometrical changes such as tolerance factor and octahedral tilting. Since, inorganic counterpart such as Cesium is a best cation that can replace the organic part in the structure, but experimental evidence reveals that there is a problem related to the solubility of Cesium. Although a replacement of organic cation may decrease the bandgap which is the most crucial part to achieve the high performance of perovskites for solar cell applications. Thus the rise and emergence of hybrid perovskite (MAPI) has stimulated the photovoltaic research community. The only material till date is considered to be a third generation solar absorbing material that has a potential to effectively be an alternative to silicon technology. This material clearly possesses the property combinations that demonstrate the potential of polar materials for solar energy conversion.

6. Conclusion

The approach of utilizing Goldschmidt's rules together with additional quantum mechanical considerations can provide a promising route towards replacing lead, as well as providing general insights into the photovoltaics technology of metal halide-perovskites. The materials other than lead-halide perovskites appear to be more stable and exhibit some good functionalities, however the overall power conversion efficiency of these materials is low. Therefore it is very interesting to focus on the optoelectronic properties of the lead free materials in order to achieve the environmental friendly and stable photovoltaic perovskite devices. It is noteworthy that tin based solar absorbers and the group 14 metals have similar electronic properties, but still lead based devices outperform their tin based counterparts due to the oxidation of tin which leads to the efficiency loss. Several materials show some excellent solar absorbing property but they still require some development in their optical and environmental tolerant properties before they can reach to the comparable efficiencies. Therefore, it would be consequently from both toxicological, marketing and more importantly from legal perspective very beneficial if we succeed to replace the lead in perovskite solar cells without seriously degrading their overall performance. However, the lead free material combinations with robust optoelectronic properties with perfect stability at ambient conditions cannot be ruled out in near future.

Acknowledgements

The author Dr. Hilal Ahmad Reshi is grateful to Mr. Farooq Hussain Bhat, Head, department of Physics, and Prof. M. A. Siddiqi, Honorable VC-IUST, Awantipora Kashmir for all sorts of

moral and technical support throughout this tenure. Dr. Hilal is also thankful to his mentors Dr. Vilas Shelke, Novel Materials Research Laboratory, Department of Physics, Barkatullah University, Bhopal, Madhya Pradesh and Prof. S. K. Sarkar, Devices and Interfaces Lab, Energy Science and Engineering department, IIT-Bombay, Mumbai Maharashtra for useful discussion and suggestions.

Author details

Hilal Ahmad Reshi* and Rayees Ahmad Zargar

*Address all correspondence to: hilal.phy@gmail.com

Department of Physics, Islamic University of Science and Technology, Awantipora, Kashmir, India

References

- [1] IEA. Energy Technology Perspectives (ETP). Paris: OECD/IEA; 2014
- [2] Pfann WG, Van Roosbroeck W. Radioactive and photoelectric p-n junction power sources, *Journal of Applied Physics* 1954;**25**:1422-1434, Doi:10.1063/1.1721579
- [3] IEA, Technology Roadmap. Solar Photovoltaic Energy. Paris: OECD/IEA; 2010
- [4] Green MA, Emery K, Hishikawa Y, Warta W, Dunlop ED. Solar cell efficiency tables (version 42). *Progress in Photovoltaics; Research and Applications*. 2013;**21**:827-837
- [5] Green MA. Silicon solar cells: State of the art. *Philosophical Transactions of Royal Society A*. 2013;**371**:20110413-20110414. DOI: 10.1098/rsta.2011.0413
- [6] Galasso FS, Smoluchowski R, Kurti N, Structure, Properties and Preparation of Perovskite Type Compounds, *International Series of Monographs in Solid State Physics*. 1st ed., Pergamon: London, 1969. 220 p. ISBN: 9781483146027
- [7] Service RF. Solar energy. Outlook brightens for plastic solar cells. *Science*. 2011;**332**, 6027(293):293. DOI: 10.1126/science.332
- [8] Snaith HJ. Perovskites: The emergence of a new era for low cost, high efficiency solar cells. *Journal of Physical Chemistry Letters*. 2013;**4**:3623-3630. DOI: 10.1021/jz4020162
- [9] Lee MM, Teuscher J, Miyasaka Y, Murakami TN, Snaith HJ. Efficient hybrid solar cells based on meso-superstructured organometal halide perovskites. *Science*. 2012;**338**:643-647. DOI: 10.1126/science.1228604
- [10] Kim HS, Lee CR, Im JH, Lee KB, Moehl T, Marchioro A, Moon SJ, Baker RH, Yum JH, Moser JE, Gratzel M, Park NG. Solid state submicron thin film mesoscopic solar cell with efficiency exceeding 9%. *Scientific Reports*. 2012;**2**:591-597. DOI: 10.1038/srep00591

- [11] Saliba M, Matsui T, Seo JY, Domanski K, Correa-Baena JP, Nazeeruddin MK, Zakeeruddin SM, Tress W, Abate A, Hagfeldt A, Gratzel M. Cesium-containing triple cation perovskite solar cells: Improved stability, reproducibility and high efficiency. *Energy Environment of Science*. 2016;**9**:1989-1997. DOI: 10.1039/c5ee03874j
- [12] Yang WS, Noh JH, Jeon NJ, Kim YC, Ryu S, Seo J, Seok SL, Cells S. High-performance photovoltaic perovskite layers fabricated through intermolecular exchange. *Science*. 2015;**348**:1234-1237. DOI: 10.1126/science.aaa9272
- [13] Mitzi DB, Field CA, Harrison WTA, Guloy AM. Conducting tin halides with a layered organic based perovskite structure. *Nature*. 1994;**369**:467-469. DOI: 10.1038/369467a0
- [14] Science news, newcomer juices up the race to harness sunlight. *Science*. 2013;**342**:1438-1439. DOI: 10.1126/science.342.6165.1438-b
- [15] DInnocenzo V, Grancini G, Alcocer MJP, Kandada ARS, Stranks SD, Lee MM, Lanzani G, Snaith HJ, Petrozza A. Excitons versus free charges in organo-lead tri-halide perovskites. *Nature Communications*. 2014;**5**:3586-3586. DOI: 10.1038/ncomms4586
- [16] Srivastava R. Perovskite as light harvester: Prospects, efficiency, pitfalls and roadmap. In: Das N, editor. *Nanostructured Solar Cells*. InTech; 2017. DOI: 10.5772/65052
- [17] Shockley W, Queisser HJ. Detailed balance limit of efficiency of p-n junction solar cells. *Journal of Applied Physics*. 1961;**32**:510-519. DOI: 10.1063/1.1736034
- [18] Ganose AM, Savory CN, Scanlon DO. Beyond methylammonium lead iodide: Prospects for the emergent field of ns² containing solar absorbers. *Chemical Communications*. 2017;**53**:20-44. DOI: 10.1039/C6CC06475B], 10.1039/C6CC06475B]
- [19] Jaramillo R, Sher MJ, Ofori-Okai BK, Steinmann V, Yang C, Hartman K, Nelson KA, Lindenberg AM, Gordon RG, Buonassisi T. Transient terahertz photoconductivity measurements of minority-carrier lifetime in tin sulfide thin films: Advanced metrology for an early stage photovoltaic material. *Journal of Applied Physics*. 2016;**119**:035101. DOI: 10.1063/1.4940157
- [20] Stranks SD, Eperon GE, Grancini G, Menelaou C, Snaith MJ. Electron-hole diffusion lengths exceeding 1 micrometer in an organometal trihalide perovskite absorber. *Science*. 2013;**342**:341-344. DOI: 10.1126/science.1243982
- [21] Yu P, Chang CH, Chiu CH, Yang CS, Yu JC, Kuo HC, Hsu SH, Chang YC. Efficiency enhancement of GaAs photovoltaics employing antireflective indium tin oxide nanocolumns. *Advanced Materials*. 2009;**21**:1618-1621. DOI: 10.1002/adma.200802563
- [22] Xing G, Mathews N, Sun S, Lim SS, Lam YM, Gratzel M, Mhaisalkar S, Sum TC. Long range balanced electron and hole-transport lengths in organic-inorganic CH₃NH₃PbI₃. *Science*. 2013;**342**:344-347. DOI: 10.1126/science.1243167
- [23] Choi WS, Chisholm MF, Singh DJ, Choi T, Jellison GE. Wide bandgap tenability in complex transition metal oxides by site-specific substitution. *Nature Communications*. 2012;**3**:689-686. DOI: 10.1038/ncomms1690

- [24] Grinberg I, West DV, Torres M, Gou G, Stein DM, Wu L, Chen G, Gallo EM, Akbashev AR, Davies PK, Spanier JE, Rappe AM. Perovskite oxides for visible light absorbing ferroelectric and photovoltaic materials. *Nature*. 2013;**503**:509-512. DOI: 10.1038/nature12622
- [25] Brandt RE, Stevanovic V, Ginley DS, Buonassisi T. Identifying defect-tolerant semiconductors with high minority carrier lifetimes: Beyond hybrid lead halide perovskites. *MRS Communication*. 2015;**5**:265-275. DOI: 10.1557/mrc.2015.26
- [26] Ringwood AE. The principles governing trace elements distribution during magmatic crystallization part 1: The influence of electronegativity. *Geochimica et Cosmochimica Acta*. 1955;**7**:189-202. DOI: 10.1016/0016-7037(55)90029-6
- [27] Saliba M, Matsui T, Domanski K, Seo JY, Ummadisingu A, Zaheeruddin SM, Correa-Baena JP, Tress WR, Abate A, Hagfeldt A, Gratzel M. Incorporation of rubidium cations into perovskite solar cells improves photovoltaic performance. *Science*. 2016;**354**:206-209. DOI: 10.1126/science.aah5557
- [28] Pyykko P. Relativistic effects in structural chemistry. *Chemical Reviews*. 1988;**88**:563-594. DOI: 10.1021/cr00085a006
- [29] Pazoki M, Jacobsson TJ, Hagfeldt A, Boschloo G, Edvinsson T. Effect of metal cation replacement on the electronic structure of metalorganic halide perovskites: Replacement of lead with alkaline-earth metals. *Physical Review B Condensed Matter and Material Physics*. 2016;**93**:144105-144110. DOI: 10.1103/PhysRevB.93.144105
- [30] Filip MR, Giustino F. Computational screening of homovalent lead substitution in organic-inorganic halide perovskites. *Journal of Physical Chemistry C*. 2016;**120**:166-173. DOI: 10.1021/acs.jpcc.5b11845
- [31] Uribe JL, Ramirez D, Osorio-Guillen JM, Osorio J, Jaramillo F. CH₃NH₃CaI₃ perovskite: Synthesis, characterization, and first principles studies. *Journal of Physical Chemistry C*. 2016;**120**:16393-16398. DOI: 10.1021/acs.jpcc.6b04207
- [32] Krishnamoorthy T, Ding H, Yan C, Leong WL, Baikie T, Zhang Z, Sherburne M, Li S, Asta M, Mathews N, Mhaisalkar SG. Lead-free germanium iodide perovskite materials for photovoltaic applications. *Journal of Materials Chemistry A*. 2015;**3**:23829-23832. DOI: 10.1039/C5TA05741H
- [33] Qian J, Xu B, Tian W. A comprehensive theoretical study of halide perovskites ABX₃. *Organic Electronics*. 2016;**37**:61-73. DOI: 10.1016/j.orgel.2016.05.046
- [34] Jacobsson TJ, Pazoki M, Hagfeldt A, Edvinsson T. Goldschmidt's rules and strontium replacement in lead halogen perovskite solar cells: Theory and preliminary experiments on CH₃NH₃SrI₃. *Journal of Physical Chemistry C*. 2015;**119**:25673-25683. DOI: 10.1021/acs.jpcc.5b06436
- [35] Reshi HA, Singh AP, Pillai S, Para TA, Dhawan SK, Shelke V. X-band frequency response and electromagnetic interference shielding in multiferroic BiFeO₃ nanomaterials. *Applied Physics Letters*. 2016;**109**:142904-142904. DOI: 10.1063/1.4964383

- [36] Needham GF, Willett RD, Franzen HF. Phase transitions in crystalline models of bilayers. 1. Differential scanning calorimetric and x-ray studies of $(C_{12}H_{25}NH_3)_2MCl_4$ and $(NH_3C_{14}H_{29}NH_3)_2MCl_4$ salts ($M = Mn^{2+}, Cd^{2+}, Cu^{2+}$). *The Journal of Physical Chemistry*. 1984;**88**:674-680. DOI: 10.1021/j150648a012
- [37] Reshi HA, Pillai S, Bhuwal D, Shelke V. Nanostructure induced metal-insulator transition and enhanced low-field magnetoresistance in $La_{0.7}Sr_{0.3}MnO_3$ systems. *Journal of Nanoscience and Nanotechnology*. 2013;**13**:4608-4615. DOI: 10.1166/jnn.2013.7136
- [38] Reshi HA, Pillai S, Yadav RS, Para TA, Deshpande UP, Shripathi T, Shelke V. Kondo-like electronic transport and ferromagnetic cluster-glass behavior in $La_{0.7}Sr_{0.3}MnO_3$ nanostructures. *RSC Advances*. 2015;**5**:85950-85956. DOI: 10.1039/c5ra12042j
- [39] Boix PP, Agarwala S, Koh TM, Mathews N, Mhaisalkar SG. Perovskite solar cells: Beyond methylammonium lead iodide. *Journal of Physical Chemistry Letters*. 2015;**6**:898-907. DOI: 10.1021/jz502547f
- [40] Giustino F, Snaith HJ. Towards lead-free perovskite solar cells. *ACS Energy Letters*. 2016;**1**:1233-1240. DOI: 10.1021/acsenergylett.6b00499
- [41] Slavney AH, Hu T, Lindenberg AM, Karunadasa HI. A bismuth-halide double perovskite with long carrier recombination lifetime for photovoltaic applications. *Journal of the American Chemical Society*. 2016;**138**:2138-2141. DOI: 10.1021/jacs.5b13294
- [42] Volonakis G, Filip MR, Haghighirad AA, Sakai N, Wenger B, Snaith HJ, Giustino F. Lead-free halide double perovskites via heterovalent substitution of noble metals. *Journal of Physical Chemistry Letters*. 2016;**7**:1254-1259. DOI: 10.1021/acs.jpcllett.6b00376
- [43] Amat A, Mosconi E, Ronca E, Quarti C, Umari P, Nazeeruddin MK, Gratzel M, De Angelis F. Cation-induced bandgap tuning in organohalide perovskites: Interplay of spin-orbit coupling and octahedra tilting. *Nano Letters*, 2014;**14**:3608-3616. DOI: 10.1021/nl5012992
- [44] Walsh A. Principles of chemical binding and band gap engineering in hybrid organic-inorganic halide perovskites. *Journal of Materials Chemistry C*. 2015;**119**:5755-5760. DOI: 10.1021/jp512420b

